

# GenCast: Diffusion-based ensemble forecasting for medium-range weather

Ilan Price<sup>\*,1</sup>, Alvaro Sanchez-Gonzalez<sup>\*,1</sup>, Ferran Alet<sup>\*,1</sup>, Tom R. Andersson<sup>1</sup>, Andrew El-Kadi<sup>1</sup>, Dominic Masters<sup>1</sup>, Timo Ewalds<sup>1</sup>, Jacklynn Stott<sup>1</sup>, Shakir Mohamed<sup>1</sup>, Peter Battaglia<sup>1</sup>, Remi Lam<sup>1</sup> and Matthew Willson<sup>1</sup>

<sup>\*</sup>Equal contribution, <sup>1</sup>Google DeepMind

Weather forecasts are fundamentally uncertain, so predicting the range of probable weather scenarios is crucial for important decisions, from warning the public about hazardous weather, to planning renewable energy use. Here, we introduce GenCast, a probabilistic weather model with greater skill and speed than the top operational medium-range weather forecast in the world, the European Centre for Medium-Range Forecasts (ECMWF)’s ensemble forecast, ENS. Unlike traditional approaches, which are based on numerical weather prediction (NWP), GenCast is a machine learning weather prediction (MLWP) method, trained on decades of reanalysis data. GenCast generates an ensemble of stochastic 15-day global forecasts, at 12-hour steps and 0.25° latitude-longitude resolution, for over 80 surface and atmospheric variables, in 8 minutes. It has greater skill than ENS on 97.4% of 1320 targets we evaluated, and better predicts extreme weather, tropical cyclones, and wind power production. This work helps open the next chapter in operational weather forecasting, where critical weather-dependent decisions are made with greater accuracy and efficiency.

## 1. Introduction

Every day, people, governments, and other organisations around the world rely on accurate weather forecasts to make many key decisions—whether to carry an umbrella, when to flee an approaching tropical cyclone, planning the use of renewable energy in a power grid, or preparing for a heatwave. But forecasts will always carry some uncertainty, because we can only partially observe the current weather, and even our best models of the weather are imperfect. The highly non-linear physics of weather means that small initial uncertainties and errors can rapidly grow into large uncertainties about the future, giving rise to the famous “butterfly effect” (Lorenz and Haman, 1996). Making critical decisions often requires knowing not just a single probable scenario, but the range of possible scenarios and how likely they are to occur.

Traditional weather forecasting is based on numerical weather prediction (NWP) algorithms, which approximately solve the equations that model atmospheric dynamics. Deterministic NWP methods map the current estimate of the weather to a forecast of how the future weather will unfold over time. This single forecast is only one possibility, so to model the probability distribution of different future weather scenarios (Kalnay, 2003; Palmer and Hagedorn, 2006), weather agencies increasingly rely on “ensemble forecasts”, which generate multiple NWP-based forecasts, each of which models a single possible scenario (ECMWF, 2019; Palmer, 2019; Roberts et al., 2023; Yamaguchi et al., 2018; Zhu et al., 2012b). The European Centre for Medium Range Weather Forecasting (ECMWF)’s ENS (ECMWF, 2019) is the state-of-the-art NWP-based ensemble forecast within ECMWF’s broader Integrated Forecast System (IFS), and will subsume their deterministic forecast, HRES, going forward (ECMWF, 2024). While ENS and other NWP-based ensemble forecasts are very effective at modelling the weather distribution, they are still prone to errors, are slow to run, and are time-consuming to engineer.

Recent advances in machine learning (ML)-based weather prediction (MLWP) have introduced an

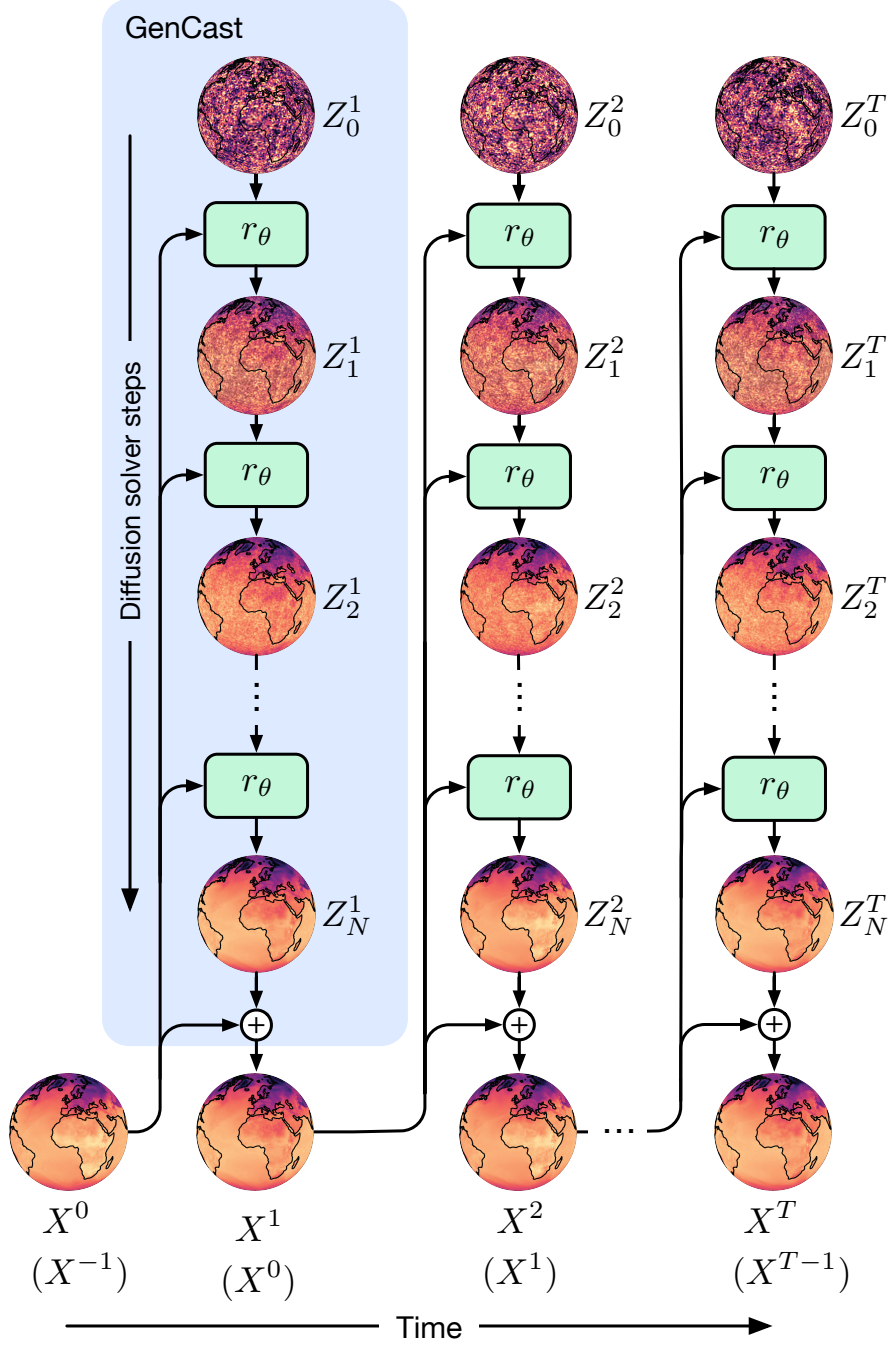


Figure 1 | **Schematic of how GenCast produces a forecast.** The blue box shows how conditioning inputs,  $(X^0, X^{-1})$ , and an initial noise sample,  $Z_0^1$ , are refined by the neural network refinement function,  $r_\theta$  (green box), which is parameterised by  $\theta$ . The resulting  $Z_1^1$  is the first refined candidate state, and this process repeats  $N$  times. The final  $Z_N^1$  is then added as a residual to  $X^0$ , to produce the weather state at the next time step,  $X^1$ . This process then repeats, autoregressively,  $T = 30$  times, conditioning on  $(X^t, X^{t-1})$  and using a new initial noise sample  $Z_0^t$  at each step, to produce the full weather trajectory sample (for visual clarity, we illustrate the previous state in parentheses,  $(X^{t-1})$ , below the current state,  $X^t$ ). Each trajectory generated via independent  $Z_0^{1:T}$  noise samples represents a sample from,  $p(X^{1:T}|X^0, X^{-1})$ .

alternative to NWP-based forecasting methods, and have been shown to provide greater accuracy and efficiency for non-probabilistic forecasts (Bi et al., 2023; Chen et al., 2023; Keisler, 2022; Kurth et al., 2022; Lam et al., 2023; Li et al., 2023; Nguyen et al., 2023). Rather than forecasting a single weather trajectory, or a distribution of trajectories, these methods have largely focused on forecasting the mean of the probable trajectories, with relatively little emphasis on quantifying the uncertainty associated with a forecast. They are typically trained to minimise mean squared error (MSE), and as a result tend to produce blurry forecast states, especially at longer lead times, rather than a specific realisation of a possible weather state (Lam et al., 2023). There have been limited attempts to use traditional initial condition perturbation methods to produce ensembles with MLWP-based forecasts (Bi et al., 2023; Kurth et al., 2022; Li et al., 2023), however they have not addressed the issue of blurring, and have not rivaled operational ensemble forecasts like ENS. One exception is Neural GCM (Kochkov et al., 2023), a hybrid NWP-MLWP method, which combines a traditional NWP’s dynamical core with local ML-based parameterisations, and shows competitive performance with operational ensemble forecasts. However its ensembles are  $1.4^\circ$  spatial resolution, which is an order of magnitude coarser than operational NWP-based forecasts, and it faces serious challenges scaling to operational settings.

## 2. GenCast

Here we introduce a probabilistic weather model—GenCast—which generates global 15-day ensemble forecasts at  $0.25^\circ$  resolution that, for the first time, are more accurate than the top operational ensemble system, ECMWF’s ENS. Generating a single 15-day GenCast forecast takes about 8 minutes on a Cloud TPUv5 device, and an ensemble of forecasts can be generated in parallel.

GenCast models the conditional probability distribution,  $p(X^{t+1}|X^t, X^{t-1})$ , of the future weather state  $X^{t+1}$  conditional on the current and previous weather states. A forecast trajectory,  $X^{1:T}$ , of length  $T$  is modeled by conditioning on the initial and previous states,  $(X^0, X^{-1})$ , and factoring the joint distribution over successive states,

$$p(X^{1:T}|X^0, X^{-1}) = \prod_{t=0}^{T-1} p(X^{t+1}|X^t, X^{t-1}) \quad ,$$

each of which are sampled autoregressively.

The representation of the global weather state,  $X$ , is comprised of 6 surface variables, and 6 atmospheric variables at 13 vertical pressure levels on a  $0.25^\circ$  latitude-longitude grid (see Table B1 for details). The forecast horizon is 15 days, with 12 hours between successive steps  $t$  and  $t + 1$ , so  $T = 30$ .

GenCast is implemented as a conditional diffusion model (Karras et al., 2022; Sohl-Dickstein et al., 2015; Song et al., 2021), a type of generative ML model used to generate new samples from a given data distribution, which underpins many of the recent advances in modelling natural images, sounds, and videos under the umbrella of “generative AI” (Croitoru et al., 2023; Yang et al., 2023). Diffusion models work through a process of iterative refinement. A future atmospheric state,  $X^{t+1}$ , is produced by iteratively refining a candidate state,  $Z_0^{t+1}$ , initialised purely from noise, conditioned on the previous two atmospheric states  $(X^t, X^{t-1})$ . The blue box in Figure 1 shows how the first forecast step is generated from the initial conditions, and how the full trajectory,  $X^{1:T}$ , is generated autoregressively. Because each time step in a forecast is initialised with noise (i.e.,  $Z_0^{t+1}$ ), the process can be repeated with different noise samples, to generate an ensemble of trajectories. See Section D.1 for further details.

At each stage of the iterative refinement process, GenCast applies a neural network architecture comprised of an encoder, processor, and decoder. The encoder component maps the input  $Z_n^{t+1}$ , as

well as the conditioning  $(X^t, X^{t-1})$ , from the native latitude-longitude grid to an internal learned representation defined on an 6-times-refined icosahedral mesh. The processor component is a graph transformer (Vaswani et al., 2017) in which each node attends to its k-hop neighbourhood on the mesh. The decoder component maps from the internal mesh representation back to  $Z_{n+1}^{t+1}$ , which is defined on the latitude-longitude grid.

GenCast is trained on 40 years of ERA5 reanalysis data (Hersbach et al., 2020) from 1979 to 2018, using a standard diffusion model denoising objective (Karras et al., 2022). Crucially, while we only ever directly train GenCast on a single step prediction task, it can be rolled out autoregressively to generate 15-day ensemble forecasts. Section D provides full details of the GenCast architecture and training protocol.

When evaluating GenCast we initialise it with ERA5 reanalysis, together with perturbations derived from the ERA5 Ensemble of Data Assimilations (EDA) (Isaksen et al., 2010) which reflect uncertainty about the initial conditions. Further details are in Section C.

### 3. Realism of GenCast samples

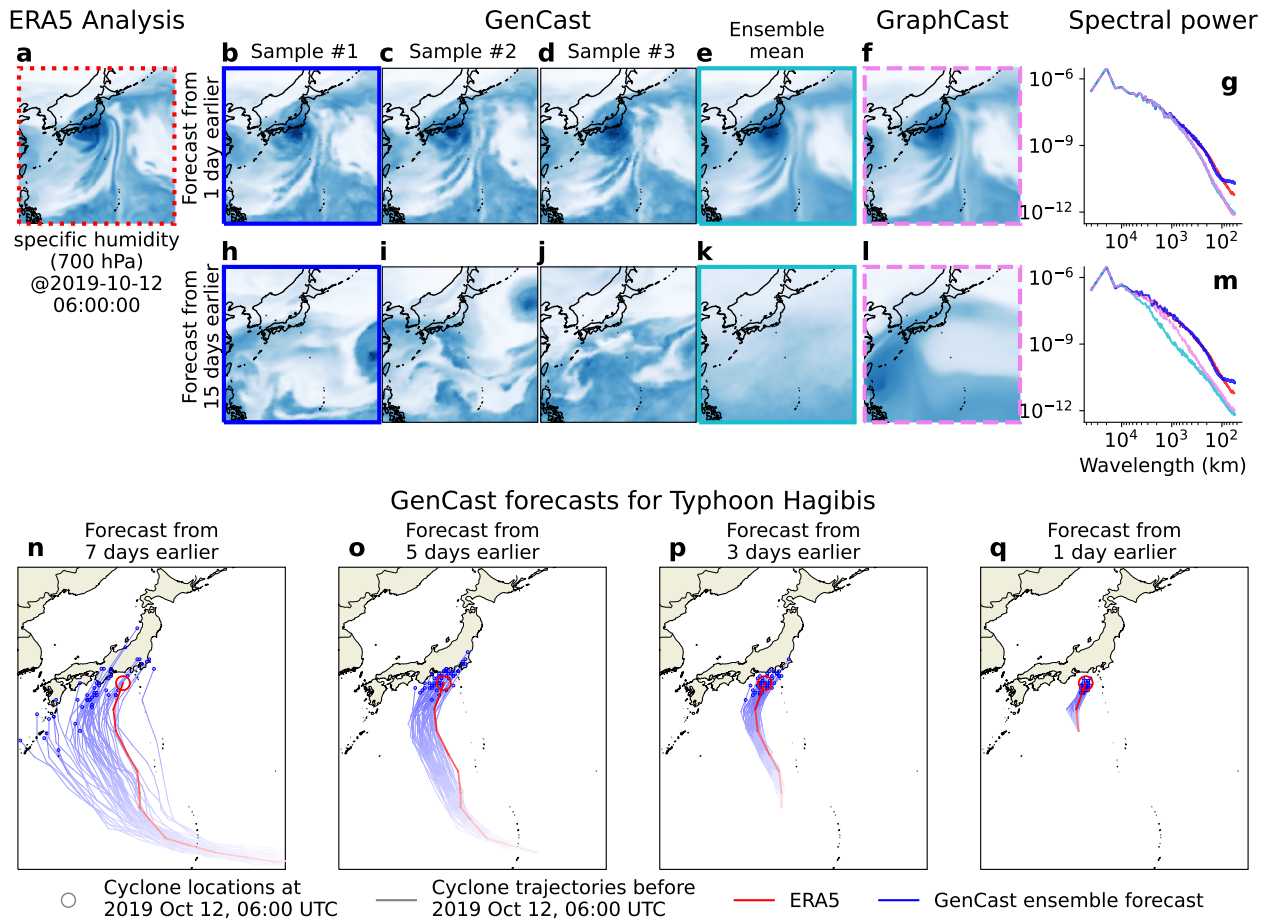
Figure 2 illustrates GenCast’s forecast samples, as well as post-processed tropical cyclone tracks, for Typhoon Hagibis, shortly before it made landfall in Japan on October 12, 2019. Figure 2a-m contrasts GenCast with GraphCast (Lam et al., 2023), a top deterministic MLWP-based method. It shows that GenCast samples, at both 1- and 15-day lead times, are sharp and have spherical harmonic power spectra that closely match the ERA5 ground truth. As expected, the GenCast ensemble mean is blurry, like GraphCast’s states, which lose power at the high frequencies (see also Figure F9 and Figure F10). This reflects how GenCast’s ensembles represent realistic samples from the predictive forecast distribution, while MSE-trained models like GraphCast are closer to the ensemble mean. Over and above the blurring issue, forecasts of the ensemble mean for each variable can be biased when computing nonlinear derived quantities such as wind speed (which is the L2-norm of the  $(u, v)$  wind vector,  $\sqrt{u^2 + v^2}$ ). This is because a nonlinear function of an average is not necessarily equal to the average of that nonlinear function. Computing nonlinear functions directly on the samples avoids this: as shown in Section F.9.1, GenCast exhibits minimal bias on wind speed, unlike GraphCast which exhibits large negative bias.

Figure 2n-q shows how GenCast forecasts can be used in important downstream applications, such as predicting the paths of tropical cyclones. We use Typhoon Hagibis as an example, which was the costliest tropical cyclone of 2019, causing widespread destruction across eastern Japan and over \$17 billion in damages. When initialised 7 days before Typhoon Hagibis’s landfall, GenCast’s predicted trajectory has high uncertainty, covering a wide range of possible scenarios. At shorter lead times, GenCast’s uncertainty about the cyclone’s path is lower, reflecting greater confidence about the landfall timing and location. Figures G1— G4 visualise GenCast and ENS cyclone forecasts for other important cyclones in 2019.

### 4. Baselines

We compare GenCast to ENS, which we regridded from its native  $0.2^\circ$  latitude-longitude resolution<sup>1</sup> to  $0.25^\circ$ . ENS contains 50 perturbed ensemble members, so we used 50-member GenCast ensembles to perform all evaluation. The public TIGGE archive (Swinbank et al., 2016) only makes all 50 ENS

<sup>1</sup>ENS’s resolution changed from  $0.2^\circ$  to  $0.1^\circ$  in mid-2023, however our validation and test years are 2018 and 2019, respectively.



**Figure 2 | Visualisation of forecasts and tropical cyclone tracks for the validity time of 12 October, 2019, 06 UTC, hours before Typhoon Hagibis made landfall in Japan.** (a) The ERA5 analysis state for specific humidity at 700hPa, at validity time 06 UTC, October 12, 2019, shows Typhoon Hagibis near the center of the frame. (b-d) Three sample GenCast forecast states, initialised one day earlier, show how the samples are sharp, and very similar to one another. (e) The GenCast ensemble mean, obtained by computing the mean of 50 sample states like in (b-d), is somewhat blurry, showing how uncertainty results in a blurrier average state. (f) The forecast state from (deterministic) GraphCast, initialised one day earlier like in (b-e), is blurry, similar to GenCast’s ensemble mean. (g) The spatial power spectrum of the states in (a), (b), (e), and (f), where line colors match the frames of the panels, show how GenCast samples’ spectra closely match ERA5’s, while the blurrier GenCast ensemble mean and GraphCast states have less power at shorter wavelengths. (h-m) These subplots are analogous to (b-g), except the forecasts are initialised 15 days earlier. The GenCast samples are still sharp (h-j), while the GenCast ensemble mean (k) and GraphCast (l) states are even blurrier than at the 1-day lead time. This is also reflected in the power spectrum (m), where the GenCast samples’ spectra still closely match ERA5’s, while the GenCast ensemble mean and GraphCast states have even less power in the shorter wavelengths relative to the 1-day lead time in (g). See Section G.2 for more variables and lead times. (n-q) Typhoon Hagibis’s trajectory based on ERA5 (in red) and the ensemble of tropical cyclone trajectories from GenCast (in blue) up to a validity time 4 hours before the cyclone made landfall on Japan. GenCast forecasts are shown at lead times of 7, 3, 5, and 1 day/s. The blue and red circles show cyclone locations at the validity time. At long lead times the cyclone trajectories have substantial spread, while for the shorter lead times the predictive uncertainty collapses to a small range of trajectories. See Section G.1 for details and additional cyclone visualisations.

ensemble members available for surface variables and for atmospheric variables at 8 pressure levels in the troposphere. So these are the variables and levels we compare models on.

For an ML baseline, we use GraphCast (Lam et al., 2023) to generate ensemble forecasts (denoted GraphCast-Perturbed). Since GraphCast is a deterministic model, all ensemble spread must come from differences in the initial conditions. We initialise GraphCast using ERA5 reanalysis plus the ERA5 EDA perturbations used for GenCast, however in order to improve dispersion and skill of the ensemble we found it necessary to supplement them with additional ad hoc Gaussian Process perturbations; full details are in Section C.

For a fair comparison among models, we evaluate each model against its corresponding analysis. We follow the protocol described in Lam et al. (2023, Appendix Section 5.2), in which we evaluate ECMWF’s operational forecasts against HRES-fc0 (a dataset comprising the initial conditions used for their HRES deterministic forecast), and we evaluate ML models, that were trained and initialised using ERA5, against ERA5.

During our 2019 test period, ENS was initialised with analyses whose assimilation window had between 3 and 5 hours of look-ahead beyond the stated initialisation time (Lean et al., 2019). Again following Lam et al. (2023)’s protocol, we initialise ML models using ERA5 at 06 UTC and 18 UTC, since these benefit from only 3 hours of look-ahead<sup>2</sup>. In comparison, ERA5’s 00 and 12 UTC times have 9 hours of look-ahead, which may translate into improved metrics for 00/12 UTC initialised ML model forecasts (as shown in Figure F31). Overall, the difference in assimilation windows used in our evaluation leaves ENS with a small advantage of up to 2 hours additional look-ahead over the ML models, for all variables except sea surface temperature (SST).

We follow standard verification practice (W.M.O., 2019, Section 2.2.35) in evaluating ensemble forecasts using a single deterministic analysis as ground truth. However we note that this favours under-dispersion at short lead times. For example, at a lead time approaching zero, scores computed against deterministic analysis would be optimized by setting all initial conditions equal to the deterministic analysis, ignoring initial condition uncertainty.

## 5. Ensemble skill

To evaluate GenCast’s performance compared to ENS and GraphCast-Perturbed— our primary NWP- and MLWP-based baselines, respectively — we report Continuous Ranked Probability Scores (CRPS) for all evaluation variables, lead times, and pressure levels. The CRPS (Gneiting and Raftery, 2007) is a standard measure of the skill of a probabilistic forecast. It measures how well the marginal distributions of the forecast represent the ground truth, and it is minimized, in expectation, by a forecast whose marginals reflect true predictive uncertainty. See Section E.2.1 for CRPS’s mathematical definition.

As shown in Figure 3’s CRPS scorecard, GenCast’s forecasts are significantly more skillful ( $p < 0.05$ ) than ENS’s on 97.4% of our 1320 variable, lead time, and vertical level combinations (and 99.8% of targets at lead times greater than 36 hours)<sup>3</sup>. Blue cells on the scorecard indicate a variable, lead time, and level combination where GenCast has better (i.e. lower) CRPS skill scores than ENS, while red cells indicate lower CRPS for ENS. GenCast’s largest improvements are often at shorter lead times up to around 3-5 days, for surface variables, as well as temperature and specific humidity at

<sup>2</sup>An exception is sea surface temperature (SST), which in ERA5 is updated once per 24 hours based on a longer assimilation window; however this is a relatively slow-changing variable and we do not expect any extra look-ahead to provide a material advantage.

<sup>3</sup>Note, due to our lack of confidence in the the quality of ERA5 precipitation data, we exclude precipitation results from our main results, and refer readers to Section F.4.

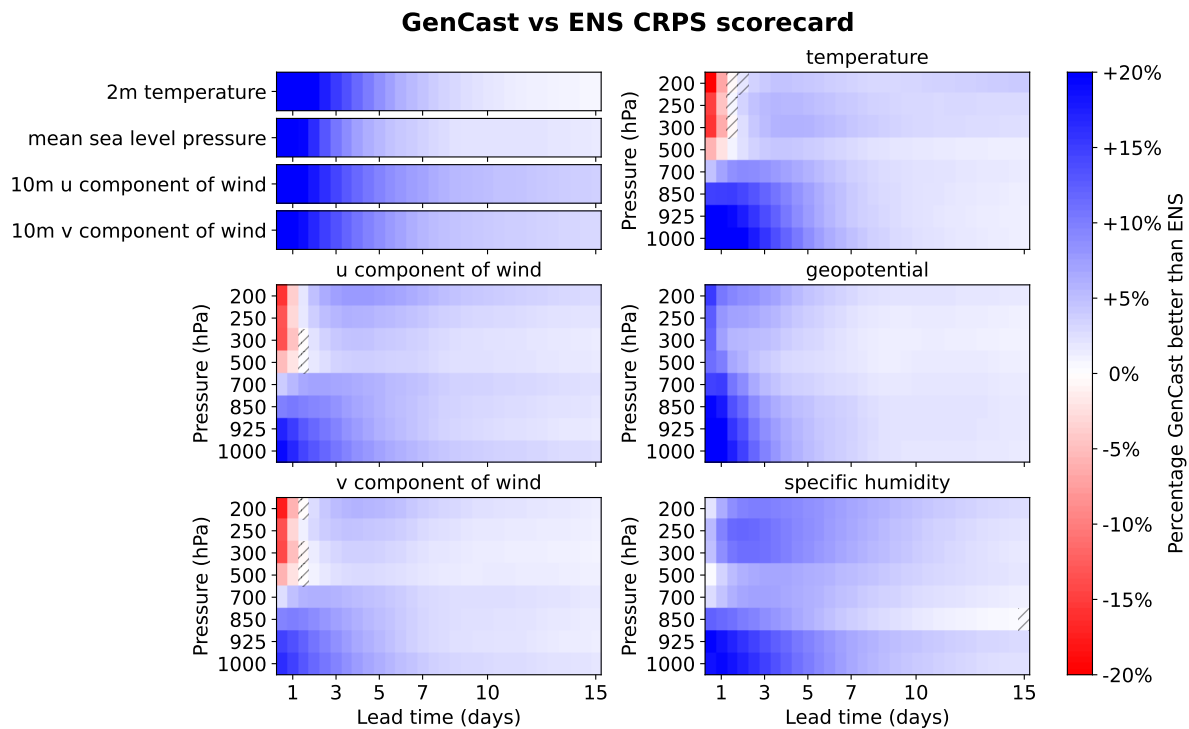


Figure 3 | **CRPS scores for GenCast versus ENS in 2019.** The scorecard compares CRPS skill between GenCast and ENS across all variables and 8 pressure levels, where dark blue indicates GenCast is 20% better than ENS, dark red indicates GenCast is 20% worse, and white means they perform equally. The results indicate that GenCast significantly outperforms ENS ( $p < 0.05$ ) on 97.4% of all reported variable, lead time, and level combinations. Hatched regions indicate where neither model is significantly better.

higher pressure levels, where CRPS skill scores range between 10-30% better. When compared to GraphCast-Perturbed, we found GenCast has better CRPS on 99.6% of targets, as shown in Section F.6 and Figure F12. Figure F11 further shows that GraphCast-Perturbed only outperforms ENS on CRPS in 27% of targets, which are concentrated at shorter lead times.

We also compared the Root Mean Squared Error (RMSE) of GenCast's and ENS's ensemble means. The Ensemble-Mean RMSE measures how the mean of an ensemble of forecasts matches ground truth. While RMSE is a common metric for deterministic forecasts, it does not account for uncertainty, which is central to probabilistic verification. Nonetheless, as shown in Figure F5, GenCast's ensemble mean RMSE is as good or better than ENS's on 96% of targets, and significantly better ( $p < 0.05$ ) on 82% of targets.

## 6. Ensemble calibration

For a probabilistic forecast to be useful, it should be well-calibrated: it should know when it may be wrong, and have confidence when it is likely to be right. This allows a decision-maker to hedge their choices in proportion to the forecast's confidence. Two common tools in the weather community for evaluating calibration, on average, are spread/skill ratios and rank histograms.

Well-calibrated probabilistic forecasts exhibit uncertainty (as measured by ensemble spread) which is commensurate on average with the size of its errors (Fortin et al., 2014). The degree to which

this relationship holds can be quantified by the spread/skill ratio defined in Section E.2.3. This ratio should be 1 for a perfect ensemble forecast, with values greater than 1 suggestive of over-dispersion (an under-confident forecast), and values less than 1 suggestive of under-dispersion (over-confidence).

Similarly, the members of an ideal ensemble forecast should be indistinguishable from ground truth values. Deviations from this property on average can be diagnosed using rank histograms (Talagrand, 1999). The rank histogram should be flat if the truth tends to be indistinguishable from the ensemble members,  $\cap$ -shaped if the truth mostly ranks near the center of the ensemble (indicating the ensembles are over-dispersed), and  $\cup$ -shaped if the truth ranks mostly near the tails of the ensemble (indicating the ensembles are under-dispersed). See Section E.2 for definitions and details.

Generally GenCast exhibits as good, or better, calibration than ENS according to these metrics (see Section F.2). GenCast’s spread-skill scores are usually close to 1, as shown in Figure F2. GenCast also tends to have flat rank histograms, as shown in Figure F3 and Figure F4. In contrast, GraphCast-Perturbed is consistently overconfident, showing spread-skill scores  $< 1$  and  $\cup$ -shaped rank histograms.

## 7. Extreme weather events

Deciding whether, and how, to prepare for extreme weather involves trading off the *cost* of preparing for an event which might not occur, against the *loss* incurred if no preparations are made and it does occur. In this cost/loss model (Thompson, 1952), the optimal decision is to prepare whenever the probability of the event exceeds the cost/loss ratio. Skillful forecasts of rare and extreme weather events are crucial for optimising these decisions, and the value of a forecast to a particular decision-maker depends on the situation’s specific cost/loss ratio.

A standard metric for representing the potential value of a forecast, as a function of cost/loss ratio, is Relative Economic Value (REV, Richardson (2000)). REV quantifies the gain of using a particular forecast over using climatology as a naive baseline (which would yield REV of 0), normalised by the gain of using a perfect forecast which is correct 100% of the time (which would yield REV of 1). See Section E.2.6 for details. We compute REV for a range of different cost/loss ratio trade-offs, showing the impact of a particular forecast across a wide range of decision scenarios.

### 7.1. Local surface extremes

Extreme heat, cold, wind, and other severe surface weather pose hazards to lives and property, but can be anticipated and prepared for using ensemble forecasts. To build intuition, consider a scenario in which an upcoming heatwave threatens to yield a 7-year high temperature tomorrow (exceeding the 99.99th percentile relative to climatology). Let us assume the cost of preparing by staging relief supplies is 1/20 of the loss associated with the public health impact if the population endures the heat unprepared, giving a cost/loss ratio is 0.05. Figure 4a shows that GenCast (blue curves) has 1.9 $\times$  better REV than ENS (black curves) in this scenario. GenCast also shows a consistent advantage across other cost/loss values (x-axis), and for lead times of 5 and 7 days (dashed and dash-dot lines, respectively). Section F.7 shows that the increased value provided by GenCast also applies across other levels of extreme event (other exceedance percentiles), and for other variables including extreme low temperature, high surface wind speed, and low mean sea level pressure (see Figures F13 to F16 for details and statistical tests).

Another method for assessing skill at extreme-weather prediction is to evaluate Brier skill scores (Section E.2.5) for the exceedance of the same high and low percentiles of the climatological distribution. Figure F17 shows the Brier skill scores of GenCast compared to ENS for predicting the

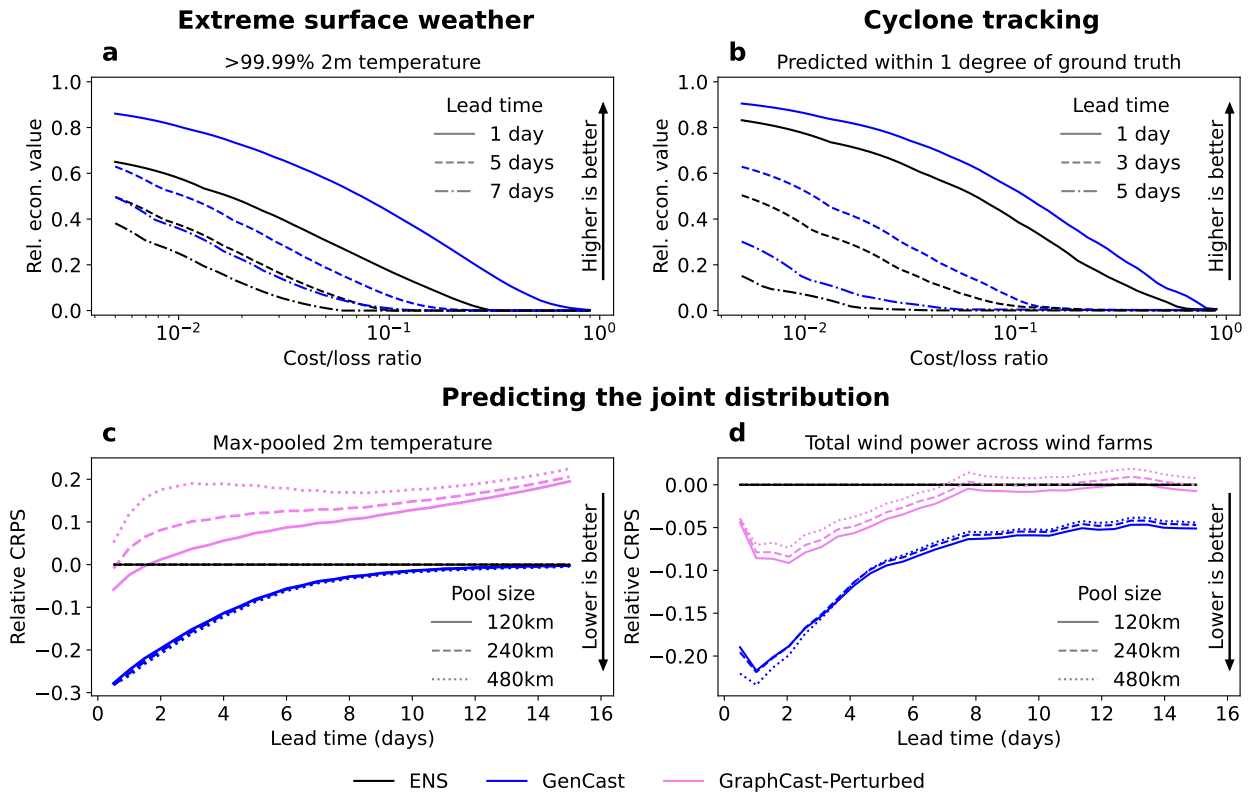


Figure 4 | **Extreme weather, joint measures, and wind power.** (a) Relative economic value (REV) for predictions of the exceedance of the 99.99th percentile for 2 m temperature, at lead times of 1, 5 and 7 days. (b) Relative economic value (REV) for predictions of the presence of a cyclone in any location at a given time, at lead times of 1, 3, and 5 days. (c) Relative CRPS of max-pooled 2m temperature, for different pooling region sizes. (d) Relative CRPS of the total wind power summed across wind farm locations in pooling regions of different sizes.

exceedance of the 99.99th, 99.9th, and 99th percentile events, for high 2 m temperature and 10 m wind speed, and for extremely low temperature and mean sea level pressure below the 0.01, 0.1 and 1st percentiles across all lead times. GenCast significantly ( $p < 0.05$ ) improves on ENS across all of these variables and thresholds, with the exception of low mean sea level pressure where some improvements are not significant.

## 7.2. Tropical cyclones

Tropical cyclones cause thousands of deaths and tens of billions of dollars in damages on average every year, and accurately predicting their emergence and trajectory is essential to prepare for and mitigate their effects (Martinez, 2020). However, given that it is impossible to predict definitively if a cyclone will appear and exactly where it will go, the ideal forecast should generate a distribution over possible trajectories, skillfully assigning probabilities for whether a particular location will be hit by a cyclone at a given time.

To obtain forecasts for the presence and tracks of tropical cyclones, we apply the TempestExtremes tropical cyclone tracker (Ullrich et al., 2021) to ensemble forecasts from both GenCast and ENS, for each initialisation time and each ensemble member. We then apply the same tracker to ERA5 and HRES-fc0, generating ground truth tracks for GenCast and ENS, respectively. We define the presence

or absence of a cyclone centre in a given location at a given time as a binary event, with a forecast probability equal to the proportion of ensemble members that predict a cyclone in that location at that time. See Section E.5 for details.

To assess the value of different models' tropical cyclone forecasts, consider a scenario where you need to decide whether to prepare for the potential landfall of a cyclone. As an example, assume that enduring a cyclone unprepared would incur a loss 100× greater than the cost of planning for evacuation or stockpiling emergency supplies like food, water, medicine and fuel (i.e., a cost/loss ratio of 0.01). Figure 4b shows that relying on GenCast instead of ENS for a cost/loss ratio of 0.01 yields 11%, 38%, 106% higher relative economic values at 1 day, 3 days and 5 days lead time respectively. Across other cost/loss ratios, and for lead times up to 7 days, GenCast consistently yields greater REV (see Section F.8 for further tropical cyclone results). This suggests GenCast's forecasts can provide substantial value in deciding how to prepare for tropical cyclones.

## 8. Skill in predicting the joint distribution

Ensemble forecasting systems like GenCast sample from a high-dimensional joint spatiotemporal distribution, as opposed to modelling weather independently at each point in space and time. Capturing this joint distribution accurately is key for applications where spatially coherent weather trajectories are needed, such as renewable energy prediction. To assess this, we evaluate GenCast, GraphCast-Perturbed, and ENS on two spatial structure prediction tasks: spatial pooling and regional wind power prediction.

### 8.1. Spatially pooled evaluation

Per-grid-cell verification, like the CRPS scorecard (Figure 3), evaluates marginal predictive distributions, but do not measure the accuracy of the forecasts' larger-scale spatial structures. Here we use a neighbourhood verification approach (Ebert, 2008), computing average-pooled and max-pooled versions of the CRPS scorecard from Section 5. Forecasts and analysis targets are aggregated over circular spatial regions distributed to jointly cover the Earth's surface, and CRPS is computed on these pooled quantities for a range of pooling region sizes from 120 km to 3828 km (see Section E.6).

Figure 4c shows the relative CRPS of GenCast compared to ENS and GraphCast-Perturbed for max-pooled 2 m temperature. GenCast shows ~25% improvement at short lead times, and plateauing from approximately 8 days lead time close to ENS performance. These improvements are consistent across spatial scales, unlike GraphCast-Perturbed, which not only does substantially worse than ENS, but also sees its relative performance degrade as the pooling size increases.

Aggregating over all 5400 pooled verification targets—across all variables, levels, lead times, and spatial scales—GenCast outperforms ENS on average-pooled CRPS in 98.1% of targets and on max-pooled CRPS in 97.6% of targets, with relative performance increasing at larger scales (see Figure F23, Figure F24). This contrasts with GraphCast-Perturbed, which only outperforms ENS in 23.9% of targets for average-pooled CRPS and 7.0% of targets for max-pooled CRPS. This suggests that GenCast captures spatial structure substantially better than ENS and GraphCast-Perturbed across all surface and atmospheric variables.

### 8.2. Regional wind power forecasting

In the electricity sector, power grid operators use regional wind power forecasts for tasks like unit commitment and reserve quantification (Siebert, 2008), where leveraging forecast uncertainty can

improve decision-making (Matos and Bessa, 2011; Rachunok et al., 2020). However, forecast errors make it harder to ensure the balance of supply and demand. Because of this, operators often rely on fossil fuel-based spinning reserves (Siebert, 2008), which undermines wind power’s potential for reducing carbon emissions (Gielen et al., 2019).

To estimate GenCast’s potential impact in wind energy applications, we conducted a simplified regional wind power forecasting experiment, where we interpolate 10 m wind speed of forecasts and analyses at all 5344 wind farm locations from the Global Power Plant Database (Byers et al. 2018, Figure E5). 10 m wind speeds are converted to wind power using a standard idealised power curve (see Figure E4) multiplied by each wind farm’s nominal capacity. Wind power (in megawatts) is then summed across arbitrary groupings of wind farms defined by the pooling regions from Section 8.1 with sizes 120 km, 240 km, and 480 km (see Section E.7 for further details).

GenCast outperforms ENS’s CRPS by around ~20% up to lead times of 2 days, 10-20% from 2-4 days, and retains statistically significant ( $p < 0.05$ ) improvements out to 10 days (Figure 4d and Figure F27). This is a substantially greater improvement than that provided by GraphCast-Perturbed. Though only a simplified experiment, these results suggest GenCast provides more skillful wind forecasts, which has potential value for the management and utilisation of wind energy.

## 9. Conclusion

Our results suggest that probabilistic weather forecasts based on MLWP are more skillful, and faster to generate, than the top NWP-based ensemble forecast, ECMWF’s ENS. GenCast generates stable, skillful 15-day global forecasts, despite only being explicitly trained on 12-hour steps, which suggests that GenCast’s predicted weather states are realistic samples of weather trajectories. Across a comprehensive probabilistic scorecard of variables, vertical levels, and lead times, as well as several important application settings, GenCast has greater accuracy and decision-making value than ENS. GenCast’s ensembles have well-calibrated uncertainty, allowing users to trust that the model generally has the right level of confidence in its predictions.

These results invite the question: what is required to deploy MLWP-based models in operation? While GenCast operates at  $0.25^\circ$ , which approximately matches the  $0.2^\circ$  resolution of ENS (which was upgraded to  $0.1^\circ$  in mid-2023), it may be valuable to scale up to higher resolution. GenCast is trained and evaluated on ERA5, and while GraphCast has been shown to be similarly effective when trained on operational HRES inputs and targets (Rasp et al., 2023), GenCast will also need to be trained on operational ENS inputs. As a diffusion model, GenCast is computationally more expensive than an equivalent deterministic MLWP architecture, because it requires multiple function evaluations required to sample each forecast timestep, and for applications that require very fast forecasts, distillation (Salimans and Ho, 2022) and other efficiency techniques should be explored. And importantly, GenCast relies on initial conditions from a traditional NWP ensemble data assimilation system, and therefore using GenCast for operational forecasts will still require NWP-based data assimilation to provide the input analysis.

Together our results open a new front in weather forecasting, promising greater accuracy, efficiency, and accessibility across a wide range of settings. More generally, our work demonstrates that cutting-edge generative AI methods can capture very high-dimensional and complex distributions over rich temporal dynamics, with sufficient accuracy and reliability to support effective decision-making in crucial applications.

## Acknowledgements

In alphabetical order, we thank Alexis Boukouvalas, Matthew Chantry, Yuri Chervonyi, Sander Dieleman, Praneet Dutta, Carl Elkin, Sarah Elwes, Isla Finney, Meire Fortunato, Marta Garnelo, Xavier Glorot, Stephan Hoyer, Dmitrii Kochkov, Pushmeet Kohli, Paul Komarek, Amy Li, Sean Lovett, Rahul Mahrsee, Liam McCafferty, Piotr Mirowski, Kevin Murphy, Kate Musgrave, Charlie Nash, Nick Pezzotti, Luis Piloto, Stephan Rasp, Suman Ravuri, Daniel Rothenberg, Tim Salimans, Fei Sha, Kunal Shah, Jon Small, Duncan Smith, Octavian Voicu, David Wallis, Daniel Worrall, Flora Xue, and Janni Yuval for their advice and/or feedback on our work. We also thank ECMWF for providing invaluable datasets to the research community.

## References

- G. Batzolis, J. Stanczuk, C.-B. Schönlieb, and C. Etmann. Conditional image generation with score-based diffusion models. *arXiv preprint arXiv:2111.13606*, 2021.
- K. Bi, L. Xie, H. Zhang, X. Chen, X. Gu, and Q. Tian. Accurate medium-range global weather forecasting with 3d neural networks. *Nature*, 619(7970):533–538, 2023.
- R. Buizza, M. Leutbecher, and L. Isaksen. Potential use of an ensemble of analyses in the ECMWF ensemble prediction system. *Quarterly Journal of the Royal Meteorological Society*, 134(637):2051–2066, 2008.
- L. Byers, J. Friedrich, R. Hennig, A. Kressig, X. Li, C. McCormick, and L. M. Valeri. A global database of power plants. *World Resources Institute*, 2018.
- K. Chen, T. Han, J. Gong, L. Bai, F. Ling, J.-J. Luo, X. Chen, L. Ma, T. Zhang, R. Su, et al. Fengwu: Pushing the skillful global medium-range weather forecast beyond 10 days lead. *arXiv preprint arXiv:2304.02948*, 2023.
- M. Chen, X. Tan, B. Li, Y. Liu, T. Qin, S. Zhao, and T.-Y. Liu. Adaspeech: Adaptive text to speech for custom voice, 2021.
- F.-A. Croitoru, V. Hondru, R. T. Ionescu, and M. Shah. Diffusion models in vision: A survey. *IEEE Transactions on Pattern Analysis and Machine Intelligence*, 45(9):10850–10869, 2023. doi: 10.1109/TPAMI.2023.3261988.
- D. R. Drew, D. J. Cannon, J. F. Barlow, P. J. Coker, and T. H. A. Frame. The importance of forecasting regional wind power ramping: A case study for the UK. *Renewable Energy*, 114:1201–1208, Dec. 2017.
- J. R. Driscoll and D. M. Healy. Computing fourier transforms and convolutions on the 2-sphere. *Adv. Appl. Math.*, 15(2):202–250, June 1994.
- E. E. Ebert. Fuzzy verification of high-resolution gridded forecasts: a review and proposed framework. *Meteorol. Appl.*, 15(1):51–64, Mar. 2008.
- ECMWF. *IFS Documentation CY46R1*, chapter Part V: Ensemble Prediction System. ECMWF, 2019. doi: 10.21957/38yug0cev. URL <https://www.ecmwf.int/node/19309>.
- ECMWF. Plans for high-resolution forecast (HRES) and ensemble forecast (ENS) control run. <https://www.ecmwf.int/en/about/media-centre/focus/2024/plans-high-resolution-forecast-hres-and-ensemble-forecast-ens>, 2024. [Accessed 25-04-2024].

- B. Efron and B. Narasimhan. The automatic construction of bootstrap confidence intervals. *Journal of Computational and Graphical Statistics*, 29(3):608–619, 2020.
- V. Fortin, M. Abaza, F. Anctil, and R. Turcotte. Why should ensemble spread match the RMSE of the ensemble mean? *Journal of Hydrometeorology*, 15(4):1708–1713, 2014.
- D. Gielen, F. Boshell, D. Saygin, M. D. Bazilian, N. Wagner, and R. Gorini. The role of renewable energy in the global energy transformation. *Energy Strategy Reviews*, 24:38–50, Apr. 2019.
- E. Gilleland, D. Ahijevych, B. G. Brown, B. Casati, and E. E. Ebert. Intercomparison of spatial forecast verification methods. *Weather Forecast.*, 24(5):1416–1430, Oct. 2009.
- T. Gneiting and A. E. Raftery. Strictly proper scoring rules, prediction, and estimation. *Journal of the American statistical Association*, pages 359–378, 2007.
- T. Haiden, M. J. Rodwell, D. S. Richardson, A. Okagaki, T. Robinson, and T. Hewson. Intercomparison of global model precipitation forecast skill in 2010/11 using the seeps score. *Monthly Weather Review*, 140(8):2720–2733, 2012.
- T. M. Hamill. Interpretation of rank histograms for verifying ensemble forecasts. *Monthly Weather Review*, 129(3):550–560, 2001.
- H. Hersbach, B. Bell, P. Berrisford, S. Hirahara, A. Horányi, J. Muñoz-Sabater, J. Nicolas, C. Peubey, R. Radu, D. Schepers, et al. The ERA5 global reanalysis. *Quarterly Journal of the Royal Meteorological Society*, 146(730):1999–2049, 2020.
- J. Ho, A. Jain, and P. Abbeel. Denoising diffusion probabilistic models. *Advances in neural information processing systems*, 33:6840–6851, 2020.
- L. Isaksen, M. Bonavita, R. Buizza, M. Fisher, J. Haseler, M. Leutbecher, and L. Raynaud. Ensemble of data assimilations at ECMWF, 12/2010 2010. URL <https://www.ecmwf.int/node/10125>.
- E. Kalnay. *Atmospheric modeling, data assimilation and predictability*. Cambridge university press, 2003.
- T. Karras, M. Aittala, T. Aila, and S. Laine. Elucidating the design space of diffusion-based generative models. *Advances in Neural Information Processing Systems*, 35:26565–26577, 2022.
- R. W. Katz and A. H. Murphy. *Economic value of weather and climate forecasts*. Cambridge University Press, 1997.
- R. Keisler. Forecasting global weather with graph neural networks. *arXiv preprint arXiv:2202.07575*, 2022.
- J. King, A. Clifton, and B. M. Hodge. Validation of power output for the wind toolkit. *National Renewable Energy Laboratory, NREL*, 9 2014. doi: 10.2172/1159354. URL <https://www.osti.gov/biblio/1159354>.
- K. R. Knapp, M. C. Kruk, D. H. Levinson, H. J. Diamond, and C. J. Neumann. The international best track archive for climate stewardship (IBTrACS): Unifying tropical cyclone data. *Bull. Am. Meteorol. Soc.*, 91(3):363–376, Mar. 2010.
- D. Kochkov, J. Yuval, I. Langmore, P. Norgaard, J. Smith, G. Mooers, J. Lottes, S. Rasp, P. Düben, M. Klöwer, et al. Neural general circulation models. *arXiv preprint arXiv:2311.07222*, 2023.

- T. Kurth, S. Subramanian, P. Harrington, J. Pathak, M. Mardani, D. Hall, A. Miele, K. Kashinath, and A. Anandkumar. FourCastNet: Accelerating global high-resolution weather forecasting using adaptive fourier neural operators. *arXiv preprint arXiv:2208.05419*, 2022.
- R. Lam, A. Sanchez-Gonzalez, M. Willson, P. Wirnsberger, M. Fortunato, F. Alet, S. Ravuri, T. Ewalds, Z. Eaton-Rosen, W. Hu, et al. Learning skillful medium-range global weather forecasting. *Science*, page eadi2336, 2023.
- P. Lean, M. Bonavita, E. Hólm, N. Bormann, and T. McNally. Continuous data assimilation for the IFS. *ECMWF Newsletter*, pages 21–26, Jan. 2019. doi: 10.21957/9pl5fc37it. URL <https://www.ecmwf.int/node/18882>.
- H. Li, L. Chen, X. Zhong, F. Zhang, Y. Cheng, Y. Xu, and Y. Qi. FuXi: A cascade machine learning forecasting system for 15-day global weather forecast. *npj Climate and Atmospheric Science*, 6(190), 2023.
- E. N. Lorenz and K. Haman. The essence of chaos. *Pure and Applied Geophysics*, 147(3):598–599, 1996.
- I. Loshchilov and F. Hutter. Decoupled weight decay regularization. In *International Conference on Learning Representations*, 2018.
- C. Lu, Y. Zhou, F. Bao, J. Chen, C. Li, and J. Zhu. DPM-Solver++: Fast solver for guided sampling of diffusion probabilistic models. *arXiv preprint arXiv:2211.01095*, 2022.
- L. Magnusson, S. Majumdar, R. Emerton, D. Richardson, M. Alonso-Balmaseda, C. Baugh, P. Bechtold, J. Bidlot, A. Bonanni, M. Bonavita, et al. Tropical cyclone activities at ECMWF. *ECMWF Technical Memorandum*, 2021.
- A. B. Martinez. Forecast accuracy matters for hurricane damage. *Econometrics*, 8(2):18, 2020.
- M. A. Matos and R. J. Bessa. Setting the operating reserve using probabilistic wind power forecasts. *IEEE Trans. Power Syst.*, 26(2):594–603, May 2011.
- A. H. Murphy. The value of climatological, categorical and probabilistic forecasts in the cost-loss ratio situation. *Monthly Weather Review*, 105(7):803–816, 1977.
- T. Nguyen, R. Shah, H. Bansal, T. Arcomano, S. Madireddy, R. Maulik, V. Kotamarthi, I. Foster, and A. Grover. Scaling transformer neural networks for skillful and reliable medium-range weather forecasting. *arXiv preprint arXiv:2312.03876*, 2023.
- T. Q. Nguyen and J. Salazar. Transformers without tears: Improving the normalization of self-attention. In *Proceedings of the 16th International Conference on Spoken Language Translation*, 2019.
- R. North, M. Trueman, M. Mittermaier, and M. J. Rodwell. An assessment of the SEEPS and SEDI metrics for the verification of 6 h forecast precipitation accumulations. *Meteorological Applications*, 20(2):164–175, 2013.
- T. Palmer. The ECMWF ensemble prediction system: Looking back (more than) 25 years and projecting forward 25 years. *Quarterly Journal of the Royal Meteorological Society*, 145:12–24, 2019.
- T. Palmer and R. Hagedorn. *Predictability of weather and climate*. Cambridge University Press, 2006.
- A. Patton, D. N. Politis, and H. White. Correction to “Automatic block-length selection for the dependent bootstrap” by D. Politis and H. White. *Econometric Reviews*, 28(4):372–375, 2009.

- D. N. Politis and J. P. Romano. The stationary bootstrap. *Journal of the American Statistical association*, 89(428):1303–1313, 1994.
- D. N. Politis and H. White. Automatic block-length selection for the dependent bootstrap. *Econometric reviews*, 23(1):53–70, 2004.
- B. Rachunok, A. Staid, J.-P. Watson, and D. L. Woodruff. Assessment of wind power scenario creation methods for stochastic power systems operations. *Appl. Energy*, 268:114986, June 2020.
- S. Rasp, P. D. Dueben, S. Scher, J. A. Weyn, S. Mouatadid, and N. Thuerey. WeatherBench: a benchmark data set for data-driven weather forecasting. *Journal of Advances in Modeling Earth Systems*, 12(11):e2020MS002203, 2020.
- S. Rasp, S. Hoyer, A. Merose, I. Langmore, P. Battaglia, T. Russel, A. Sanchez-Gonzalez, V. Yang, R. Carver, S. Agrawal, et al. Weatherbench 2: A benchmark for the next generation of data-driven global weather models. *arXiv preprint arXiv:2308.15560*, 2023.
- S. Ravuri, K. Lenc, M. Willson, D. Kangin, R. Lam, P. Mirowski, M. Fitzsimons, M. Athanassiadou, S. Kashem, S. Madge, et al. Skilful precipitation nowcasting using deep generative models of radar. *Nature*, 597(7878):672–677, 2021.
- D. S. Richardson. Skill and relative economic value of the ECMWF ensemble prediction system. *Quarterly Journal of the Royal Meteorological Society*, 126(563):649–667, 2000.
- D. S. Richardson. *Predictability and economic value*, page 628–644. Cambridge University Press, 2006.
- N. Roberts, B. Ayliffe, G. Evans, S. Moseley, F. Rust, C. Sandford, T. Trzeciak, P. Abernethy, L. Beard, N. Crosswaite, et al. Improver: The new probabilistic postprocessing system at the Met office. *Bulletin of the American Meteorological Society*, 104(3):E680–E697, 2023.
- M. J. Rodwell, D. S. Richardson, T. D. Hewson, and T. Haiden. A new equitable score suitable for verifying precipitation in numerical weather prediction. *Quarterly Journal of the Royal Meteorological Society*, 136(650):1344–1363, 2010.
- T. Salimans and J. Ho. Progressive distillation for fast sampling of diffusion models. *arXiv preprint arXiv:2202.00512*, 2022.
- K. Sheppard, S. Khrapov, G. Lipták, R. van Hattem, mikedeltalima, J. Hammudoglu, R. Capellini, A. Cermeno, S. bot, Huggle, esvhd, A. Fortin, JPN, M. Judell, R. Russell, W. Li, 645775992, A. Adams, jbrockmendel, M. Rabba, M. E. Rose, N. Tretyak, T. Rochette, U. Leo, X. René-Corail, X. Du, and B. Çelik. bashtage/arch: Release 7.0.0, Apr. 2024. URL <https://doi.org/10.5281/zenodo.10981635>.
- N. Siebert. *Development of methods for regional wind power forecasting*. PhD thesis, École Nationale Supérieure des Mines de Paris, Mar. 2008.
- J. Sohl-Dickstein, E. Weiss, N. Maheswaranathan, and S. Ganguli. Deep unsupervised learning using nonequilibrium thermodynamics. In *International conference on machine learning*, pages 2256–2265. PMLR, 2015.
- Y. Song, J. Sohl-Dickstein, D. P. Kingma, A. Kumar, S. Ermon, and B. Poole. Score-based generative modeling through stochastic differential equations. In *International Conference on Learning Representations*, 2021. URL <https://openreview.net/forum?id=PXTIG12RRHS>.

- R. Swinbank, M. Kyouda, P. Buchanan, L. Froude, T. M. Hamill, T. D. Hewson, J. H. Keller, M. Matsueda, J. Methven, F. Pappenberger, et al. The tigge project and its achievements. *Bulletin of the American Meteorological Society*, 97(1):49–67, 2016.
- O. Talagrand. Evaluation of probabilistic prediction systems. In *Proceedings of “Workshop on Predictability”, 20-22 October 1997, ECMWF, Reading, UK*, 1999.
- J. Thompson. On the operational deficiencies in categorical weather forecasts. *Bulletin of the American Meteorological Society*, 33(6):223–226, 1952.
- P. A. Ullrich and C. M. Zarzycki. TempestExtremes: a framework for scale-insensitive pointwise feature tracking on unstructured grids. *Geosci. Model Dev.*, 10(3):1069–1090, Mar. 2017.
- P. A. Ullrich, C. M. Zarzycki, E. E. McClenny, M. C. Pinheiro, A. M. Stansfield, and K. A. Reed. TempestExtremes v2.1: a community framework for feature detection, tracking, and analysis in large datasets. *Geosci. Model Dev.*, 14(8):5023–5048, Aug. 2021.
- A. Vaswani, N. Shazeer, N. Parmar, J. Uszkoreit, L. Jones, A. N. Gomez, Ł. Kaiser, and I. Polosukhin. Attention is all you need. *Advances in neural information processing systems*, 30, 2017.
- A. Weaver and P. Courtier. Correlation modelling on the sphere using a generalized diffusion equation. *Quarterly Journal of the Royal Meteorological Society*, 127(575):1815–1846, 2001.
- D. Wilks. A skill score based on economic value for probability forecasts. *Meteorological Applications*, 8(2):209–219, 2001.
- D. Wilks. On the reliability of the rank histogram. *Monthly Weather Review*, 139(1):311–316, 2011.
- W.M.O. *Manual on the Global Data-processing and Forecasting System*. World Meteorological Organization, 2019. ISBN 978-92-63-10485-4. URL <https://library.wmo.int/idurl/4/35703>.
- H. Yamaguchi, D. Hotta, T. Kanehama, K. Ochi, Y. Ota, R. Sekiguchi, A. Shimpo, and T. Yoshida. Introduction to JMA’s new global ensemble prediction system. *CAS/JSC WGNE, Research Activities in Atmospheric and Oceanic Modelling*, 42:6–13, 2018.
- R. Yang, P. Srivastava, and S. Mandt. Diffusion probabilistic modeling for video generation. *Entropy*, 25(10):1469, 2023.
- M. Zamo and P. Naveau. Estimation of the continuous ranked probability score with limited information and applications to ensemble weather forecasts. *Mathematical Geosciences*, 50(2):209–234, 2018.
- C. M. Zarzycki and P. A. Ullrich. Assessing sensitivities in algorithmic detection of tropical cyclones in climate data. *Geophys. Res. Lett.*, 44(2):1141–1149, Jan. 2017.
- Y. Zhu, Z. Toth, R. Wobus, M. Wei, and B. Cui. May 2006 upgrade of the GEFS and first implementation of NAEFS systems, 2012b.

# Supplementary material

<b>A</b>	<b>Task definition and general approach</b>	<b>19</b>
<b>B</b>	<b>Data</b>	<b>19</b>
B.1	ERA5 training and evaluation data for GenCast	19
B.2	Data preprocessing	20
B.3	Data Availability	21
<b>C</b>	<b>Initial conditions</b>	<b>22</b>
C.1	Deterministic analysis	22
C.2	Ensemble of data assimilations (EDA) analysis	22
C.3	Deterministic analysis plus EDA perturbations	22
C.4	Additional ad hoc Gaussian process perturbations	22
<b>D</b>	<b>Diffusion model specification</b>	<b>23</b>
D.1	Sampling process	24
D.2	Noise distribution on the sphere	24
D.3	Denoiser architecture	25
D.4	Training the denoiser	25
D.4.1	Resolution training schedule	26
D.5	Sampler hyperparameters	27
<b>E</b>	<b>Supplementary evaluation details</b>	<b>28</b>
E.1	ENS initialisation and evaluation times	28
E.2	Verification metrics	28
E.2.1	CRPS	28
E.2.2	Ensemble mean RMSE	29
E.2.3	Spread/skill ratio	29
E.2.4	Rank histogram	29
E.2.5	Brier skill score	30
E.2.6	Relative Economic Value	30
E.3	Statistical tests	32
E.4	Local surface extremes evaluation	33
E.5	Cyclone tracking	33

E.5.1	Cyclone evaluation	33
E.5.2	Cyclone tracker	35
E.6	Spatially pooled evaluation	36
E.7	Regional wind power forecasting evaluation	39
<b>F</b>	<b>Supplementary results</b>	<b>41</b>
F.1	CRPS line plots	41
F.2	Ensemble calibration	41
F.3	Ensemble-Mean RMSE	44
F.4	Precipitation	46
F.5	Spectrum for additional variables	48
F.6	GraphCast-Perturbed scorecards	50
F.7	Extreme surface weather	51
F.8	Tropical cyclones	55
F.9	Joint distribution	56
F.9.1	Wind speed as a derived variable	56
F.9.2	Pooled evaluation	56
F.10	Regional wind power forecasting statistical significance	63
F.11	Ablation of EDA perturbations in GenCast initial conditions	64
F.12	Empirical support of initialisation time and evaluation time choices for verification	67
F.12.1	Initialisations used for GenCast evaluation	67
F.12.2	Lead time interpolation in regional wind farm evaluation	67
<b>G</b>	<b>Forecast visualisations</b>	<b>70</b>
G.1	Tropical cyclone tracks	70
G.2	Visualising forecasts of additional variables during Typhoon Hagibis	75
G.3	Global forecasts	85
<b>H</b>	<b>Author Contributions</b>	<b>96</b>

## A. Task definition and general approach

In its general formulation, the task of probabilistic forecasting from the present time  $t = 0$  into the future is to model the joint probability distribution,  $p(\bar{X}^{0:T} | O^{\leq 0})$ , where  $T$  is the forecast horizon,  $\bar{X}^i$  denotes the atmospheric state at time  $i$ , and  $O^{\leq 0}$  are observations made up to the forecast initialisation time  $t = 0$ . In NWP-based weather forecasts,  $\bar{X}$  represents variables that are part of the underlying atmospheric fluid equations, on a discrete spatial grid or mesh. This joint distribution is assumed to be Markov, and is factored as,

$$p(\bar{X}^{0:T} | O^{\leq 0}) = \underbrace{p(\bar{X}^0 | O^{\leq 0})}_{\text{State inference}} \underbrace{p(\bar{X}^{1:T} | \bar{X}^0)}_{\text{Forecast model}} = p(\bar{X}^0 | O^{\leq 0}) \prod_{t=1}^T p(\bar{X}^t | \bar{X}^{t-1})$$

Our innovation in this work is an MLWP-based `Forecast model`, and we simply adopt a traditional NWP-based `State inference` approach. We make a number of approximations to the above general formulation, as follows.

The standard approach to `State inference` is to approximate samples from  $p(\bar{X}^0 | O^{\leq 0})$  — the distribution over the current atmospheric state — with an ensemble of NWP-based analysis<sup>4</sup> states, which are generated using a window of observations in a process known as “data assimilation”. We too rely on ensemble analysis to approximate the `State inference` stage: we use ECMWF’s ERA5 archive of reanalysis data (Hersbach et al., 2020), including the ERA5 EDA (ensemble of data assimilations), to represent the initial conditions  $\bar{X}^0$ . Details are in Section C.

We approximate the full atmospheric state,  $\bar{X}$ , with  $X$ , an  $84 \times 720 \times 1440$  array, which includes 6 surface variables, and 6 atmospheric variables at each of 13 vertical pressure levels (see Table B1), on a  $0.25^\circ$  latitude-longitude grid. Because  $X$  is only a partial representation of  $\bar{X}$ , forecasts initialised with a single  $X$  may not be able to generate forecasts as accurate as those initialised with  $\bar{X}$ , and in practice we found conditioning on the current *and* previous state,  $X^0$  and  $X^{-1}$ , respectively, to be more effective. Therefore, the initial conditions provided as input to our model are  $(X^0, X^{-1})$ . This means we approximate a single step of the `Forecast model` as  $p(\bar{X}^t | \bar{X}^{t-1}) \approx p(X^t | X^{t-1}, X^{t-2})$ .

We generate 15-day forecasts, at 12 hour steps, so  $T = 30$ . To sample a weather trajectory,  $X^{1:T} \sim p(X^{1:T} | X^0, X^{-1})$ , we first sample  $(X^0, X^{-1})$  using ERA5 and ERA5 EDA. Then for each subsequent timestep  $t = 1, \dots, T$ , we sample  $X^t \sim p(X^t | X^{t-1}, X^{t-2})$ , autoregressively, conditioned on the previous two steps  $(X^{t-1}, X^{t-2})$ . This process can be repeated multiple times, and the multiple resulting sample trajectories can then be used to compute Monte Carlo estimates of probabilities and expectations of interest. This is a form of ensemble forecasting, which is a popular method in traditional NWP-based forecasting, because the joint distribution is extremely high-dimensional, and is thus intractable to represent explicitly.

## B. Data

### B.1. ERA5 training and evaluation data for GenCast

We trained GenCast on a dataset built from the ECMWF’s ERA5 archive (Hersbach et al., 2020), a large corpus of global reanalysis data. The following description of the ERA5 dataset is adapted directly from Lam et al. (2023). ECMWF’s ERA5 (Hersbach et al., 2020)<sup>5</sup> archive is a large corpus of

<sup>4</sup>“Analysis” refers to an estimate of the state of the atmosphere based on observations; “reanalysis” is an analysis computed retrospectively based on historical observations.

<sup>5</sup>See ERA5 documentation: <https://confluence.ecmwf.int/display/CKB/ERA5>.

data that represents the global weather from 1959 to the present, at 1 hour increments, for hundreds of static, surface, and atmospheric variables. The ERA5 archive is based on *reanalysis*, which uses ECMWF’s Integrated Forecast System (IFS) cycle 42r1 that was operational for most of 2016, with an ensemble 4D-Var data assimilation scheme. ERA5 assimilated 12-hour windows of observations, from 21-09 UTC and 09-21 UTC, as well as previous forecasts, into a dense representation of the weather’s state, for each historical date and time. The ERA5 archive consists of a deterministic reanalysis (ERA5) computed at  $0.28125^\circ$  native latitude/longitude resolution, and an associated ensemble reanalysis (the ERA5 Ensemble of Data Assimilations or ERA5 EDA), which consists of 9 ensemble members and 1 control member computed at a lower  $0.5625^\circ$  native resolution.

Our ERA5 dataset contains a subset of available variables in ECMWF’s ERA5 archive (Table B1), on a  $0.25^\circ$  equiangular grid, at 13 pressure levels<sup>6</sup> corresponding to the levels of the WeatherBench (Rasp et al., 2020) benchmark: 50, 100, 150, 200, 250, 300, 400, 500, 600, 700, 850, 925, and 1000 hPa. We subsampled the temporal resolution from 1 hour to 6 hours, corresponding to 00:00, 06:00, 12:00 and 18:00 UTC times each day. From this dataset, we extracted sequences at 12 hour temporal resolution (sequences of 00/12 UTC or 06/18 UTC times) to train GenCast.

Although its temporal resolution is hourly, ERA5 only assimilates observations in 12-hour windows, from 21 UTC–09 UTC and 09 UTC–21 UTC. This means that steps taken within a single 12h assimilation window have a different, less dispersed distribution to those which jump from one window into the next. By choosing a 12 hour time step we avoid training on this bimodal distribution, and ensure that our model always predicts a target from the next assimilation window.

For accumulated variables such as precipitation, instead of subsampling the data in time, we accumulated values over the 12 hour period preceding each time.

Our dataset covers the period of 1979 to 2019. During the development phase of GenCast, we used dates from 1979 to 2017 for training and validated results on 2018. Before starting the test phase, we froze all model and training choices, retrained the model on data from 1979 to 2018, and evaluated results on 2019. For the GraphCast-Perturbed baseline, we trained the deterministic GraphCast baseline with the protocol described in Lam et al. (2023) at  $0.25^\circ$  resolution, using data from 1979 to 2018, which is consistent with the approach to the data split for GenCast.

## B.2. Data preprocessing.

**Handling of ENS missing data.** When trying to download ENS forecasts for surface variables for the 2019-10-17 00:00 UTC initialisation, we were met with persistent errors, so we left that initialisation out of the ENS evaluation, and used neighboring information when performing paired statistical tests for differences in verification metrics (see Section E.2.6 for details).

**Variables with NaNs.** ERA5 sea surface temperature (SST) data contains NaNs over land by default. As preprocessing of the SST training and evaluation data, values over land are replaced with the minimum sea surface temperature seen globally in a subset of ERA5.

**Upsampling EDA analysis.** As described in C, the initialisation of the ensemble forecasts for GenCast and GraphCast-Perturbed utilises the ERA5 EDA dataset. Since ERA5 EDA exists only at  $0.5^\circ$  resolution, we bilinearly interpolate the EDA perturbations to  $0.25^\circ$  before adding them to the ERA5 inputs.

<sup>6</sup>We follow common practice of using pressure as our vertical coordinate, instead of altitude. A “pressure level” is a field of altitudes with equal pressure. E.g., “pressure level 500 hPa” corresponds to the field of altitudes for which the pressure is 500 hPa. The relationship between pressure and altitude is determined by the geopotential variable.

We noticed that for sea surface temperature (SST), which takes NaN values over land regions, after bilinear interpolation to  $0.25^\circ$ , the NaN locations of the EDA data and the NaN locations of ERA5 did not match exactly. We built the sea surface temperature inputs according to the NaN locations of ERA5 at  $0.25^\circ$ , and simply used ERA5 deterministic analysis SST for any points for which EDA SST values were not available.

Type	Variable name	Short name	ECMWF Parameter ID	Role (accumulation period, if applicable)
Atmospheric	Geopotential	z	129	Input/Predicted
Atmospheric	Specific humidity	q	133	Input/Predicted
Atmospheric	Temperature	t	130	Input/Predicted
Atmospheric	U component of wind	u	131	Input/Predicted
Atmospheric	V component of wind	v	132	Input/Predicted
Atmospheric	Vertical velocity	w	135	Input/Predicted
Single	2 metre temperature	2t	167	Input/Predicted
Single	10 metre u wind component	10u	165	Input/Predicted
Single	10 metre v wind component	10v	166	Input/Predicted
Single	Mean sea level pressure	msl	151	Input/Predicted
Single	Sea Surface Temperature	sst	34	Input/Predicted
Single	Total precipitation	tp	228	Predicted (12h)
Static	Geopotential at surface	z	129	Input
Static	Land-sea mask	lsm	172	Input
Static	Latitude	n/a	n/a	Input
Static	Longitude	n/a	n/a	Input
Clock	Local time of day	n/a	n/a	Input
Clock	Elapsed year progress	n/a	n/a	Input

Table B1 | **ECMWF variables used in our datasets.** The “Type” column indicates whether the variable represents a *static* property, a time-varying *single*-level property (e.g., surface variables are included), or a time-varying *atmospheric* property. The “Variable name” and “Short name” columns are ECMWF’s labels. The “ECMWF Parameter ID” column is a ECMWF’s numeric label, and can be used to construct the URL for ECMWF’s description of the variable, by appending it as suffix to the following prefix, replacing “ID” with the numeric code: <https://apps.ecmwf.int/codes/grib/param-db/?id=ID>. The “Role” column indicates whether the variable is something our model takes as input and predicts, or only uses as input context (the double horizontal line separates predicted from input-only variables, to make the partitioning more visible).

### B.3. Data Availability

- ERA5 and ERA5 EDA datasets were downloaded and are downloadable from the Climate Data Store (CDS) of the Copernicus Climate Change Service (<https://cds.climate.copernicus.eu>). The results contain modified Copernicus Climate Change Service information 2020. Neither the European Commission nor ECMWF is responsible for any use that may be made of the Copernicus information or data it contains.
- ENS and HRES data were downloaded and are downloadable from the ECMWF as of April 2024 (<https://apps.ecmwf.int/datasets/data/tigge/>), and usable according to the license described at <https://apps.ecmwf.int/datasets/licences/tigge/>. The data

forms part of the THORPEX Interactive Grand Global Ensemble (TIGGE) archive (<https://confluence.ecmwf.int/display/TIGGE>). TIGGE is an initiative of the World Weather Research Programme (WWRP).

- The Global Power Plant Database v1.3.0 was and can be downloaded from <https://datasets.wri.org/dataset/globalpowerplantdatabase>. The idealised wind turbine power curve was and can be downloaded from the National Renewable Energy Laboratory [https://github.com/NREL/turbine-models/blob/master/Onshore/WTK\\_Validation\\_IEC-2\\_normalized.csv](https://github.com/NREL/turbine-models/blob/master/Onshore/WTK_Validation_IEC-2_normalized.csv).

## C. Initial conditions

We explored a number of methods for deriving ensemble initial conditions for our ML models. In this section we discuss these methods in more detail in order to motivate the choices we made. We also supply full details of the ad-hoc Gaussian Process perturbations described in Section C.4.

### C.1. Deterministic analysis

We tried initialising every ensemble member in the same way, using two consecutive deterministic analyses from ECMWF’s ERA5 reanalysis dataset. This is a relatively crude approximation as it collapses initial condition uncertainty down to a pair of point estimates. A deterministic model initialised this way will have no dispersion, but the method works relatively well for our diffusion model. A comparison of the CRPS results reported in the main results section to those achieved when initialising with deterministic analysis is included in Section F.11.

### C.2. Ensemble of data assimilations (EDA) analysis

Another possibility is to initialise each ensemble member using two consecutive ensemble analyses from a corresponding ensemble member of ECMWF’s ERA5 EDA. This better approximates a posterior distribution conditional on observations. However it still tends to be under-dispersed (Buizza et al., 2008), and the ERA5 EDA was computed using IFS at half the native resolution used for ERA5 itself (Hersbach et al., 2020), reducing the quality of the analysis.

### C.3. Deterministic analysis plus EDA perturbations

Following ECMWF (Buizza et al., 2008) we combine the high quality of the deterministic analysis with the distributional information of the ensemble analysis, by taking the deterministic ERA5 analysis and adding to it perturbations equal to the difference between ERA5 EDA members and their mean. This is analogous to the use of EDA perturbations in initialising ECMWF’s ENS forecast system, although we do not include the additional singular value perturbations used at ECMWF to address under-dispersion of the EDA perturbations, largely because we were not easily able to obtain singular value perturbations for use with the ERA5 EDA dataset. Nevertheless this method yielded the best results for our diffusion model beyond the shortest lead times (Figure F28).

### C.4. Additional ad hoc Gaussian process perturbations

The final method we explored takes the deterministic ERA5 analysis with EDA perturbations and adds to it perturbations sampled from a zero-mean Gaussian process on the sphere. This process uses the Gaussian-like stationary isotropic correlation function from Weaver and Courtier (2001), with a horizontal decorrelation length-scale of 1200km.

Variable
Geopotential
Temperature
U component of wind
V component of wind
2-metre temperature

Table C1 | Variables to which Gaussian process perturbations are applied

We sample independent perturbations for each of the variables listed in Table C1; other variables are not perturbed by the Gaussian process. We obtained better results perturbing only this subset than the full set of input variables, although we have not exhaustively investigated the best subset of variables to perturb.

The marginal standard deviations of the perturbations are equal to 0.085 times those of 6-hour differences in the corresponding variables at each respective pressure (or surface) level. Aside from these differences in scale, for a given variable the same perturbation is used for all levels, and for both input timesteps. This is equivalent to infinite vertical and temporal decorrelation lengthscales. We investigated using lower vertical decorrelation lengthscales but found they did not help.

We selected the scale factor 0.085 and horizontal decorrelation length-scale 1200km based on CRPS scores for the resulting forecasts over a range of variables and lead times, after sweeping over scale factors (0.03, 0.05, 0.07, 0.085, 0.1, 0.3), and decorrelation length-scales (30km, 480km, 1200km, 3000km). Results were significantly worse at the shortest lengthscale we tried of 30km, but were not otherwise very sensitive to decorrelation lengthscale.

These perturbations are quite crude; in particular they are not flow-dependent and do not take any care to preserve physical invariants. Nevertheless we’ve found them to be surprisingly effective at longer lead times with the deterministic GraphCast model. In combination with EDA perturbations, they appear to play a similar role to the singular value perturbations used operationally at ECMWF to address the under-dispersion of EDA perturbations. They also allow us to generate ensembles of arbitrary size from deterministic GraphCast, without being limited by the size of the EDA ensemble. However as noted, with the diffusion model they do not give any additional skill over EDA perturbations alone, in fact for the diffusion model, skill is reduced when these perturbations are added with all but the smallest scale factors.

## D. Diffusion model specification

Our key innovation is to model  $p(X^t|X^{t-1}, X^{t-2})$  with a learned neural network-based diffusion model (Karras et al., 2022; Sohl-Dickstein et al., 2015; Song et al., 2021), which allows us to draw samples from it. Rather than sampling  $X^t$  directly, our approach is to sample a residual  $Z^t$  with respect to the most recent weather state  $X^{t-1}$ , where the residuals have been normalised to unit variance on a per-variable and per-level basis as was done for GraphCast in Lam et al. (2023).  $X^t$  is then computed as  $X^t = X^{t-1} + SZ^t$ , where  $S$  is a diagonal matrix which inverts the normalisation<sup>7</sup>.

We broadly follow the diffusion framework presented in Karras et al. (2022), and refer the reader to their paper for a more rigorous introduction to diffusion, as well as a detailed treatment of the

<sup>7</sup>An exception to this is precipitation, for which we set  $X^t = SZ^t$  without adding the previous state.

available modelling decisions. We adopt their choices of noise schedule, noise scaling, loss weighting by noise level, and preconditioning. However we make changes to the noise distribution, the training-time distribution of noise levels, and add additional loss weightings, all of which are described below. These changes improve performance on the task of probabilistic weather forecasting.

### D.1. Sampling process

The sampling process begins by drawing an initial sample  $Z_0^t$  from a noise distribution on the sphere  $p_{noise}(\cdot|\sigma_0)$  that is described in Section D.2, at a high initial noise level  $\sigma_0$ . After  $N$  steps of transformation we end up at  $Z_N^t := Z^t$ , our sample from the target distribution at noise level  $\sigma_N = 0$ . To take us from one to the other, we apply an ODE solver to the probability flow ODE described by Karras et al. (2022); Song et al. (2021). Each step of this solver is denoted by  $r_\theta$  (see Figure 1), with

$$Z_{i+1}^t = r_\theta(Z_i^t; X^{t-1}, X^{t-2}, \sigma_{i+1}, \sigma_i) \quad (\text{D1})$$

taking us from noise level  $\sigma_i$  to the next (lower) noise level  $\sigma_{i+1}$ , conditioned on  $(X^{t-1}, X^{t-2})$ .

We use the second-order DPMSolver++2S solver (Lu et al., 2022), augmented with the stochastic churn (again making use of  $p_{noise}$  from Section D.2) and noise inflation techniques used in Karras et al. (2022) to inject further stochasticity into the sampling process. In conditioning on previous timesteps we follow the Conditional Denoising Estimator approach outlined and motivated by Batzolis et al. (2021).

Each step  $r_\theta$  of the solver makes use of a learned denoiser  $D_\theta$  with parameters  $\theta$ , described in detail below (Section D.3). We take  $N = 20$  solver steps per generated forecast timestep. As we are using a second-order solver, each step  $r_\theta$  requires two function evaluations of the denoiser  $D_\theta$  (with the exception of the last step which requires only a single evaluation). This results in 39 function evaluations in total. See Section D.5 for further details including a full list of sampling hyperparameters.

### D.2. Noise distribution on the sphere

At the core of a diffusion model is the addition and removal of noise, drawn from some distribution  $p_{noise}(\cdot|\sigma)$  parameterized by noise level  $\sigma$ . When using diffusion to generate natural images (Ho et al., 2020),  $p_{noise}$  is usually chosen to be i.i.d. Gaussian, and much of the early theory around diffusion models was developed for the case of Gaussian white noise. A true white noise process on the sphere is isotropic or rotation-invariant, and is characterised by a flat spherical harmonic power spectrum in expectation. However these properties do not hold if we attempt to approximate it at finite resolution by sampling i.i.d. noise on the cells of our equiangular latitude-longitude grid. This is due to the greater density of cells near to the poles which results in more power at higher frequencies in the spherical harmonic domain.

Empirically we didn't find this to be a fatal problem; nonetheless we found we can obtain a small but consistent improvement using a different approach to noise sampling which is sensitive to the spherical geometry. We sample isotropic Gaussian noise in the spherical harmonic domain, with an expected power spectrum that is flat over the range of wavenumbers that our grid is able to resolve, and truncated thereafter. We then project it onto our discrete grid using the inverse spherical harmonic transform (Driscoll and Healy, 1994). The resulting per-grid-cell noise values are not independent especially near to the poles, but are approximately independent at the resolution resolved at the equator, and display the desired properties of isotropy and flat power spectrum.

### D.3. Denoiser architecture

To recap, our diffusion sampling process involves taking multiple solver steps  $r_\theta$ , and each solver step calls a denoiser  $D_\theta$  as part of its computation. We parameterise the denoiser  $D_\theta$  following [Karras et al. \(2022\)](#) as a preconditioned version of a neural network function  $f_\theta$ .

$$D_\theta(Z_\sigma^t; X^{t-1}, X^{t-2}, \sigma) := c_{skip}(\sigma) \cdot Z_\sigma^t + c_{out}(\sigma) \cdot f_\theta(c_{in}(\sigma)Z_\sigma^t; X^{t-1}, X^{t-2}, c_{noise}(\sigma)). \quad (D2)$$

Here  $Z_\sigma^t$  denotes a noise-corrupted version of the target  $Z^t$  at noise level  $\sigma$ , and  $c_{in}$ ,  $c_{out}$ ,  $c_{skip}$  and  $c_{noise}$  are preconditioning functions taken from Table 1 in [Karras et al. \(2022\)](#), with  $\sigma_{data} = 1$  due to the normalisation of the targets.

The architecture used for  $f_\theta$  is related to the GraphCast architecture described in [Lam et al. \(2023\)](#). To be precise, the Encoder and Decoder architectures stay the same, and those inputs to the encoder corresponding to the previous two timesteps are normalised to zero mean and unit variance in the same way. However, unlike in GraphCast, which uses a similar message-passing GNN for the Processor architecture as in the Encoder and Decoder, in GenCast the Processor is a graph transformer model operating on a spherical mesh which computes neighbourhood-based self-attention. Unlike the multimesh used in GraphCast, the mesh in GenCast is a 6-times refined icosahedral mesh as defined in [Lam et al. \(2023\)](#), with 41,162 nodes and 246,960 edges. The Processor consists of 16 consecutive standard transformer blocks ([Nguyen and Salazar, 2019](#); [Vaswani et al., 2017](#)), with feature dimension equal to 512. The 4-head self-attention mechanism in each block is such that each node in the mesh attends to itself and to all other nodes which are within its 32-hop neighbourhood on the mesh.

To condition on prior timesteps  $X^{t-1}, X^{t-2}$ , we concatenate these along the channel dimension with the input to be denoised, and feed this as input to the model. Conditioning on noise level  $\sigma$  is achieved by replacing all layer-norm layers in the architecture with conditional layer-norm ([Chen et al., 2021](#)) layers. We transform log noise levels into a vector of sine/cosine Fourier features at 32 frequencies with base period 16, then pass them through a 2-layer MLP to obtain 16-dimensional noise-level encodings. Each of the conditional layer-norm layers applies a further linear layer to output replacements for the standard scale and offset parameters of layer norm, conditioned on these noise-level encodings.

### D.4. Training the denoiser

At training time we apply the denoiser to a version of the target  $Z^t$  which has been corrupted by adding noise  $\epsilon \sim p_{noise}(\cdot|\sigma)$  at noise level  $\sigma$ :

$$Y^t = D_\theta(Z^t + \epsilon; X^{t-1}, X^{t-2}, \sigma). \quad (D3)$$

We train its output, denoted  $Y^t$ , to predict the expectation of the noise-free target  $Z^t$  by minimizing the following mean-squared-error objective weighted per elevation level and by latitude-longitude cell area,

$$\sum_{t \in \mathcal{D}_{train}} \mathbb{E} \left[ \lambda(\sigma) \frac{1}{|G||J|} \sum_{i \in G} \sum_{j \in J} w_j a_i (Y_{i,j}^t - Z_{i,j}^t)^2 \right], \quad (D4)$$

where

- $t$  indexes the different timesteps in the training set  $\mathcal{D}_{train}$ ,

- $j \in J$  indexes the variable, and for atmospheric variables the pressure level, i.e.  $J = \{z1000, z850, \dots, 2T, MSL\}$ ,
- $i \in G$  indexes the location (latitude and longitude coordinates) in the grid,
- $w_j$  is the per-variable-level loss weight, set as in Lam et al. (2023) with the additional sea surface temperature variable weighted at 0.01.
- $a_i$  is the area of the latitude-longitude grid cell, which varies with latitude, and is normalised to unit mean over the grid,
- $\lambda(\sigma)$  is the per-noise-level loss weight from Karras et al. (2022),
- the expectation is taken over  $\sigma \sim p_{train}, \epsilon \sim p_{noise}(\cdot; \sigma)$ .

Instead of using the log-normal distribution for  $p_{train}$  that is suggested in Karras et al. (2022), we construct a distribution whose quantiles match the noise-level schedule used for sample generation, assigning higher probability to noise levels which are closer together during sampling. Specifically its inverse CDF is:

$$F^{-1}(u) = \left( \sigma_{max}^{\frac{1}{\rho}} + u(\sigma_{min}^{\frac{1}{\rho}} - \sigma_{max}^{\frac{1}{\rho}}) \right)^{\rho}$$

and we sample from it by drawing  $u \sim U[0, 1]$ . At training time we use the same  $\rho$  as at sampling time, but a slightly wider range for  $[\sigma_{min}, \sigma_{max}]$ , values are in Table D2.

As in Lam et al. (2023) we weight the squared error made at each latitude-longitude grid cell by a per-variable-level loss weight, as well as the normalised area of that grid cell; this is also a departure from Karras et al. (2022).

Unlike GraphCast, which is fine-tuned by back-propagating gradients through 12 step trajectories (3 days with 6 hour steps) produced by feeding the model its own inputs during training, GenCast is only ever trained using targets that consist of the next 12 hour state, without ever being provided its own predictions on previous steps as inputs.

#### D.4.1. Resolution training schedule

The results reported in this paper were generated by a model which was trained in a two-stage process. Stage one was a pre-training stage, taking 2 million training steps. During this stage, the ground truth dataset was bi-linearly downsampled from  $0.25^\circ$  to  $1^\circ$ , and the denoiser architecture used a 5-refined icosahedral mesh. This training stage takes a little over 3.5 days using 32 TPUv5 instances. After this training phase was complete, Stage 2 was conducted, fine-tuning the model to  $0.25^\circ$ , taking 64 000 further training steps. This takes just under 1.5 days using 32 TPUv5 instances. During Stage two, the ground truth data is kept at  $0.25^\circ$ , and the denoiser architecture is updated to take in  $0.25^\circ$  data and output  $0.25^\circ$  outputs, and to operate on a 6-refined icosahedral mesh. The GNN and graph-transformer architectures are such that the same model weights can operate on the higher data and mesh resolutions without any alterations. We do, however, make one minor modification before beginning the fine-tuning stage, in order to decrease the shock to the model of operating on higher resolution data. In the Encoder GNN, which performs message passing between the grid and mesh nodes, when the data resolution increases from  $1^\circ$  to  $0.25^\circ$ , the number of messages being received by each mesh node increases by a factor of 16. To approximately preserve the scale of the incoming signal to all mesh nodes at the start of finetuning, we therefore divide the sum of these message vectors by 16. The optimisation hyperparameters used for both stages of training are detailed in Table D1.

Optimiser	AdamW (Loshchilov and Hutter, 2018)
LR decay schedule	Cosine
Stage 1: Batch size	32
Stage 1: Warm-up steps	1e3
Stage 1: Total train steps	2e6
Stage 1: Peak LR	1e-3
Stage 1: Weight decay	0.1
Stage 2: Batch size	32
Stage 2: Warm-up steps	5e3
Stage 2: Total train steps	64000
Stage 2: Peak LR	1e-4
Stage 2: Weight decay	0.1

Table D1 | Diffusion model training hyperparameters.

### D.5. Sampler hyperparameters

To draw samples we use DPMSolver++2S (Lu et al., 2022) as a drop-in replacement for the second-order Heun solver used in Karras et al. (2022). It is also a second-order ODE solver requiring  $2N - 1$  function evaluations for  $N$  noise levels (two per step, one fewer for the final Euler step). We augment it with the stochastic churn and noise inflation described in Algorithm 2 of Karras et al. (2022).

At sampling time we adopt the noise level schedule specified by Karras et al. (2022):

$$\sigma_i := \left( \sigma_{max}^{\frac{1}{\rho}} + \frac{i}{N-1} (\sigma_{min}^{\frac{1}{\rho}} - \sigma_{max}^{\frac{1}{\rho}}) \right)^{\rho} \quad \text{for } i \in \{0 \dots N-1\}.$$

Settings for the parameters of this schedule ( $\rho, \sigma_{min}, \sigma_{max}, N$ ) as well for stochastic churn and noise inflation are given in Table D2.

Name	Notation	Value, sampling	Value, training
Maximum noise level	$\sigma_{max}$	80	88
Minimum noise level	$\sigma_{min}$	0.03	0.02
Shape of noise distribution	$\rho$	7	7
Number of noise levels	$N$	20	
Stochastic churn rate	$S_{churn}$	2.5	
Churn maximum noise level	$S_{tmax}$	80	
Churn minimum noise level	$S_{tmin}$	0.75	
Noise level inflation factor	$S_{noise}$	1.05	

Table D2 | **Settings used at sampling time, and their equivalents at training time where applicable.** Notation aligns with that used in Karras et al. (2022).

## E. Supplementary evaluation details

### E.1. ENS initialisation and evaluation times

As discussed in Section 4, we only evaluate GenCast on forecasts initialised at 06/18 UTC, since using 00/12-initialised forecasts gives GenCast an additional advantage (see Figure F31) due to the longer data-assimilation lookahead. Ideally we would compare all models at the same 06/18 UTC initialisation times, however ENS forecasts from 06/18 UTC are only archived up to 6-day lead times and are not free for public download. Hence we evaluate ENS on forecasts initialised at 00/12 UTC. For globally averaged metrics this should not matter, and in fact Lam et al. (2023) found that 00/12 UTC initialisation tends to give a small advantage in RMSE to the deterministic HRES forecast over the 06/18 UTC initialisation, and we expect a similar minor advantage to apply to ENS. However, the regional wind power evaluation (Section 8.2) is sensitive to the diurnal cycle since wind power capacity is sparsely and non-uniformly distributed around the world. Thus in this case it is important to compare forecasts by ENS and GenCast at the same set of validity times. We therefore evaluate ENS (initialised at 00/12 UTC) at the same 06/18 UTC targets as GenCast. However, GenCast produces 06/18 UTC forecasts at lead times of 12 hours, 24 hours, 36 hours, ..., while for ENS we only obtain 06/18 UTC forecasts at lead times of 6 hours, 18 hours, 30 hours, and so on. In order to estimate ENS's 06/18 UTC regional wind power CRPS at the same lead times as GenCast, we linearly interpolate ENS's CRPS curve. In Section F.12.2 we validate this approach on 2018 data where we did get access to ENS 06/18 UTC initialisations, showing that this lead time interpolation in fact overestimates the performance of ENS, in particular at short lead times.

### E.2. Verification metrics

In the following, for a particular variable, level and lead time,

- $x_{i,k}^m$  denotes the value of the  $m$ th of  $M$  ensemble members in a forecast from initialisation time indexed by  $k = 1 \dots K$ , at latitude and longitude indexed by  $i \in G$ .
- $y_{i,k}$  denotes the corresponding verification target.
- $\bar{x}_{i,k} = \frac{1}{M} \sum_m x_{i,k}^m$  denotes the ensemble mean.
- $a_i$  denotes the area of the latitude-longitude grid cell, which varies by latitude and is normalized to unit mean over the grid.

#### E.2.1. CRPS

The Continuous Ranked Probability Score (CRPS, see e.g. Gneiting and Raftery (2007)) is estimated for our ensembles as follows:

$$\text{CRPS} := \frac{1}{K} \sum_k \frac{1}{|G|} \sum_i a_i \left( \frac{1}{M} \sum_m |x_{i,k}^m - y_{i,k}| - \frac{1}{2M^2} \sum_{m,m'} |x_{i,k}^m - x_{i,k}^{m'}| \right). \quad (\text{E1})$$

For CRPS, smaller is better.

Here we use the traditional estimator of CRPS, which estimates the expected CRPS of the empirical distribution of a finite ensemble of size  $M$ . An alternative is the ‘fair’ CRPS estimator (Zamo and Naveau, 2018), which estimates the CRPS that would be attained in the limit of an infinite ensemble. In our case this would not be appropriate as we make use of precomputed NWP ensemble analyses of finite size, and we do not wish to assume that they can be scaled up arbitrarily. Although we can scale up our own ensembles more cheaply, in doing so we must repeatedly re-use the same set of NWP ensemble analysis members, and the fair CRPS estimator would not correctly model this reuse.

### E.2.2. Ensemble mean RMSE

This is defined as:

$$\text{EnsembleMeanRMSE} := \sqrt{\frac{1}{K} \sum_k \frac{1}{|G|} \sum_i a_i (y_{i,k} - \bar{x}_{i,k})^2}, \quad (\text{E2})$$

and again smaller is better.

### E.2.3. Spread/skill ratio

Following Fortin et al. (2014) we define spread as the root mean estimate of ensemble variance given below, and skill as the Ensemble-Mean RMSE from Equation (E2):

$$\text{Spread} := \sqrt{\frac{1}{K} \sum_k \frac{1}{|G|} \sum_i a_i \frac{1}{M-1} \sum_m (x_{i,k}^m - \bar{x}_{i,k})^2}, \quad (\text{E3})$$

$$\text{Skill} := \text{EnsembleMeanRMSE}. \quad (\text{E4})$$

Under these definitions and the assumption of a perfect forecast where ensemble members and ground truth  $\{x_{i,k}^1, \dots, x_{i,k}^M, y_{i,k}\}$  are all exchangeable, Fortin et al. (2014) Equation 15 shows that

$$\text{Skill} \approx \sqrt{\frac{M+1}{M}} \text{Spread}, \quad (\text{E5})$$

which motivates the following definition of spread/skill ratio including a correction for ensemble size:

$$\text{SpreadSkillRatio} := \sqrt{\frac{M+1}{M}} \frac{\text{Spread}}{\text{Skill}}. \quad (\text{E6})$$

Under the perfect forecast assumption then, we expect to see  $\text{SpreadSkillRatio} \approx 1$ . While diagnosis of under- or over-dispersion is confounded by forecast bias (Hamill, 2001; Wilks, 2011), if we assume such bias is relatively small, we can associate under-dispersion on average with  $\text{spread/skill} < 1$  and over-dispersion on average with  $\text{spread/skill} > 1$ .

### E.2.4. Rank histogram

The rank histogram (Talagrand, 1999) measures where the ground truth value tends to fall with respect to the ensemble distribution. More precisely, for each evaluation time and for each grid cell, we record the rank of the ground truth among the forecast ensemble members, from 1 to  $M+1$ , where  $M$  is the ensemble size, and plot the histogram of these ranks. For perfect ensemble forecasts in which ensemble members and ground truth are all exchangeable, we expect to see a flat rank histogram, since the true value should fall between any pair of proximal sorted ensemble values with equal probability. If we assume relatively small bias, rank histograms can be used to diagnose under- or over-dispersion (Hamill, 2001; Wilks, 2011). Under-dispersion will tend to result in the rank of the ground truth falling towards or beyond the outer bounds of the ensembles' values, resulting in a rank histogram with a U-shape. Conversely, an over-dispersed but unbiased ensemble will result in the ground truth falling predominantly near the center of the range of ensemble values, causing the rank histogram to have a  $\cap$ -shape. Peaks on either side of the rank histogram can suggest over- or under- prediction bias.

### E.2.5. Brier skill score

Suppose now that predictions  $x_{i,k}^m \in \{0, 1\}$  and targets  $y_{i,k} \in \{0, 1\}$  are binary variables, such as whether or not one is close to a cyclone, or whether surface temperature exceeds the 99.9th percentile of climatology.

Our ensemble means  $\bar{x}_{i,k}$  now correspond to empirical predictive probabilities for the events in question, and are scored by the Brier score as follows:

$$\text{BrierScore} := \frac{1}{K} \sum_k \frac{1}{|G|} \sum_i a_i (\bar{x}_{i,k} - y_{i,k})^2 \quad (\text{E7})$$

As with CRPS this is chosen to score the empirical probabilities of an ensemble of a specific finite size. While estimators exist for the Brier score attained by the true underlying probability of an infinite ensemble, these are not appropriate in our case for the same reason described above.

To obtain a Brier skill score, this is then normalized relative to the Brier score attained by predicting a fixed (and location-independent) climatological probability of the event, estimated using the evaluation set:

$$p_{clim} := \frac{1}{K} \sum_k \frac{1}{|G|} \sum_i a_i y_{i,k} \quad (\text{E8})$$

$$\text{BrierScore}_{clim} := \frac{1}{K} \sum_k \frac{1}{|G|} \sum_i a_i (p_{clim} - y_{i,k})^2 \quad (\text{E9})$$

$$\text{BrierSkillScore} := 1 - \frac{\text{BrierScore}}{\text{BrierScore}_{clim}} \quad (\text{E10})$$

Brier skill score is 0 for the climatological forecast and 1 for a perfect forecast, so larger is better.

### E.2.6. Relative Economic Value

The Brier score evaluates predictive probabilities without regard for the specific decision rule that will be used to act on those probabilities. In doing so it implicitly places much weight on decision thresholds that are not relevant in practice, especially in decision-making about extreme events, where it is often worth making preparations even given a small probability of the event in question.

To remedy this situation, Relative Economic Value has been proposed by [Richardson \(2000, 2006\)](#); [Wilks \(2001\)](#), based on the well-studied cost-loss ratio decision model ([Murphy, 1977](#); [Thompson, 1952](#)) for forecasts of binary events. This model allows us to assess the value of a forecast to a range of users facing different decision problems—from those who will act on a relatively small probability of a severe event, to those who will only act once the event is predicted with confidence.

In this model, a user must decide whether or not to prepare for an adverse weather event. Facing the event unprepared incurs an expense  $L$  (the ‘loss’). However, this loss can be avoided by preparing for the event with an expense  $C$  (the ‘cost’), as reflected in [Table E1](#):

The optimal strategy is to take action whenever the probability of the event exceeds  $C/L$ . This ‘cost-loss ratio’ is thus sufficient to characterise the decision problem faced by a particular user. Since it may vary significantly for different users, we display results for a range of cost-loss ratios. For severe weather events we will focus in particular on small cost-loss ratios (on the order of 0.01 to 0.2 for example) since these are more typical in practice, see [Katz and Murphy \(1997\)](#) for a number of examples.

	Event doesn't happen	Event happens
No preparation made	0	$L$
Preparation made	$C$	$C$

Table E1 | Expenses under the cost-loss decision model.

Under this model the expected expense of a decision system can be computed in terms of its confusion matrix, consisting of the proportions of true and false positives and negatives incurred (denoted TP, TN, FP, FN).

To make binary decisions based on our ensemble, we select a probability threshold  $q$ , and make a positive prediction whenever our empirical predictive probability  $\bar{x}_{i,m}$  exceeds  $q$ , obtaining binary forecasts:

$$x_{i,k} := \mathbb{1}[\bar{x}_{i,k} > q]. \quad (\text{E11})$$

We then compute the confusion matrix weighted by grid cell area:

$$\begin{bmatrix} \text{TN} & \text{FN} \\ \text{FP} & \text{TP} \end{bmatrix} := \frac{1}{K} \sum_k \frac{1}{|G|} \sum_i a_i \begin{bmatrix} (1-x_{i,k})(1-y_{i,k}) & (1-x_{i,k})y_{i,k} \\ x_{i,k}(1-y_{i,k}) & x_{i,k}y_{i,k} \end{bmatrix} \quad (\text{E12})$$

Multiplying the entries of this confusion matrix with the expenses in Table E1 and summing, we can then compute the expected expense incurred as:

$$E_{forecast} = (\text{TP} + \text{FP}) \cdot C + \text{FN} \cdot L. \quad (\text{E13})$$

To derive relative economic value (REV), we normalize this relative to the expense  $E_{clim}$  incurred by a constant forecast (whose value is chosen based only on the climatological base rate of the event), and the expense  $E_{perfect}$  incurred by a perfect forecast. In other words, REV compares how much expense you save using the forecasts instead of relying on climatology, relative to how much it would have been possible to save if you had the perfect forecast.

Never preparing will incur expense equal to either  $(\text{TP} + \text{FN}) \cdot L$  (because  $\text{TP} + \text{FN}$  is the base rate of the event), whereas always preparing will incur an expense  $C$ . Choosing the better of these strategies yields

$$E_{clim} = \min\{(\text{TP} + \text{FN}) \cdot L, C\}, \quad (\text{E14})$$

while with a perfect forecast, one only needs to prepare when the event is actually going to occur, incurring an expense

$$E_{perfect} = (\text{TP} + \text{FN}) \cdot C. \quad (\text{E15})$$

REV is then defined as

$$\text{REV}(C/L, q) := \frac{E_{clim} - E_{forecast}}{E_{clim} - E_{perfect}}, \quad (\text{E16})$$

and is 0 for a forecast based on climatology alone and 1 for a perfect forecast, so larger is better. Note that by dividing each term in Equation (E16) by  $L$ , the definition of REV depends on  $C$  and  $L$  only through the cost-loss ratio  $C/L$ .

It also depends on the probability threshold  $q$  that was chosen earlier. When probabilities are perfectly calibrated, it is optimal to set  $q = C/L$ . In practice ensemble forecast systems are rarely

perfectly calibrated, and we are more interested in the potential REV obtainable by a system after its probabilities have been optimally recalibrated. We follow [Richardson \(2000\)](#) in approximating this by computing REV at every possible threshold for the empirical predictive probability of our size- $M$  ensemble, and taking the maximum REV over these:

$$\text{REV}^*(C/L) := \max_{j=0, \dots, M+1} \text{REV}\left(C/L, q = \frac{j-1/2}{M}\right) \quad (\text{E17})$$

It is this maximum or potential REV that we report throughout; for the sake of conciseness we refer to it just as REV. Note that it is impossible to do worse than climatology on this metric, since both options available to the climatological forecast (never preparing and always preparing) are included in the maximization above. Thus  $0 \leq \text{REV}^* \leq 1$  always holds, and it is common to see values equal to zero when a forecast does not improve on climatology.

### E.3. Statistical tests

We compare GenCast with ENS on a number of verification metrics (detailed in Section E.2) computed on our 2019 evaluation set. For each relevant metric (and where applicable at each lead time, level, quantile and cost-loss ratio), we test the null hypothesis of no difference in the metric between GenCast and ENS, against the two-sided alternative. Specifically we are testing for differences in the values of the metrics that would be attained in the limit of infinite years of evaluation data, assuming stationarity of the climate.

Each of our verification metrics  $V$  can be viewed as a function of the mean of a time-series of statistics given for every initialisation time  $t$ , where these statistics have already been spatially averaged. The statistics used for each metric are given in Table E2.

Verification metric	Statistic time-series	Proxy used for block length selection
CRPS	CRPS	CRPS
Ensemble mean RMSE	Ensemble mean MSE	Ensemble mean MSE
Brier skill score	Brier score, base rate	BSS with constant denominator
REV*	Confusion matrix	REV with constant denominator and $q$ maximizing overall REV.

Table E2 | Time-series of statistics used by each verification metric.

To perform our test, we compute paired time-series of these statistics for both GenCast and ENS. We then resample the paired time-series 10000 times using the stationary block bootstrap of [Politis and Romano \(1994\)](#) implemented in [Sheppard et al. \(2024\)](#). We compute  $V_{\text{GenCast}} - V_{\text{ENS}}$  for each resample, and use these values to construct a  $(1 - \alpha) * 100\%$  confidence interval for the difference using the bias-corrected and accelerated ('bca') method of [Efron and Narasimhan \(2020\)](#). We reject the null hypothesis when this interval does not contain zero.

**Block length selection** In order to account for temporal dependence it is important to select an appropriate mean block length for the stationary block bootstrap. For this we use the automatic block length selection described in [Patton et al. \(2009\)](#); [Politis and White \(2004\)](#) and implemented by [Sheppard et al. \(2024\)](#). Block length selection is performed separately for each lead time, variable and level, and for each setting of the metric in question (such as cost-loss ratio or event threshold). Since the selection mechanism takes as input a univariate time-series and our paired time-series of statistics

are multivariate, we compute a suitable per-initialisation-time proxy  $V_k$  whose temporal mean is equal to or closely related to  $V$ , described in Table E2. We then use differences  $V_{GenCast,k} - V_{ENS,k}$  for block length selection.

**Alignment of GenCast and ENS time-series** As motivated in Section E.1, ENS is initialised at 00/12 UTC, and GenCast at 06/18 UTC, meaning that forecast initialisation times do not match between the two time-series of statistics. In order to align the two time-series when performing a paired test, we take one of two approaches:

- Pair statistics for GenCast with statistics for ENS that are based on a forecast initialisation time 6 hours earlier, and a validity time 6 hours earlier too (so maintaining the same lead time).
- Pair statistics for GenCast with the mean of two statistics for ENS: one taken from a forecast initialised 6 hours earlier and so with 6 hours additional lead time; another taken from a forecast initialised 6 hours later and so with 6 hours less lead time. Both forecasts thus have the same validity time as the corresponding GenCast forecast, and the lead time is the same on average. This method is used only in the results on regional wind power forecasting, where a similar adjustment is performed for the reported metrics themselves; these adjustments are described and motivated in more detail in Section E.1.

**Missing data.** For ENS, a single initialisation time is missing, as described in Section B.2. The statistics from Table E2 are imputed for this initialisation time based on a linear interpolation of the previous and next values.

#### E.4. Local surface extremes evaluation

We evaluate GenCast and ENS on the task of predicting when surface weather variables exceed high (99.99th, 99.9th and 99th) and low (0.01st, 0.1st and 1st) climatological percentiles. These percentiles are computed per latitude/longitude using 7 recent years of 6-hourly data from 2016 - 2022, taken from the corresponding ground truth dataset for each model (ERA5 for GenCast and HRES-fc0 for ENS). For each latitude/longitude, they correspond to return periods of approximately 7 years, 8 months and 25 days respectively.

#### E.5. Cyclone tracking

##### E.5.1. Cyclone evaluation

A common approach for evaluating *deterministic* cyclone trajectory forecasts is to initialise the tracker from cyclones' initial locations and to continue the tracks until they predict the disappearance of the cyclone. Then the track error is computed from these pairs of forecast cyclone tracks and ground truth cyclone tracks until one of them terminates (Magnusson et al., 2021). However, this approach does not measure ability to accurately predict cyclogenesis nor cyclone termination. Furthermore, this approach cannot be applied to ensemble forecasts because the temporal duration of cyclones can differ between ensemble members.

We use a probabilistic cyclone evaluation which overcomes these issues. First, we apply a cyclone tracker that processes forecasts independently from ground truth and captures cyclogenesis. We then extract strike probabilities from these cyclone tracks. Strike probability is a common output in probabilistic cyclone modelling (Magnusson et al., 2021), measuring the chance that a given location on earth has a cyclone passing within a certain distance at a given time. We compute REV from these

probabilities, which penalises incorrectly predicting the existence or non-existence of a cyclone, as well as errors in predictions of their positions. This probabilistic approach is well aligned with decision making, where it is vital to accurately know the risk of being affected by an incoming cyclone.

More specifically, we apply the same cyclone tracker, TempestExtremes (Section E.5.2), to each forecast generated by ENS and GenCast, downsampling ENS from a 6-hourly to 12-hour resolution for a fair comparison with GenCast. From these tracks we generate  $1^\circ$  resolution probability heatmaps for each time step, where the probability in each  $1^\circ$  cell is the fraction of ensemble members predicting a cyclone centre within that cell. We choose  $1^\circ$  as it corresponds to 111km at the equator, which is close to 120km, a common radius used for defining cyclone strike probability (Magnusson et al., 2021). We then run the tracker on chunks of HRES-fc0 and ERA5 of the same length as the forecast trajectories, yielding binary ground truth maps for each initialisation time and lead time. Finally, Relative Economic Value (REV) is computed for each model's forecasts using their respective ground truth.

As mentioned in the IBTrACS paper (Knapp et al., 2010), different cyclone trackers apply different detection criteria in the definition of cyclones, which can affect results substantially, confounding the evaluation of the accuracy of the underlying gridded predictions. Our use of the TempestExtremes cyclone tracker controls for this. TempestExtremes is an open-source tracker which requires physically consistent cyclone behaviour in the raw forecasts (Section E.5.2). We apply this same tracker in the same way to all models and ground truth analysis datasets (without tuning the tracker to optimise performance on a particular model). Our evaluation therefore minimises bias toward any particular model, isolating the relative quality of the raw forecasts (as opposed to the quality or sensitivity of the tracker or source of ground truth).

We note that due to differences between ERA5 and HRES-fc0, running the TempestExtremes cyclone tracker on each dataset produces different cyclone locations and counts. On average across 2019, ERA5 has 1.51 cyclones per timestep and HRES-fc0 has 1.85 cyclones per timestep, which gives HRES-fc0 a base rate that is 23% greater than ERA5. Figure E1 plots the total cyclone counts tracked in the ground truth dataset at each time of the year, for both ERA5 and HRES-fc0. However, REV accounts for this difference in base rates by virtue of its normalisations with respect to climatology and the perfect forecast (see Section E.2.6), and is thus a fair metric to use when comparing methods evaluated against different ground truths. Furthermore, GenCast still outperforms ENS beyond 1 day lead times even when using HRES-fc0 ground truth, which puts GenCast at a disadvantage (Figure F19).

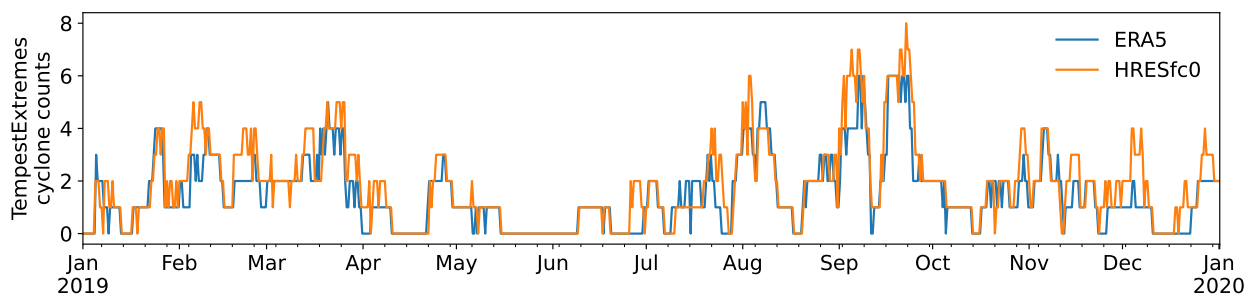


Figure E1 | Per-timestep TempestExtremes cyclone counts for ERA5 and HRES-fc0. The two time-series exhibit high correlation, but HRES-fc0 has 23% more cyclones than ERA5. The TempestExtremes tracker is applied to these analysis datasets as described in section E.5.2. We then arbitrarily picked a lead time of 4 days to extract cyclone count (all lead times 0-10 days yield very similar results).

### E.5.2. Cyclone tracker

To extract cyclone trajectories from gridded forecasts and analysis datasets, we use the TempestExtremes v2.1 cyclone tracking algorithm (Ullrich et al., 2021). TempestExtremes is open-source on GitHub<sup>8</sup> and has been used in a wide range of cyclone studies (Ullrich et al. 2021, Section 3.1). The algorithm has two stages described below (readers are referred to Section 3.2 of Ullrich et al. 2021 and Ullrich and Zarzycki 2017 for full details).

The first stage, *DetectNodes*, finds candidate tropical cyclones where minima in mean sea level pressure (MSL) are co-located with upper-level warm cores:

- Initial candidate locations are determined by local minima in MSL. Candidates within  $6^\circ$  of another stronger MSL minimum are eliminated.
- Each MSL minimum must be surrounded by a closed contour of MSL that is 200 hPa greater than the minimum. The minima must be sufficiently compact with this closed contour falling within a  $5.5^\circ$  great circle distance of the MSL minimum.
- A warm core criterion checks that candidate storms are co-located with maxima in the geopotential thickness field between 500 hPa and 300 hPa, Z500 - Z300. The maxima must be enclosed by a closed contour of thickness that is  $58.8 \text{ m}^2\text{s}^{-2}$  less than the maximum. The maxima must be sufficiently compact with this closed contour falling within a  $6.5^\circ$  great circle distance from the maximum.

The second stage, *StitchNodes*, detects plausible cyclone trajectories from these candidate cyclone locations by linking them together in time with the following criteria:

- Candidates cannot move more than an  $8^\circ$  great circle distance between subsequent time slices (the ‘stitch range’).
- Trajectories are allowed a maximum gap of 24 hours between candidate nodes; greater gaps result in a trajectory terminating (and potentially a new trajectory forming).
- To filter out short-lived storms that are not tropical cyclones, trajectories must last for at least 54 hours.
- A threshold analysis is performed on candidate trajectories to ensure cyclones are sufficiently intense and in the right locations on Earth: each trajectory must have at least 10 time slices with wind speed greater than  $10 \text{ ms}^{-1}$ , elevation below 150 m, and latitude between  $-50^\circ$  and  $50^\circ$ .

The algorithm’s default hyper-parameters were chosen so that when TempestExtremes is applied to 6-hourly reanalysis datasets the resulting tracks closely match observed tracks (Zarzycki and Ullrich, 2017), using the IBTrACS dataset as ground truth (Knapp et al., 2010). To account for the 12-hourly (instead of 6-hourly) temporal resolution in our evaluation, we changed two of the tracker’s *StitchNodes* hyperparameters. Firstly, we halved the number of time slices for the criteria checks from 10 to 5. Secondly, because cyclones can travel further in a 12 hour interval than in 6 hours, we increased the stitch range from an  $8^\circ$  to a  $12^\circ$  great circle distance. This value was chosen from visual inspection to trade-off fast-moving cyclones being cut off (if the stitch range is too small) and trajectories jumping between separate storms (if the stitch range is too large). Increasing the stitch range to  $12^\circ$  can sometimes result in nearby but separate storms being connected as part of the same cyclone trajectory (for example, in Figure G4g). However, we found this to be rare, and do not expect it to bias the results towards one particular model. All other TempestExtremes hyperparameters were left as their default values, and the same hyperparameters were used for each model and each analysis dataset.

<sup>8</sup><https://github.com/ClimateGlobalChange/tempestextremes>

Since TempestExtremes performs a global optimisation when stitching nodes, the tracker output at a particular lead time depends on raw predictions at nearby lead times. We prepend 10 days of the model’s respective ground truth (ERA5 or HRES-fc0) to each forecast before running the cyclone tracker. This avoids cyclones being dropped when forecasts are initialised close to the end of a cyclone’s lifetime, due to the short duration of cyclone within the forecast period not passing the tracker’s criteria. Similarly, we only report results up to lead times of 9 days despite providing 15 days of predictions to the tracker, because the tracker may drop cyclones that begin close to the end of the forecast period.

## E.6. Spatially pooled evaluation

The meteorological literature has produced a wide range of methods to verify spatial structure in weather forecasts (Gilleland et al., 2009). We use a neighbourhood (or ‘fuzzy’) approach, where forecasts and targets are first aggregated over regions of a particular spatial scale and standard skill scores computed on these pooled counterparts, with the process repeated at a range of spatial scales (Ebert, 2008; Ravuri et al., 2021). Neighbourhood methods often perform pooling using squares on a 2D latitude-longitude grid, which can lead to undesirable behaviour towards the poles and is not appropriate for evaluating global weather forecasts. Instead, we perform pooling on the surface of a sphere. We define pool centres as the nodes of a  $k$ -times refined icosahedral mesh, which are distributed approximately uniformly over the Earth’s surface. Pooling regions are defined within a fixed geodesic distance of each pool centre, with radii set to the mean distance between mesh nodes. To capture performance at different spatial scales, we do this separately for 6 mesh refinement levels ( $k = 7, 6, \dots, 2$ ), resulting in a wide range of pool sizes: 120 km, 241 km, 481 km, 962 km, 1922 km, and 3828 km (Figure E2)<sup>9</sup>, ranging from mesoscales to planetary scales.

We use two standard aggregation methods from the neighbourhood verification literature: average-pooling and max-pooling (Figure E3), which assess how well models predict statistics of the spatial distributions. Grid cells are weighted by their area when average-pooling. We then compute globally averaged CRPS from the pooled forecasts and ground truth. To account for slight non-uniformities in the distribution of pooling centres, we weight each pooling region by the area of the pooling centre’s Voronoi cell.

Average-pooling behaves like a low-pass filter, focusing the evaluation on increasingly large spatial structures as pooling size increases, and reducing the double-penalty problem at scales smaller than the pooling size. Max-pooling emphasises the positive tail of the spatial distribution, which may include high-impact events such as extreme wind or temperature that would otherwise be blurred by average-pooling. In some cases, forecast users perform max-pooling to account for possible location error, such as the location of a weather front for wind power ramp prediction (Drew et al., 2017).

Average- and max-pooled CRPS scores are computed on key surface variables at  $0.25^\circ$ : 2 m temperature, 10 m wind speed, 12h accumulated precipitation, and mean sea level pressure at  $0.25^\circ$  (Figure 4a, Figure F21, Figure F22). We also compute pooled CRPS scorecards for wind speed, geopotential, temperature, and specific humidity at all pressure levels (Figure F23–Figure F26). To reduce the computational cost of computing multiple pooled scorecards, forecasts and targets were subsampled to  $1^\circ$  before pooling. We skipped the smallest pool size because 120 km corresponds approximately  $1^\circ$  at the equator, making it similar to a univariate evaluation of the subsampled forecasts.

<sup>9</sup>For simplicity, we round these pool sizes to the nearest 10 in text and figures.

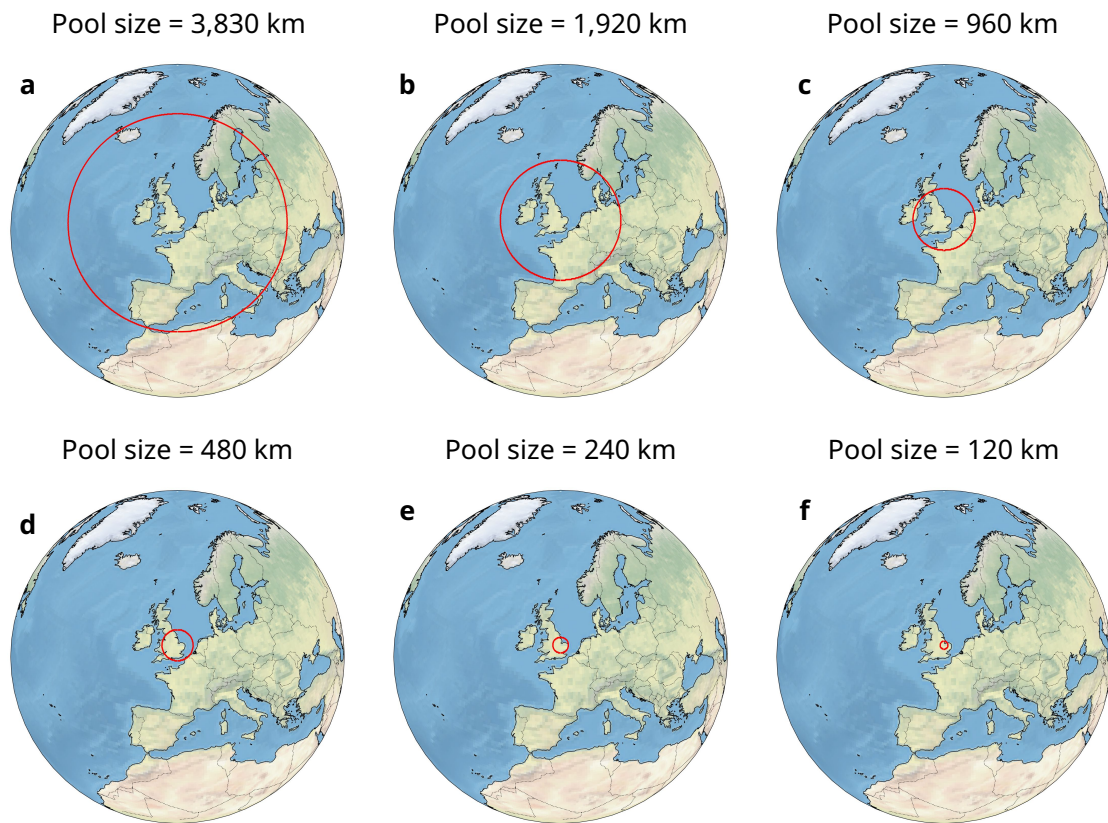


Figure E2 | Illustration of pool sizes. The sizes refer to the length of the shortest route (i.e. geodesic distance) from one side of the pooling region through the centre to the opposite side.

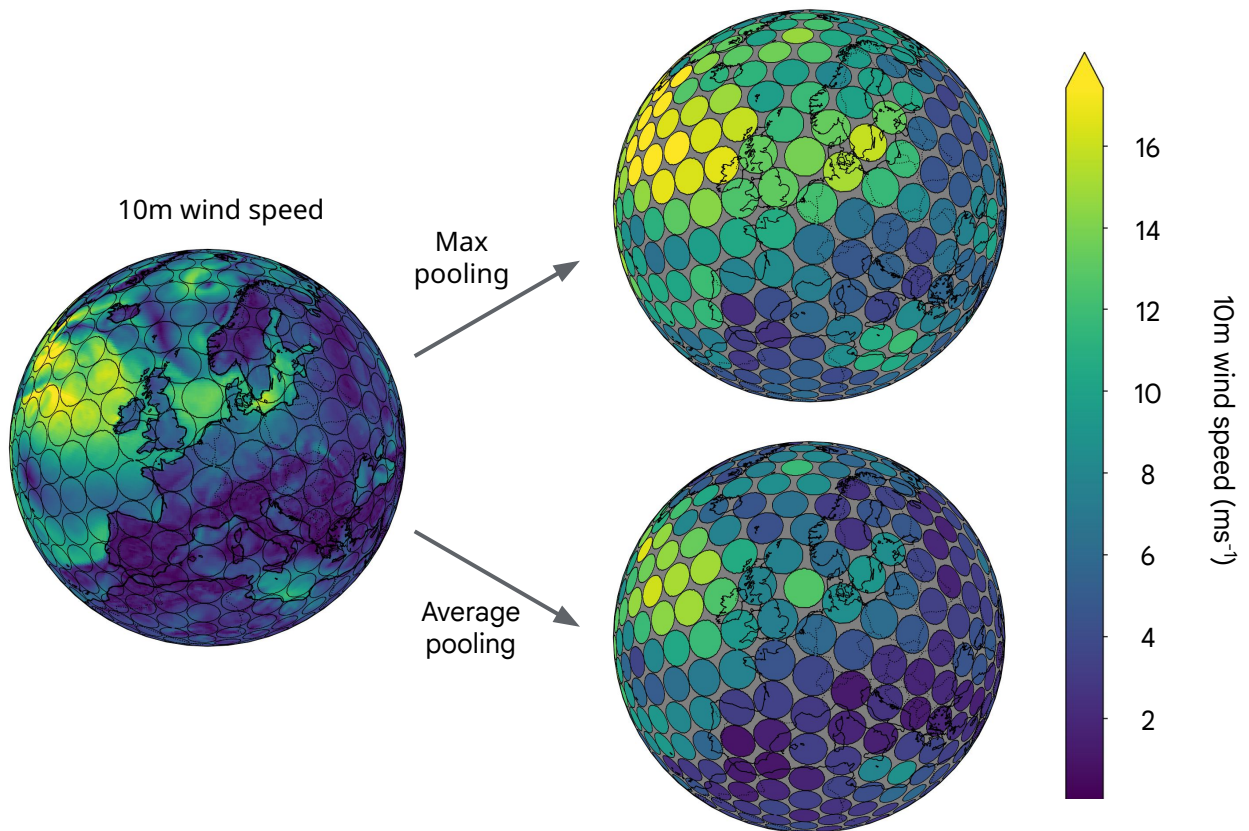


Figure E3 | Illustration of max-pooling and average-pooling on an icosahedral mesh. The pool size is 480 km. The overlap between pooling regions has been removed for visualisation purposes (Section E.6).

### E.7. Regional wind power forecasting evaluation

For the regional wind power forecasting experiment, we use all 5344 wind farm locations and their nominal capacities from the Global Power Plant Database (GPPD, [Byers et al. 2018](#), Figure E5)<sup>10</sup>. We first bilinearly interpolate 10 m wind speed forecasts and analysis states at each wind farm location. We then map 10 m wind speed to load factor—the ratio between actual wind turbine power output and maximum power output—using an idealised International Electrotechnical Commission Class II 2MW turbine power curve from the WIND Toolkit ([King et al., 2014](#)). This power curve has a cut-in speed of  $3 \text{ ms}^{-1}$ , maximum output at  $14 \text{ ms}^{-1}$ , and curtailment at  $25 \text{ ms}^{-1}$  (Figure E4). Load factor is then multiplied by nominal capacity to obtain idealised power generation in megawatts at each wind farm. This assumes no turbines are switched off due to maintenance or oversupply. Accounting for these additional complexities is beyond the scope of this study.

To generate random groupings of wind farms across the globe at a range of spatial scales, we use a similar procedure to the pooled evaluation in Section E.6. Pooling centres are defined on a 7-times refined icosahedral mesh and separate evaluations performed using pool sizes of 120 km, 240 km, and 480 km. The 120 km scale contains 3648 groups with a mean capacity of 272 MW, the 240 km scale contains 7759 groups with a mean capacity of 513 MW, and the 480 km scale contains 15913 groups with a mean capacity of 996 MW. Power output is summed over wind farm sites within each group and CRPS is computed for this derived quantity. We then compute average CRPS across all wind farm groups. By using power as the target variable, more weight is applied to pools containing more wind farm capacity in the global average CRPS.

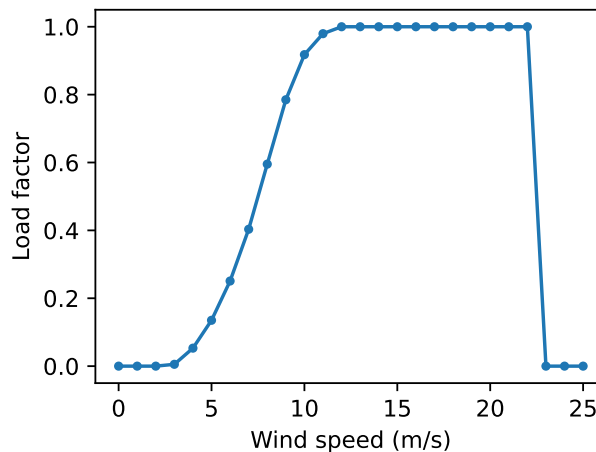


Figure E4 | International Electrotechnical Commission Class II turbine power curve from the WIND Toolkit ([King et al., 2014](#)).

<sup>10</sup>GPPD captures ~40% of all global wind farm capacity as of 2020 ([Byers et al., 2018](#)).

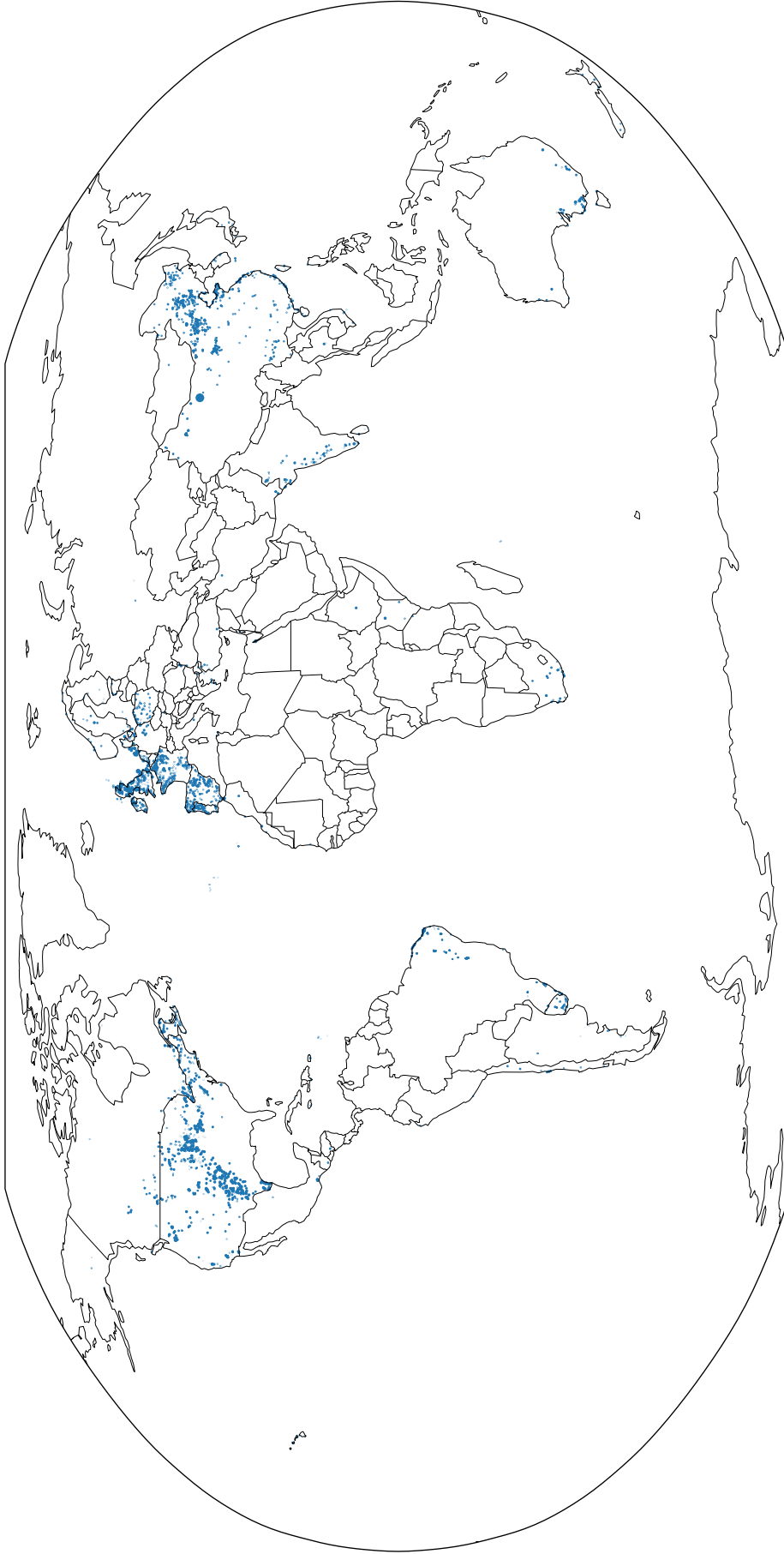


Figure E5 | Wind farm locations in the Global Power Plant Database (Byers et al., 2018) shown as blue markers, with marker size scaling with wind farm nominal capacity.

## F. Supplementary results

### F.1. CRPS line plots

We provide line plots on a set of representative variables for easier quantitative comparisons across models (Figure F1).

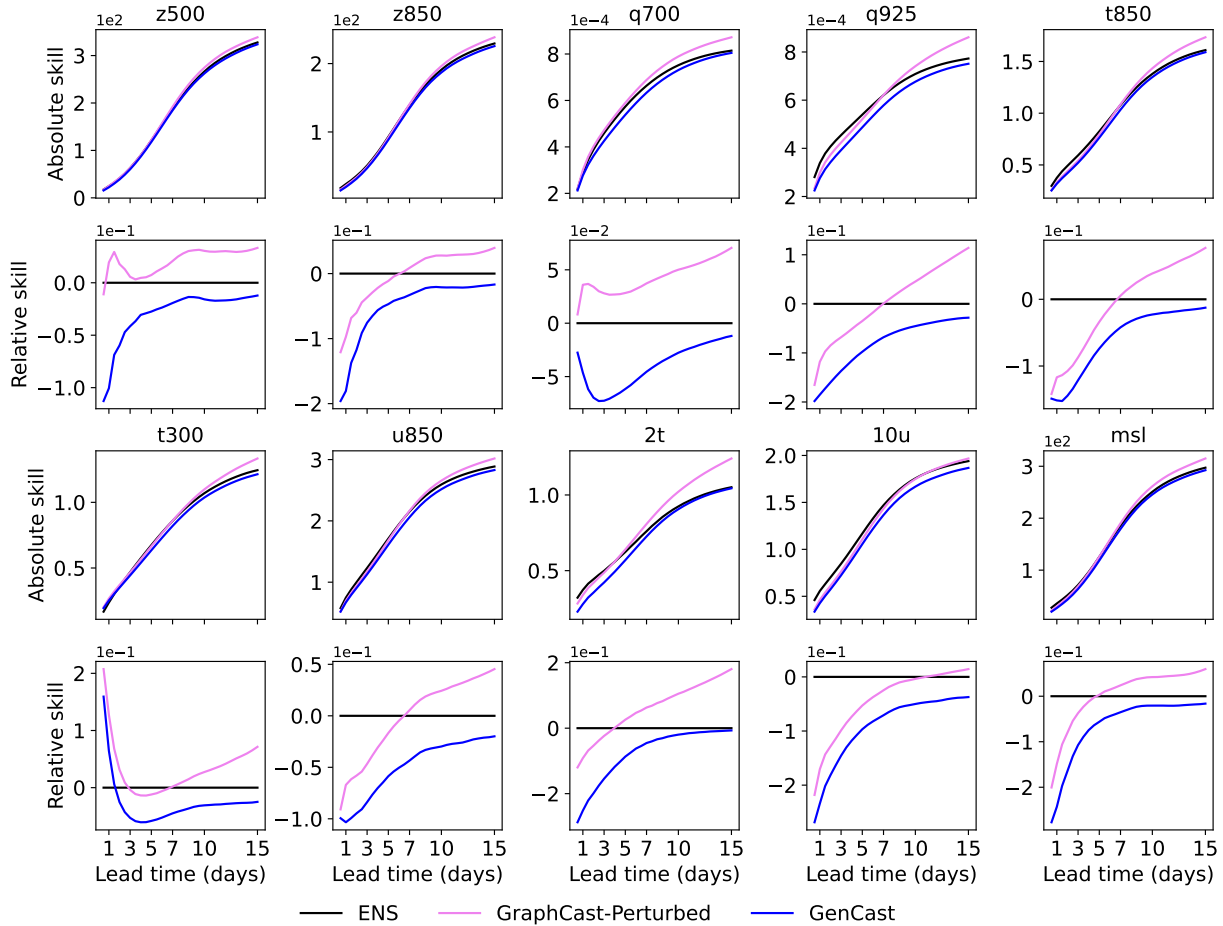


Figure F1 | Absolute and relative CRPS model comparison for z500, z850, q700, q925, t850, t300, u850, 2t, 10u and msl.

### F.2. Ensemble calibration

We find that, generally, GenCast’s spread/skill and rank histograms tend to be as good, or better, than ENS’s, and much better than that of GraphCast-Perturbed. Figure F2 compares spread/skill scores across lead times for a set of different variables and pressure levels. GenCast exhibits spread-skill scores close to 1 from 2-3 days onward. As noted in Section 4, over-dispersion at short lead times (as exhibited by GenCast) is an expected consequence of evaluating forecasts with uncertain initial conditions against a deterministic analysis ground truth. Spread/skill for ENS is also mostly quite close to one, with some exceptions like t300, q700, and 2t where it exhibits some under-dispersion. GraphCast-Perturbed shows substantial under-dispersion across almost all variables and lead times.

The rank histograms in Figure F3 and Figure F4 show that GenCast generally has very flat rank histograms from between 1 and 3 days lead time onward, in most cases flatter than those of ENS,

and in all cases flatter than GraphCast-Perturbed.

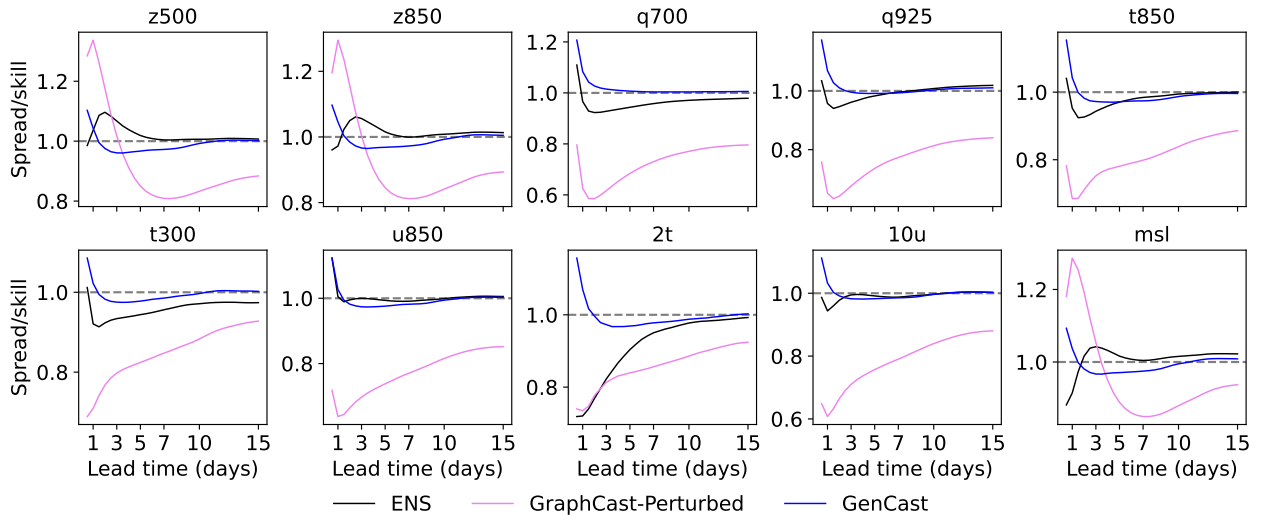


Figure F2 | Spread/skill ratio model comparison for z500, z850, q700, q925, t850, t300, u850, 2t, 10u and msl.

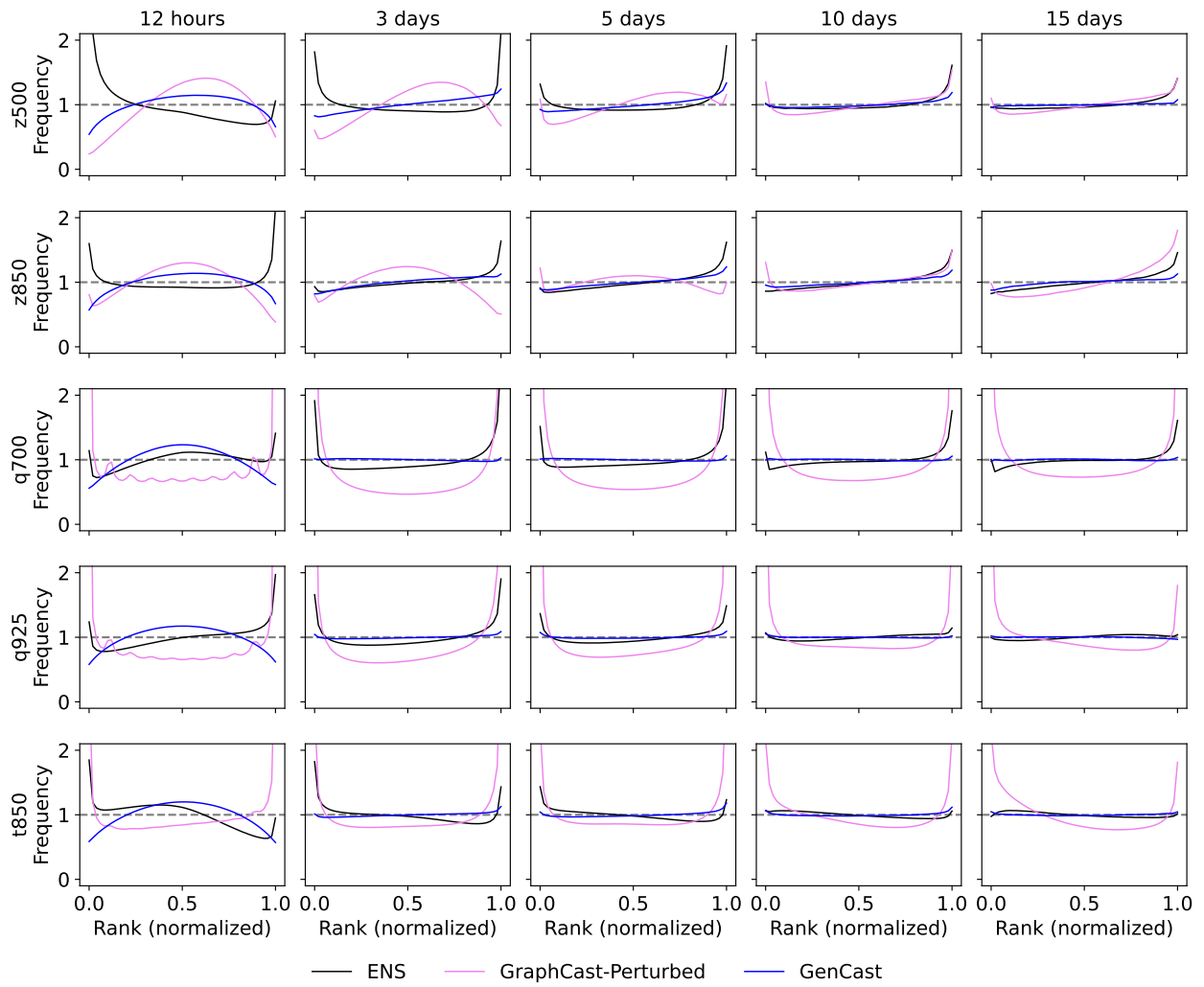


Figure F3 | Rank histogram model comparison for z500, z850, q700, q925 and t850.

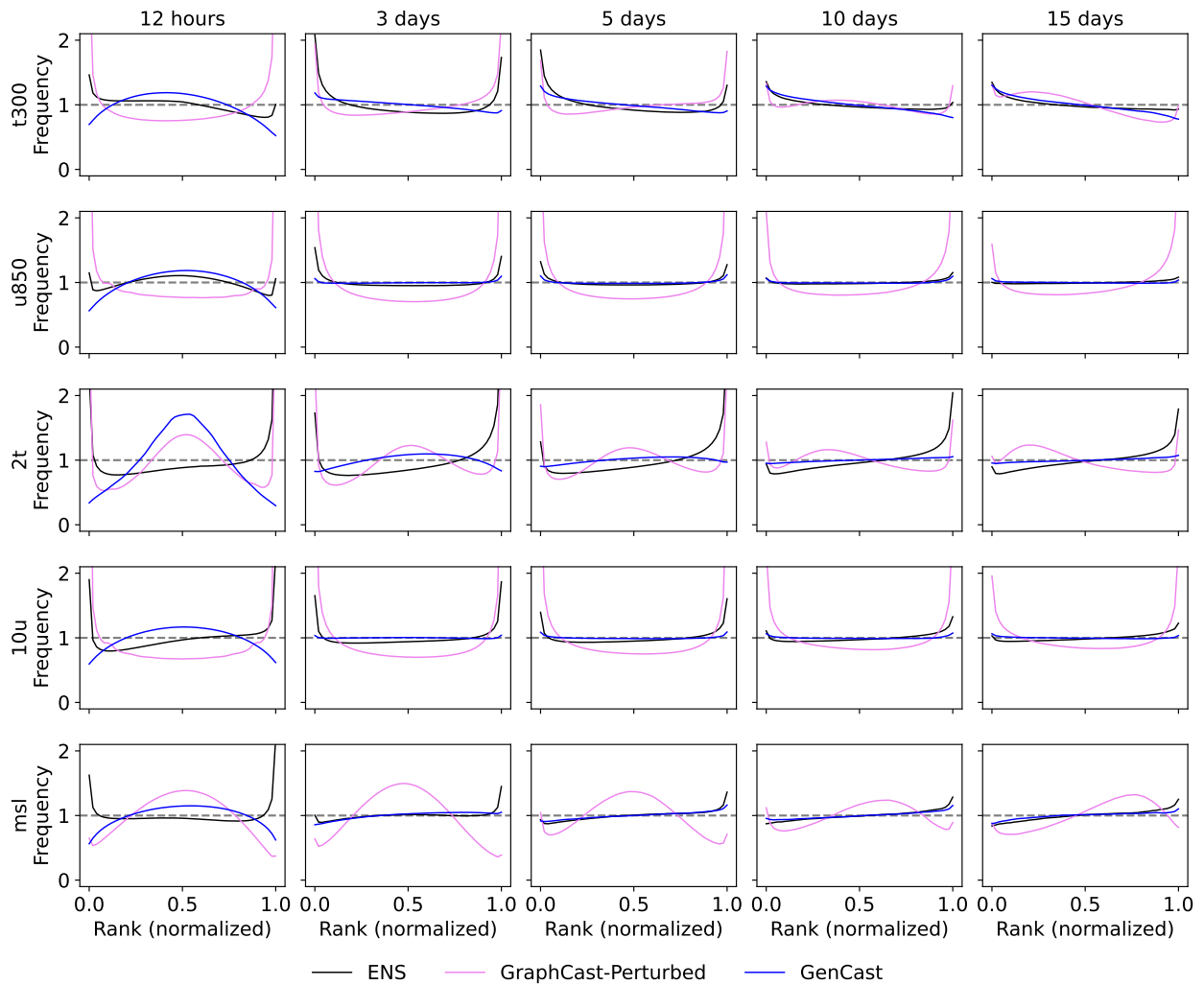


Figure F4 | Rank histograms model comparison for t300, u850, 2t, 10u and msl.

### F.3. Ensemble-Mean RMSE

Scorecards comparing the Ensemble-Mean RMSE are shown in Figure F5. The relative performance of GenCast compared to ENS is similar on Ensemble-Mean RMSE to what is observed for CRPS. GenCast is as good or better than ENS in 96% of cases, and significantly better ( $p < 0.05$ ) in 82% of cases. We also present some line plots for a subset of representative variables for easier quantitative comparison (Figure F6).

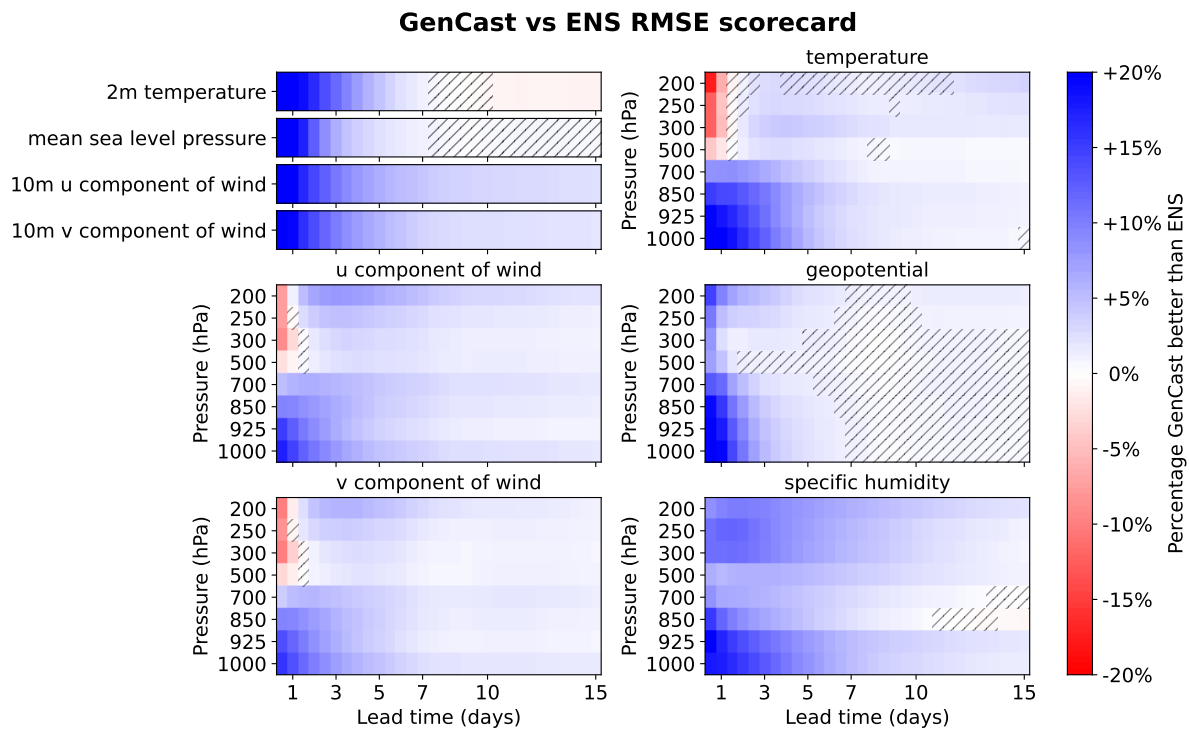


Figure F5 | Ensemble-mean RMSE scorecard comparing GenCast to ENS. Analogous to Figure 3 but displaying RMSE instead of CRPS. Hatched regions indicate where neither model is significantly better ( $p > 0.05$ ).

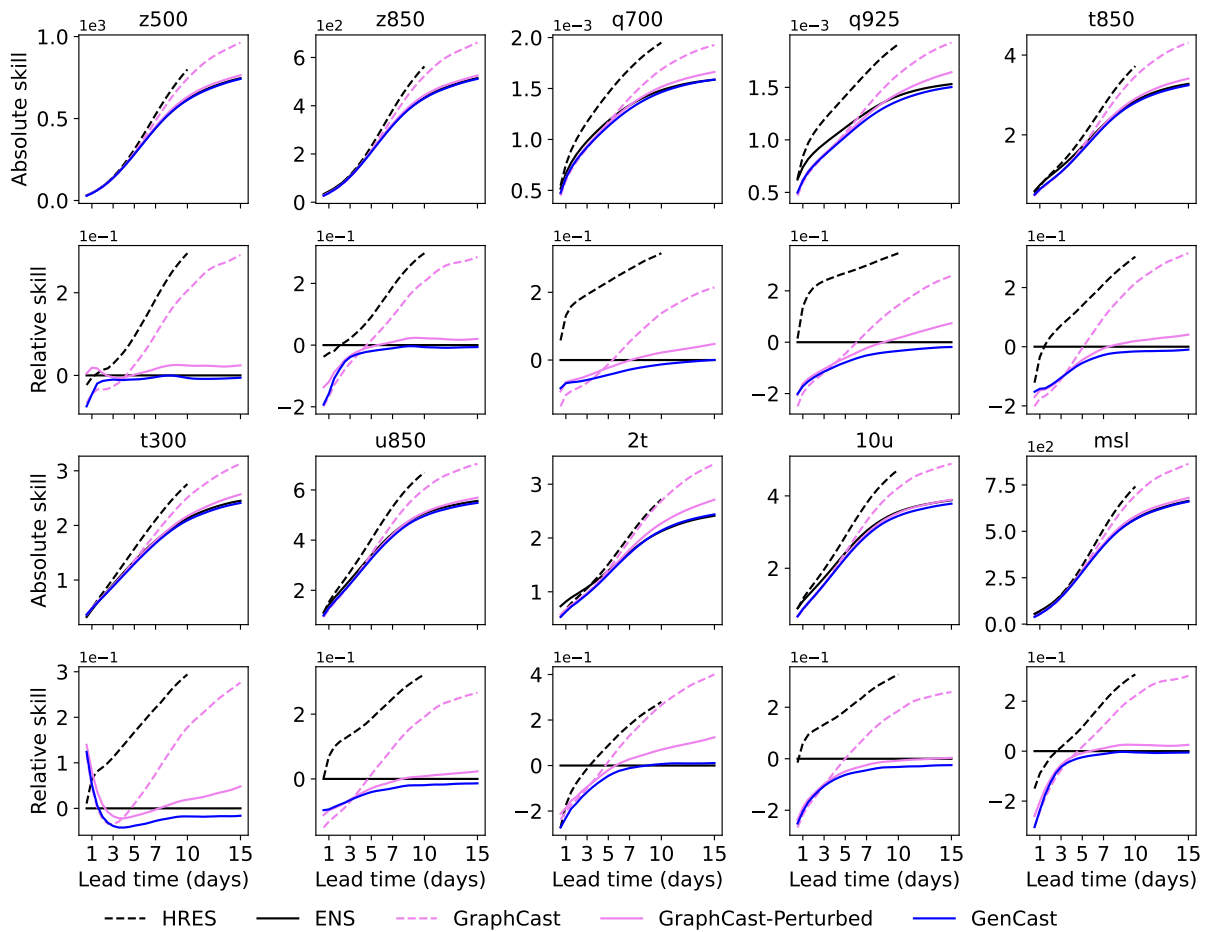


Figure F6 | Absolute and relative RMSE (Ensemble mean) model comparison for z500, z850, q700, q925, t850, t300, u850, 2t, 10u and msl.

#### F.4. Precipitation

In line with the rest of the paper, we evaluate precipitation forecasting skill using RMSE, CRPS and rank histograms. Since some of these metrics may not be representative of actual skill due to precipitation being highly sparse and very non-Gaussian, we also evaluated it using Stable Equitable Error in Probability Space (SEEPS) (Haiden et al., 2012; North et al., 2013; Rodwell et al., 2010), using the same methodology as in Lam et al. (2023). Because SEEPS is a metric for deterministic categorical forecasts (dry, light-rain, and heavy-rain) we evaluated the ensembles both computing the category of the ensemble mean, as well as the mode of the ensemble category members (i.e. majority vote). We repeat the caveats mentioned in the main text that we lack full confidence in the quality of ERA5 precipitation data, and that we have not tailored our evaluation to precipitation specifically beyond adding SEEPS as a further metric. Results for 24 hour and 12 hour accumulated precipitation are shown in Figure F7 and Figure F8 respectively.

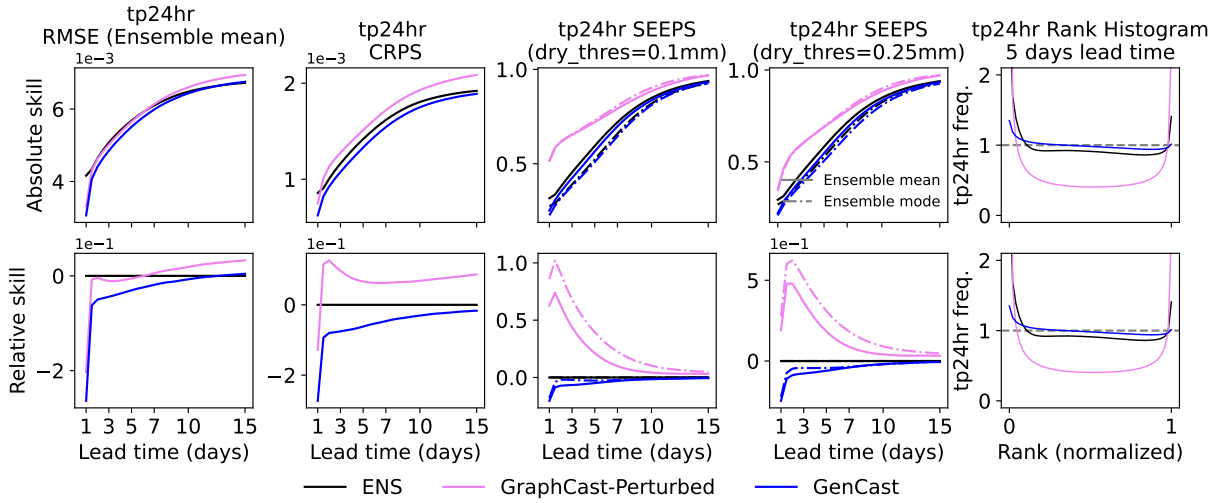


Figure F7 | Comparing preliminary results of model performance on predicted total accumulated precipitation over 24 hours, evaluated on Ensemble-Mean RMSE, CRPS, SEEPS with dry thresholds 0.1 and 0.25, and via rank-histogram. All metrics were calculated globally and over the full test period, except for SEEPS which excludes very dry regions according to the criteria in Lam et al. (2023). For ensembles, we evaluate SEEPS both on the mean of the ensemble, as well as using the mode of the dry, light-rain, and heavy-rain categories predicted by the different ensemble members (i.e. majority vote). Relative and absolute plots are shown in the top and bottom rows respectively. GenCast shows promising results, more often than not outperforming ENS and with a significantly flatter rank histogram.

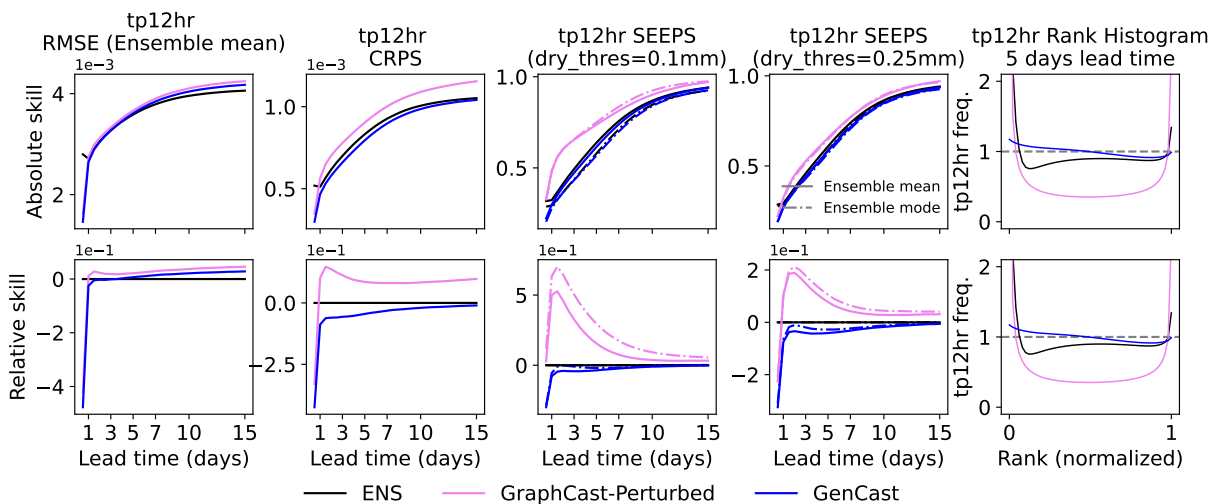


Figure F8 | Results analogous to Figure F7 on 12 hour precipitation.

## F.5. Spectrum for additional variables

We provide additional spectral results to supplement those the main paper, showing 10 representative variables: z500, z850, q700, q925, t850, t300, u850, 2t, 10u and msl (Figure F9, Figure F10).

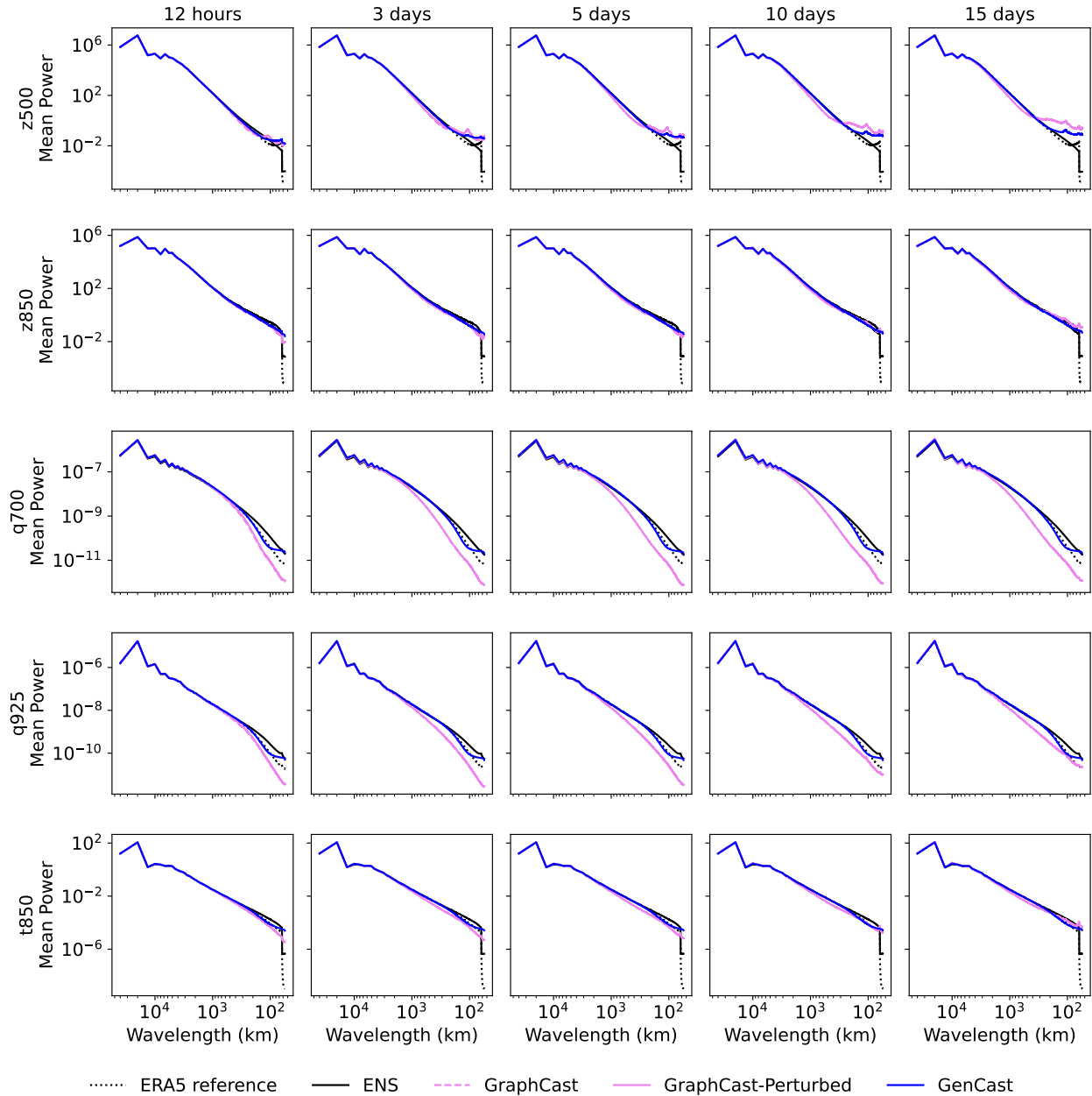


Figure F9 | Power spectrum plots for z500, z850, q700, q925 and t850.

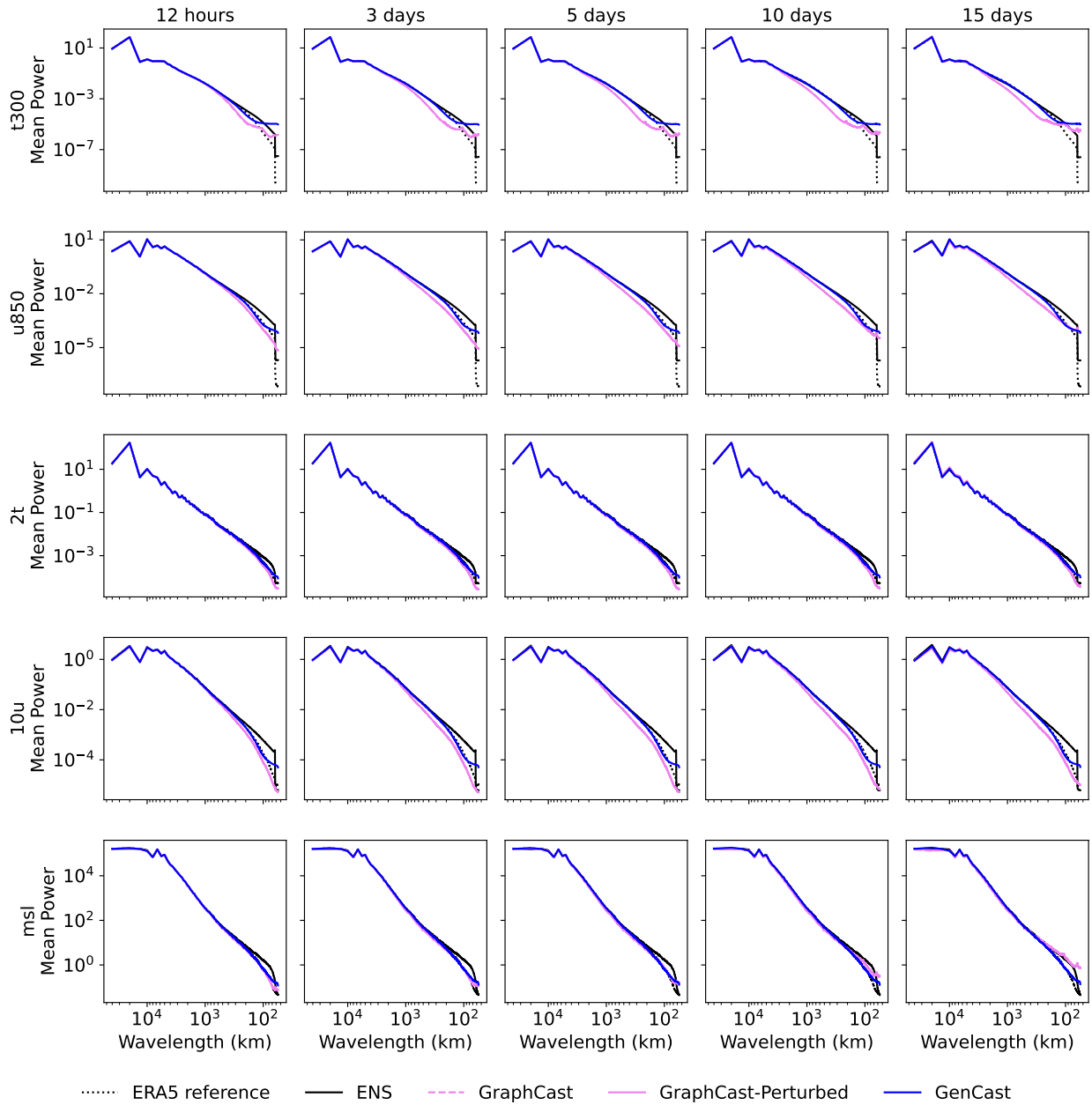


Figure F10 | Power spectrum plots for t300, u850, 2t, 10u and msl.

## F.6. GraphCast-Perturbed scorecards

Figure F11 shows RMSE and CRPS scorecards comparing GraphCast-Perturbed to ENS. We find that for long lead times, ENS is consistently better than GraphCast-Perturbed, sometimes by as much as 20%. Figure F12 shows RMSE and CRPS scorecards comparing GenCast to GraphCast-Perturbed. Except for RMSE at shorter lead times for a small number of variables, GenCast has better performance than GraphCast-Perturbed.

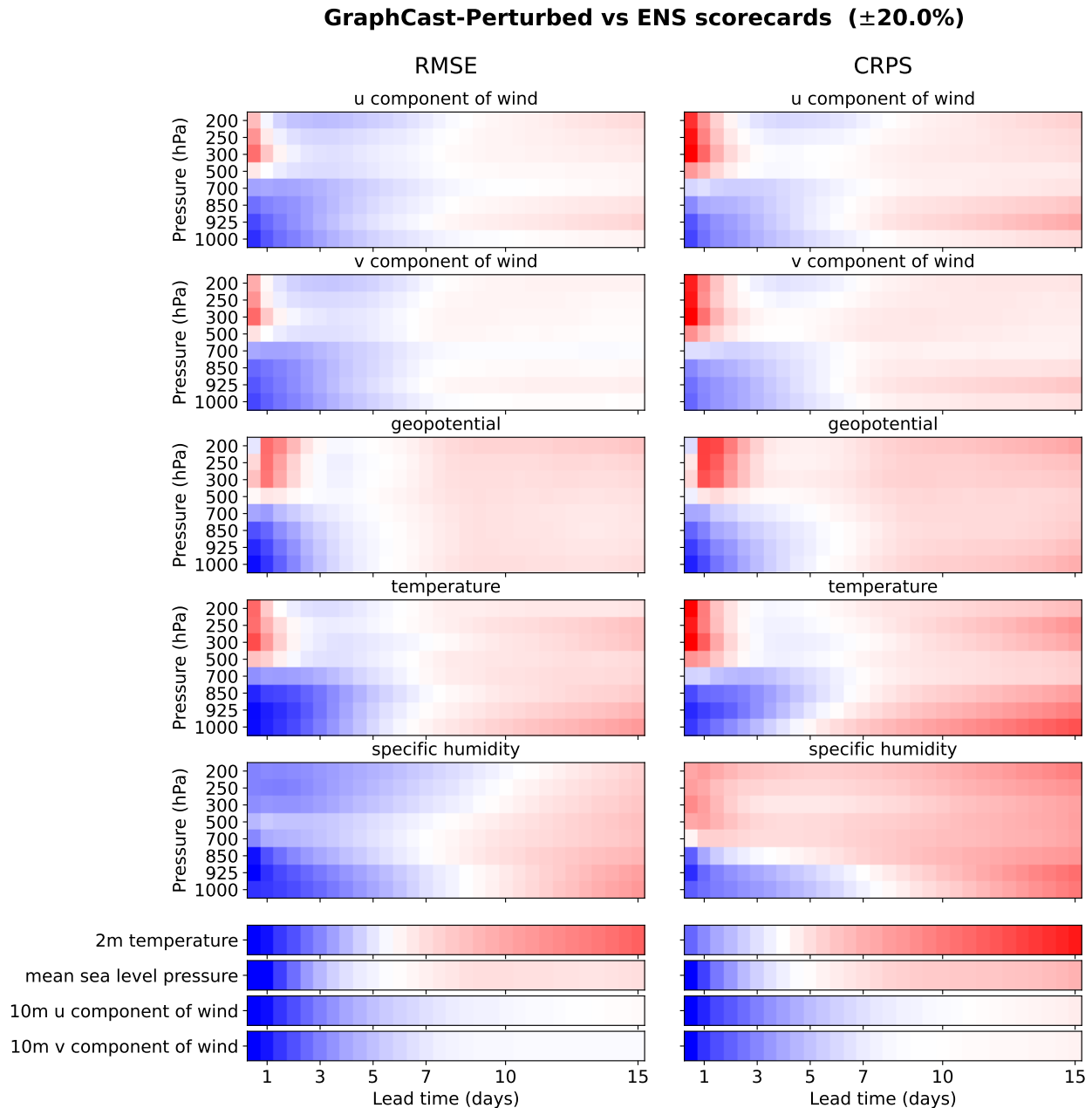


Figure F11 | RMSE and CRPS scorecard comparing GraphCast-Perturbed to ENS, dark blue (resp. red) means GraphCast-Perturbed is 20% better (resp. worse) than ENS, and white means they perform equally. Analogous to Figure 3 and F5.

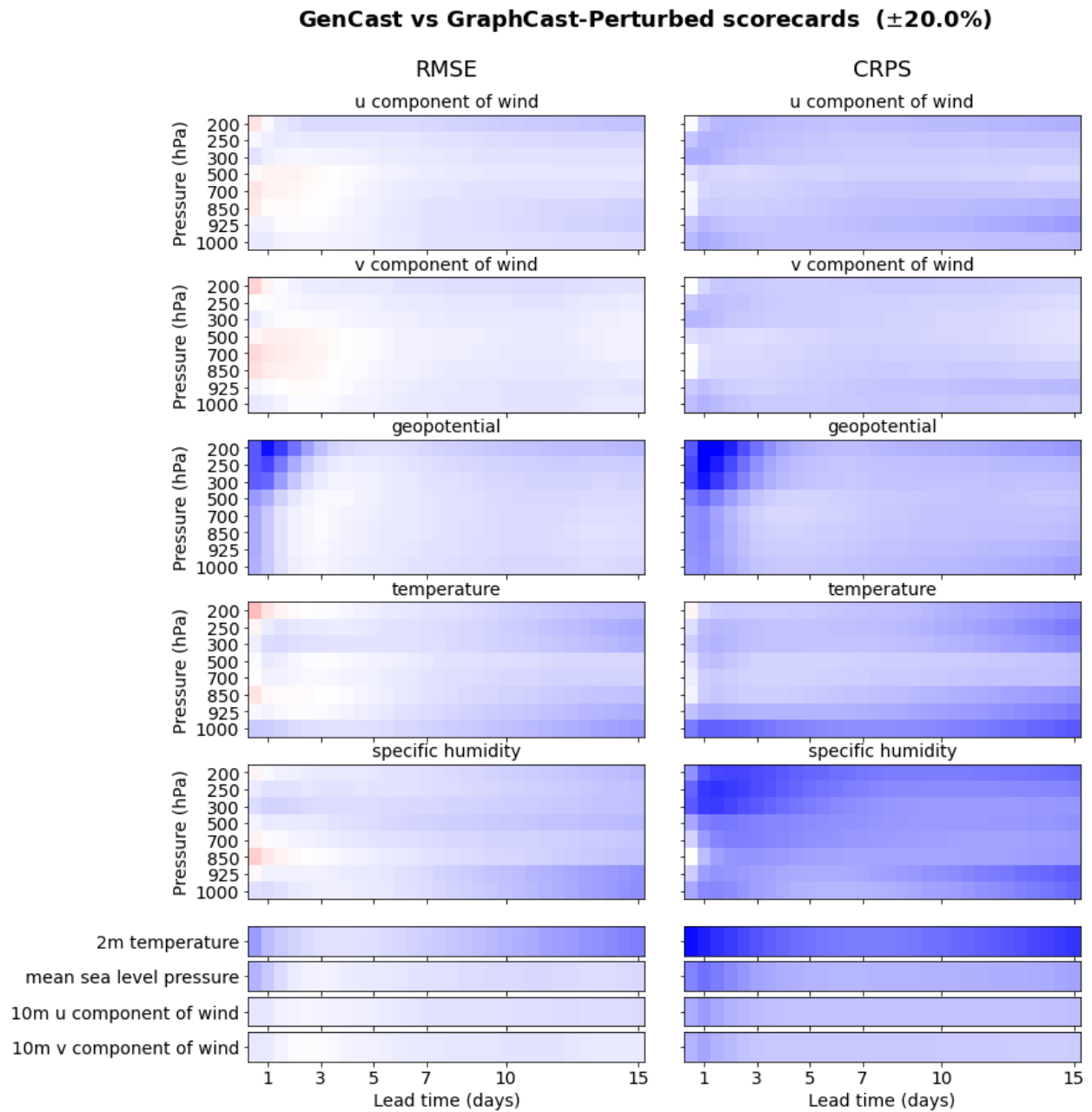


Figure F12 | RMSE and CRPS scorecard comparing GenCast to GraphCast-Perturbed. Analogous to Figure 3, F5 and F11.

### F.7. Extreme surface weather

We provide additional relative economic value plots, with statistical significance indicated, for various extreme thresholds, lead times and variables including extreme high temperature (Figure F13), extreme low temperature (Figure F14), extreme high wind speed (Figure F15), and extreme low mean sea level pressure (Figure F16). GenCast is significantly better than ENS ( $p < 0.05$ ) for up to 7 days lead time in many cases, and up to 15 days lead time in some others, while in some cases the differences are not statistically significant.

We also provide comparisons on Brier skill scores, with statistical significance indicated (Fig-

ure F17). GenCast shows significant ( $p < 0.05$ ) improvement over ENS for all thresholds, variables, and lead times shown, with the exception of certain lead times for  $<0.01$  and  $<0.1$  percentile mean sea level pressure where the improvement is not significant.

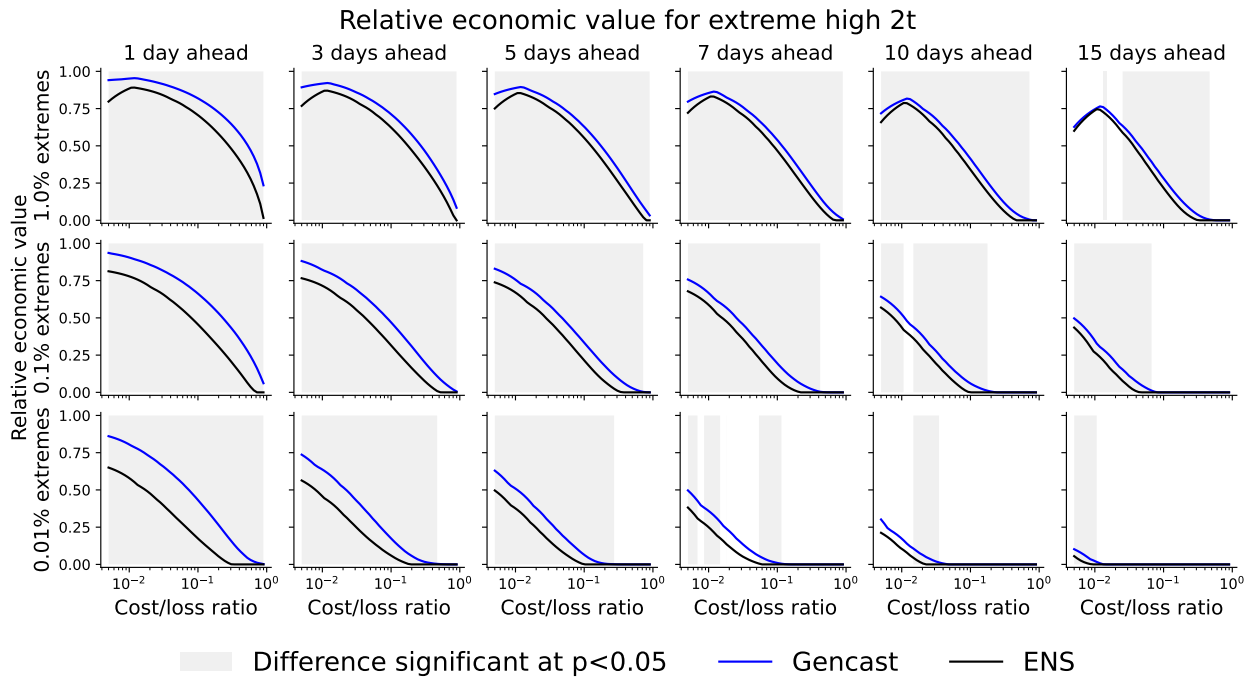


Figure F13 | Relative economic value plots for extreme high temperatures. Regions for which GenCast is better than ENS with statistical significance are shaded in grey.

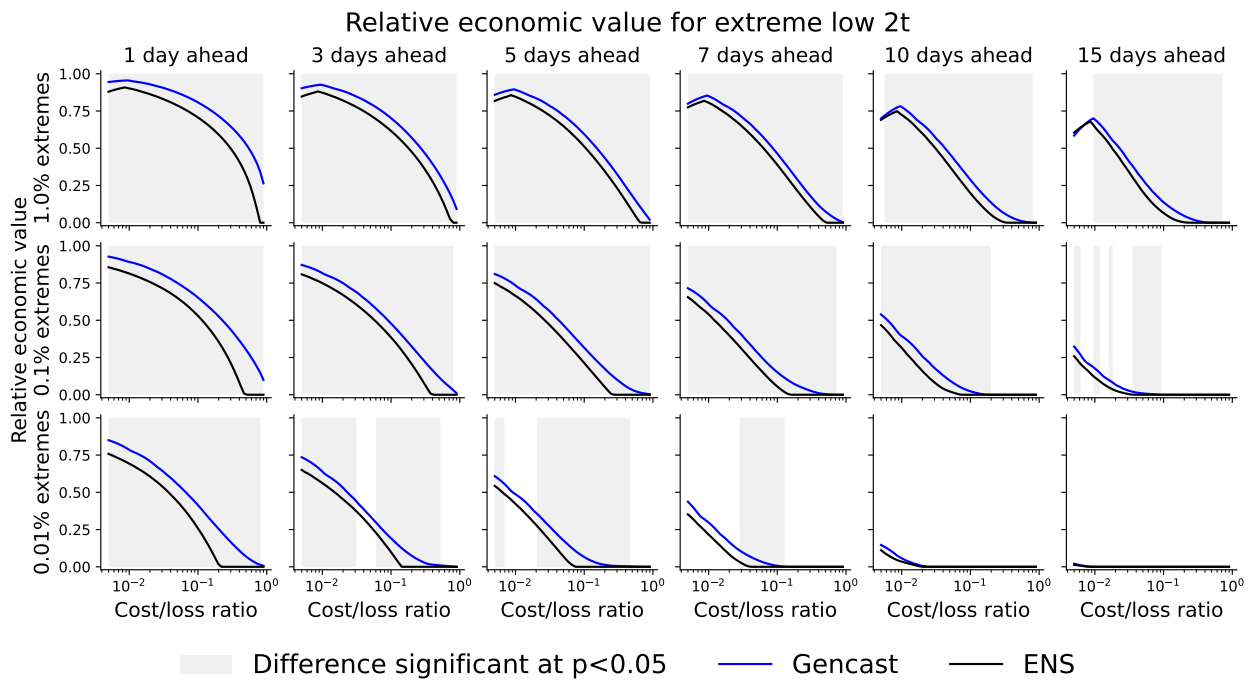


Figure F14 | Relative economic value plots for extreme low temperatures. Regions for which GenCast is better than ENS with statistical significance are shaded in grey.

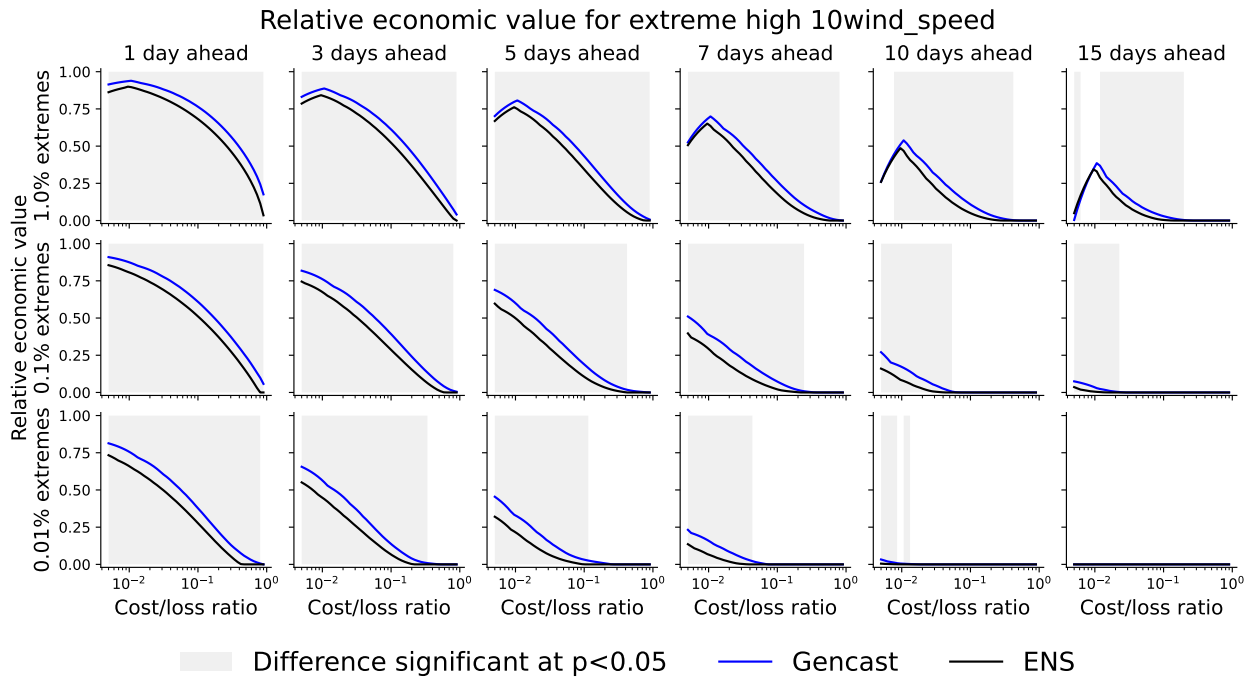


Figure F15 | Relative economic value plots for extreme high wind speeds. Regions for which GenCast is better than ENS with statistical significance are shaded in grey.

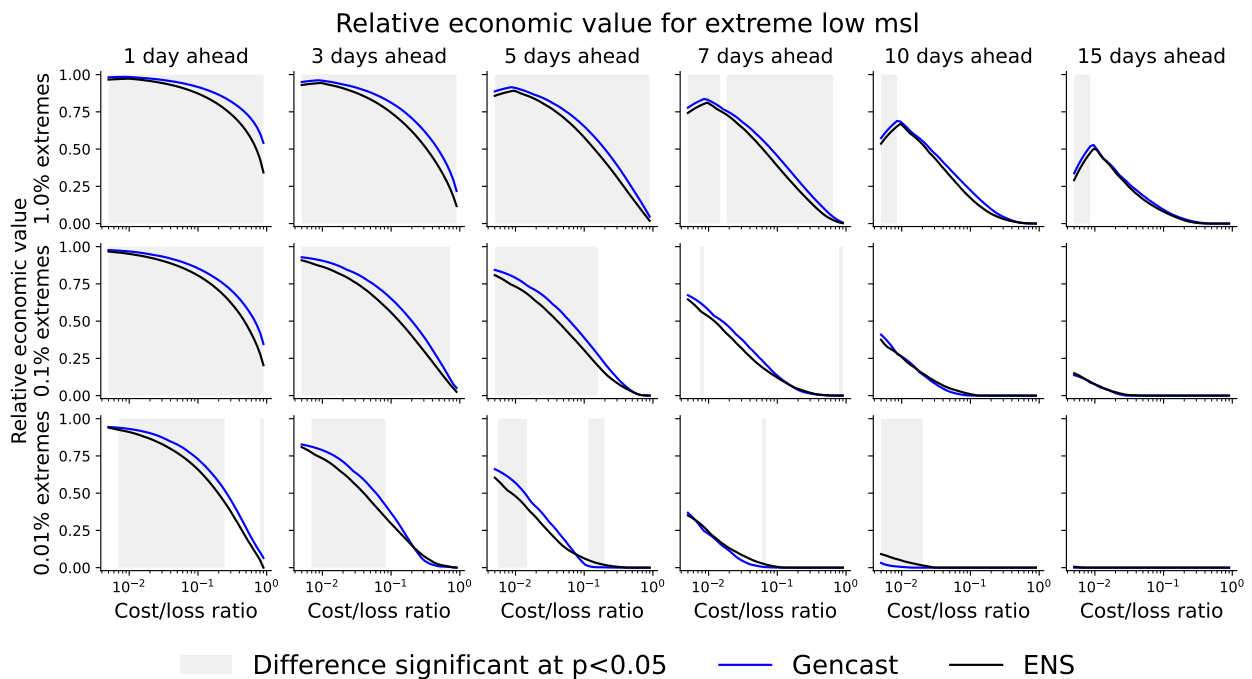


Figure F16 | Relative economic value plots for extreme low mean sea level pressure. Regions for which GenCast is better than ENS with statistical significance are shaded in grey.

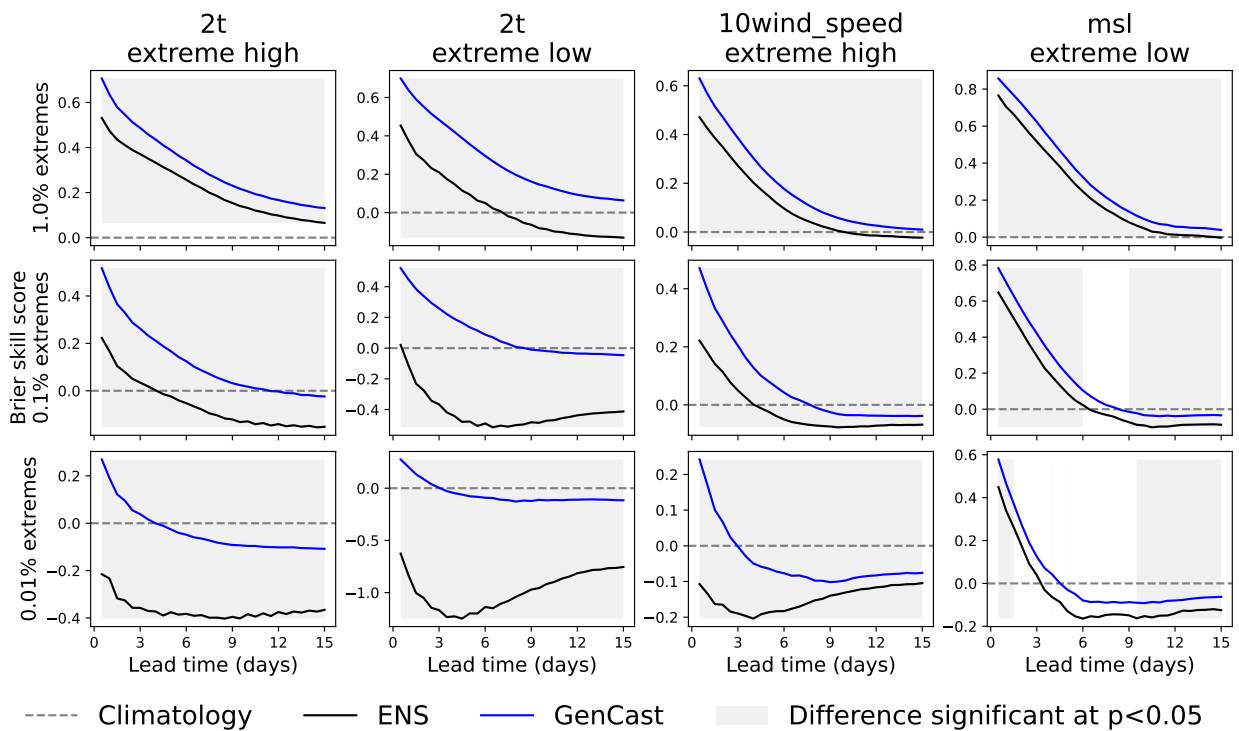


Figure F17 | Brier skill scores for ENS and GenCast for extreme high temperatures, extreme low temperatures, extreme high wind speed, and extreme low mean sea level pressure, with each row computing the metric for different percentile threshold. A skill score of one represents a perfect score, a skill score of 0 represents the skill of climatology, and below zero represents a skill worse than climatology. Regions for which GenCast is better than ENS with statistical significance are shaded in grey.

## F.8. Tropical cyclones

This section provides supplementary results for the tropical cyclone evaluation, including statistical significance. When tracks from GenCast and ENS are compared to cyclone tracks from their own ground truths (ERA5 and HRES-fc0, respectively), Figure F18 shows that GenCast significantly outperforms ENS across a broad range of cost-loss ratios at a lead time of 1 day, as well as at smaller cost-loss ratios at longer lead times up to 7 days.

For completeness, Figure F19 shows the REV obtained when both models are forced to use ENS's ground truth, HRES-fc0, giving an advantage to ENS. The gap between ENS and GenCast is smaller, particularly at a 1 day lead time, because the tracker encounters a distribution shift when stitching the HRES-fc0 context window to GenCast's predictions (Section E.5.2), which target ERA5. There is also a second distribution shift penalty because perfectly predicting ERA5 ground truth cyclone tracks would result in non-zero error when evaluated against HRES-fc0. Despite these two sources of penalty, GenCast significantly ( $p < 0.05$ ) outperforms ENS at small cost-ratios and lead times of 3–5 days. This shows that our results are robust to the difference in cyclone base rates between ERA5 and HRES-fc0.

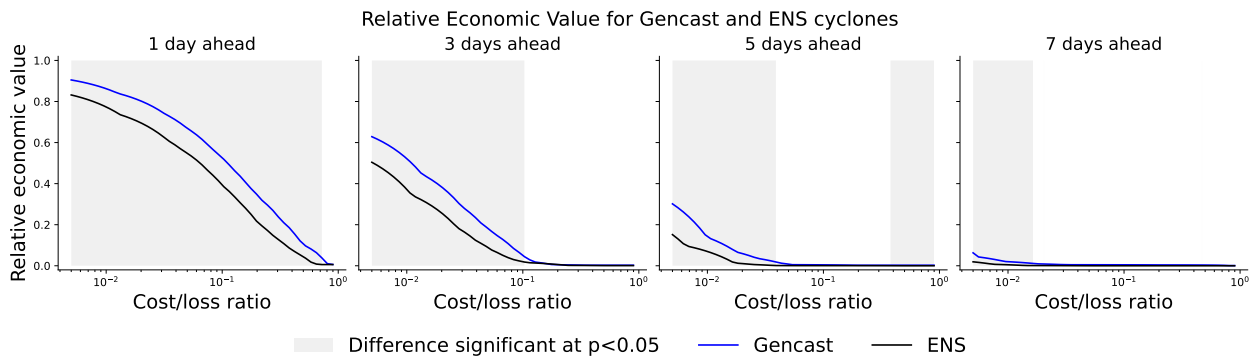


Figure F18 | Relative economic value for cyclone track prediction when comparing GenCast and ENS to ERA5 and HRES-fc0 targets, respectively. Statistical significance ( $p < 0.05$ ) of the improvement yielded by GenCast is indicated by light grey shading. The surprising statistical confidence at high cost/loss ratios at a 5 day lead time is due to GenCast having small but non-zero skill and ENS having exactly zero skill.

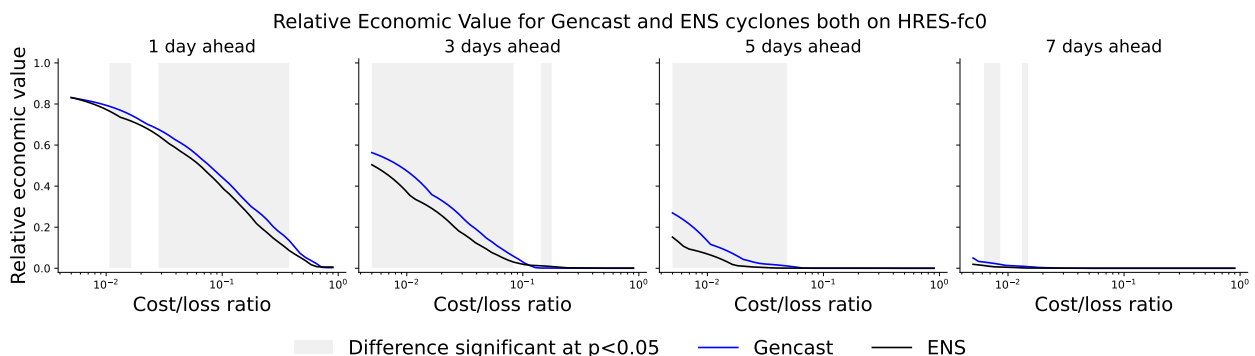


Figure F19 | Relative Economic Value for cyclone track prediction when comparing both GenCast and ENS to HRES-fc0 targets. Statistical significance ( $p < 0.05$ ) of the improvement yielded by GenCast is indicated by light grey shading. In general, GenCast is still statistically significantly better than ENS despite the disadvantage of comparing against a different ground truth.

## F.9. Joint distribution

### F.9.1. Wind speed as a derived variable

GraphCast and GraphCast-Perturbed can exhibit significant biases when used to forecast variables that are derived non-linearly from those the model was trained to predict. This is because GraphCast is trained using mean-squared-error to predict an expectation, and a non-linear function of an expectation is not equal to the expectation of the non-linear function. For example, GraphCast and GraphCast-Perturbed tend to predict wind speeds lower than average for long lead times, because GraphCast was trained to predict the expected wind vector  $(u, v)$  and not wind speed  $\sqrt{u^2 + v^2}$ . Uncertainty about wind direction thus results in an expected wind vector closer to the origin, and a lower wind speed.

To derive a skillful predictive distribution for wind speed from  $u$  and  $v$  requires modelling dependence between  $u$  and  $v$ , and so this task provides a simple test of GenCast’s ability to model cross-variable dependence structure. In Figure F20 we compare GenCast with GraphCast-Perturbed (and ENS) on both CRPS and forecast bias for 10u, 10v, and 10 m wind speed, where the wind speed variable is calculated as a function of the  $u$  and  $v$  forecasts. The most striking feature of GraphCast-Perturbed and GraphCast in Figure F20 is that while they exhibit minimal bias on 10u and 10v—indeed, less than ENS—they exhibit a significant negative bias in their derived wind speed forecasts, in particular at longer lead-times. GenCast, on the other hand, exhibits minimal bias on the derived 10 m wind speed, in addition to the very small bias it displays for 10u, 10v. Moreover, as shown in the top row of plots in Figure F20, while on CRPS the relative performance of GraphCast-Perturbed against ENS is worse for 10 m wind speed than for 10u and 10v, GenCast maintains the advantage it has over ENS for 10 m wind speed as well.

### F.9.2. Pooled evaluation

Figure F23 and Figure F24 show averaged-pooled and max-pooled CRPS scorecards for GenCast relative to ENS. Figure F25 and Figure F25 show averaged-pooled and max-pooled CRPS scorecards for GraphCast-Perturbed relative to ENS. We aggregate the  $u$ -component and  $v$ -component of wind into wind speed, and include tp12hr in our surface variables. This results in 5400 pooled verification targets across all variables, lead times, and spatial scales. Aggregating over all pooled verification targets, GenCast outperforms ENS’s average-pooled CRPS in 98.1% of cases (compared with 23.9% for GraphCast-Perturbed). For max-pooled CRPS, GenCast outperforms ENS in 97.6% of cases (compared with 7.0% for GraphCast-Perturbed, which performs especially badly on max-pooling due to blurring).

These results hold up in our surface-only  $0.25^\circ$  pooled evaluation, where GenCast substantially outperforms both ENS and GraphCast-Perturbed’s CRPS, often with relative performance improving as pooling size increases (Figure F21 and Figure F22).

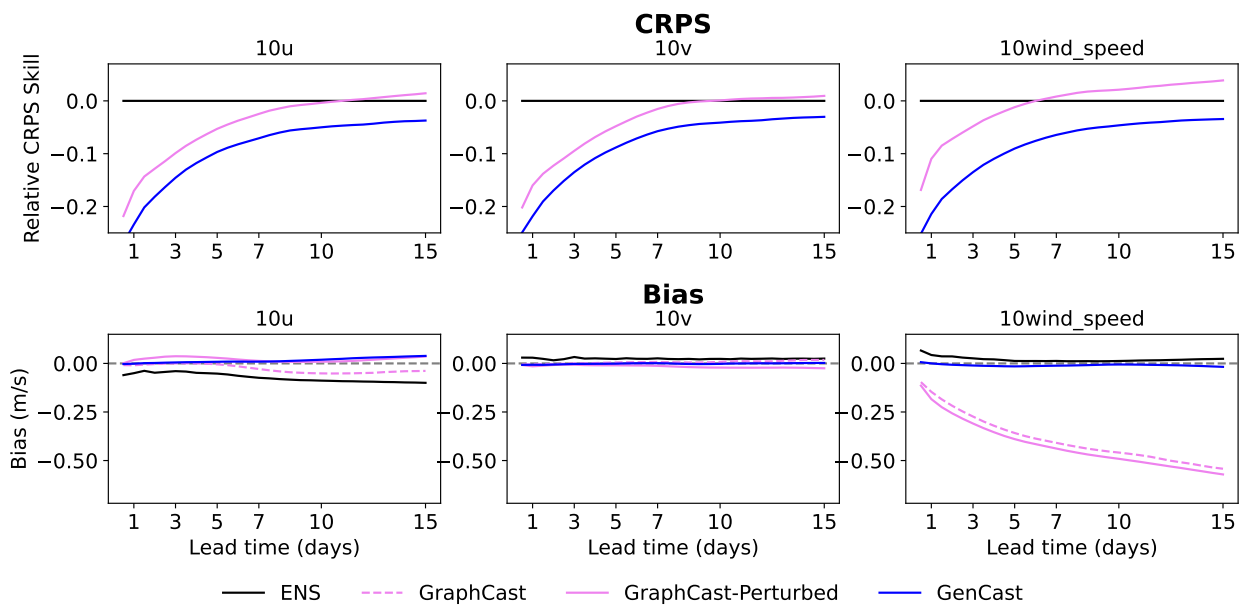


Figure F20 | Comparison of the relative CRPS (lower is better) and bias (close to zero is better) performance on native surface wind components 10u and 10v, and derived wind speed. We observed how the performance of GraphCast-Perturbed is relatively stronger on the variables that it was trained to predict (wind components), than it is on the derived variable (wind speed), exhibiting poorer relative CRPS and a strong negative bias for wind speed. Similarly, GraphCast exhibits minimal bias for 10u and 10v wind components, but a large negative bias on wind speed. On the other hand GenCast performs similarly well on both the wind components (which it was trained to predict), and the wind speed (which is derived). This seems to support the hypothesis that the states produced by GenCast are more physically plausible than GraphCast and GraphCast-Perturbed, as are the states produced by ENS.

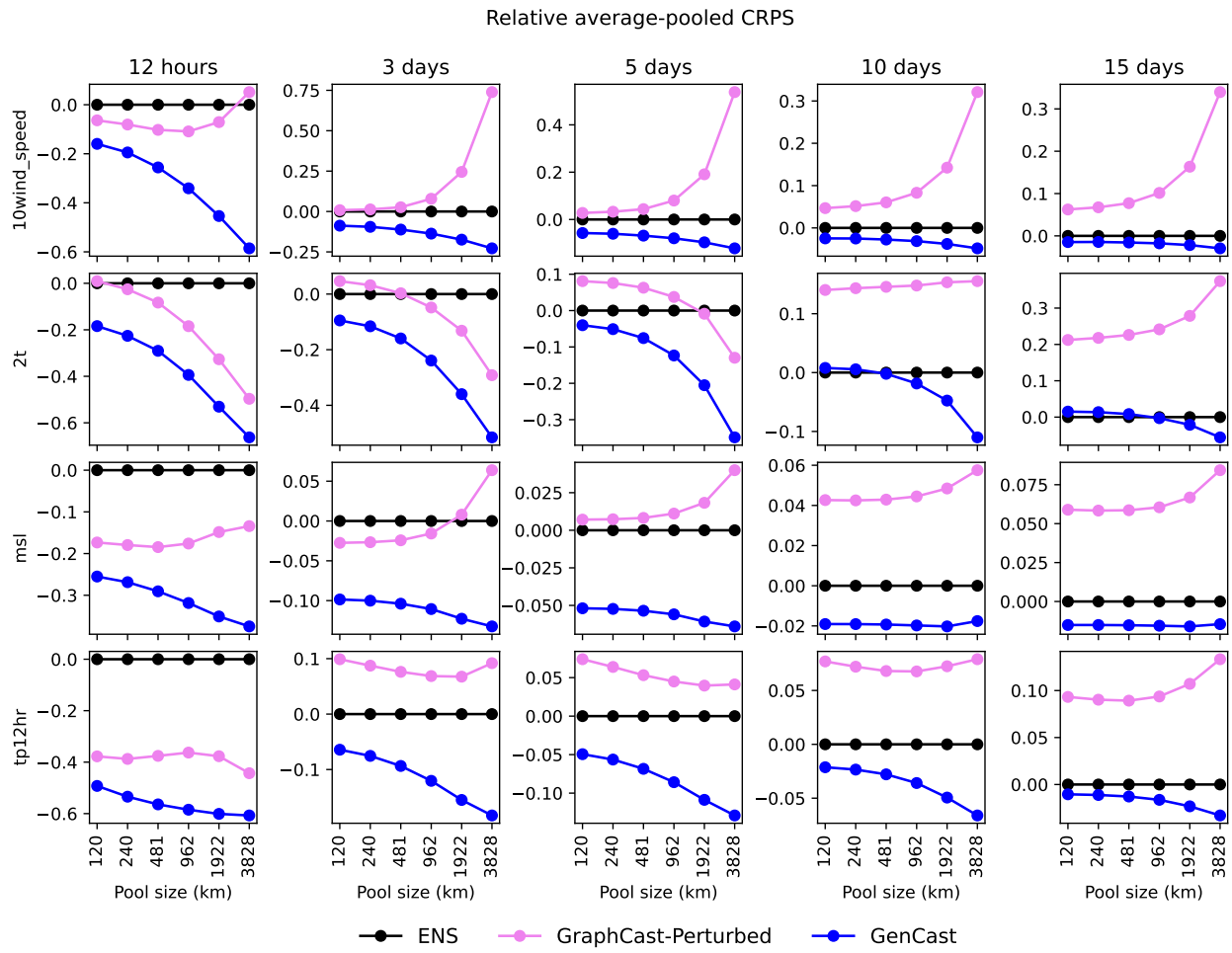


Figure F21 | 2019 average-pooled CRPS skill score plots for 0.25 deg surface variables. The sizes of the pooling regions can be visualized in Figure E2.

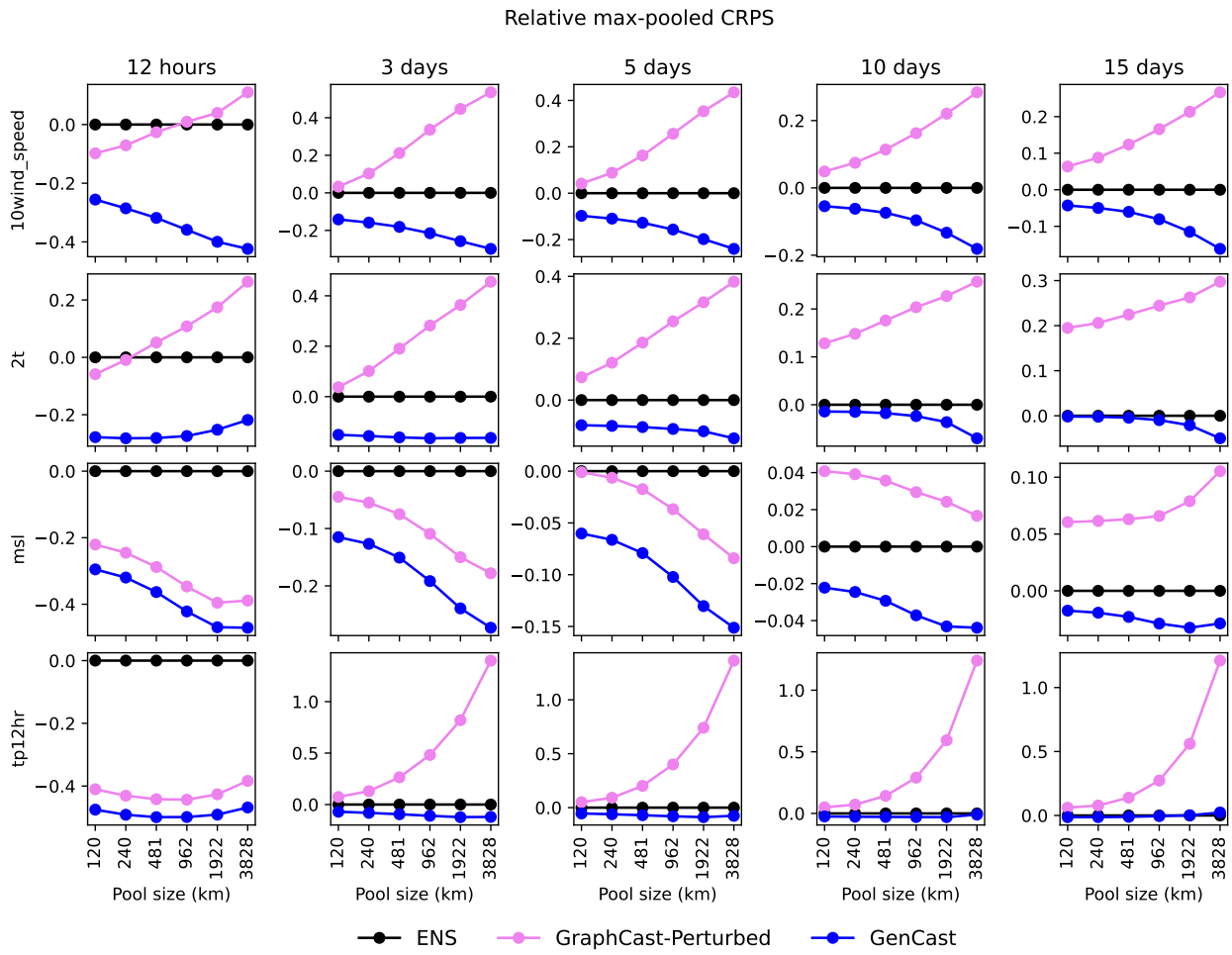


Figure F22 | 2019 max-pooled CRPS skill score plots for 0.25 deg surface variables. The sizes of the pooling regions can be visualized in Figure E2.

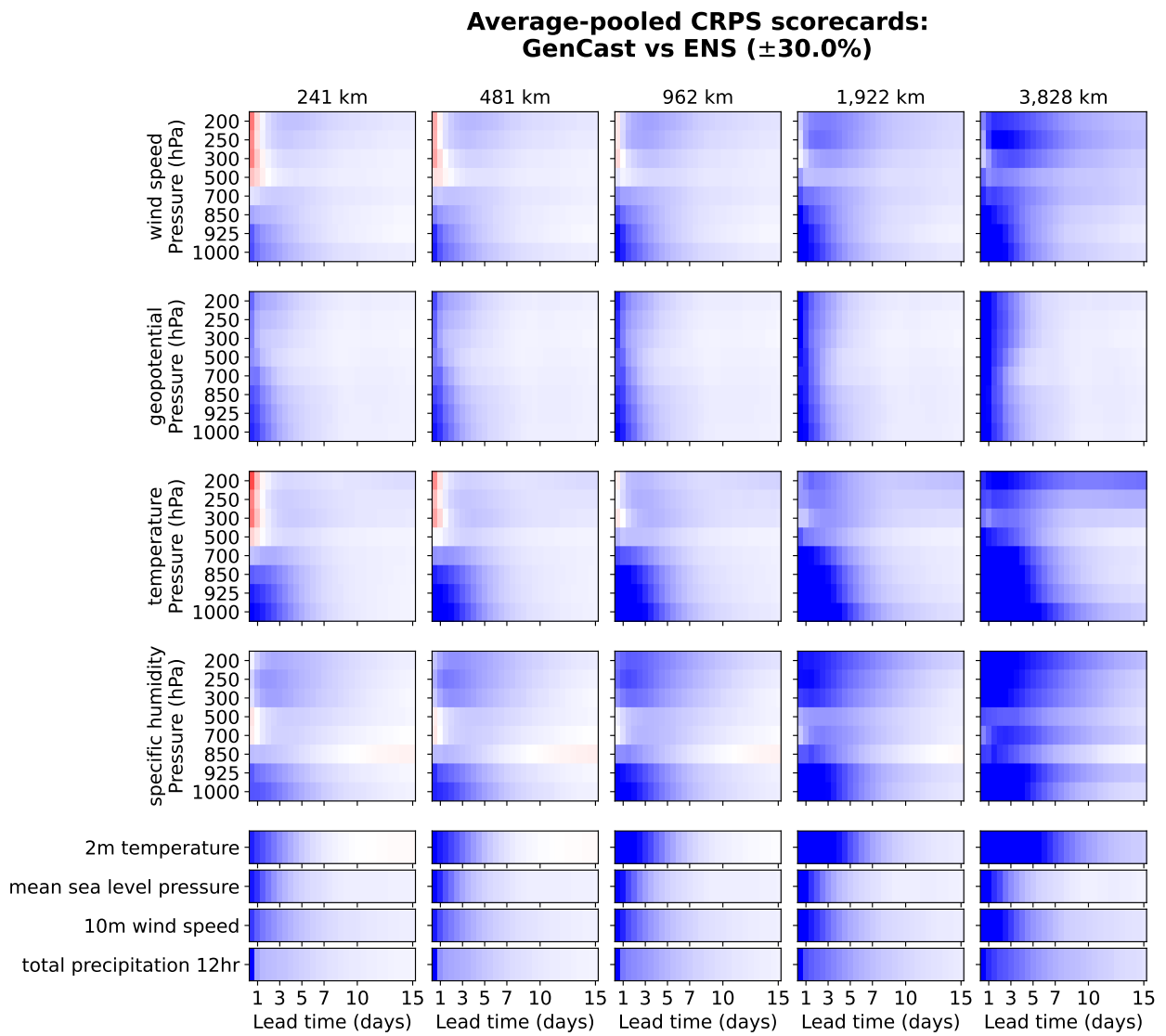


Figure F23 | Average-pooled CRPS scorecard comparing GenCast and ENS at varying spatial scales, dark blue (resp. red) means GenCast is 30% better (resp. worse) than ENS, and white means they perform equally.

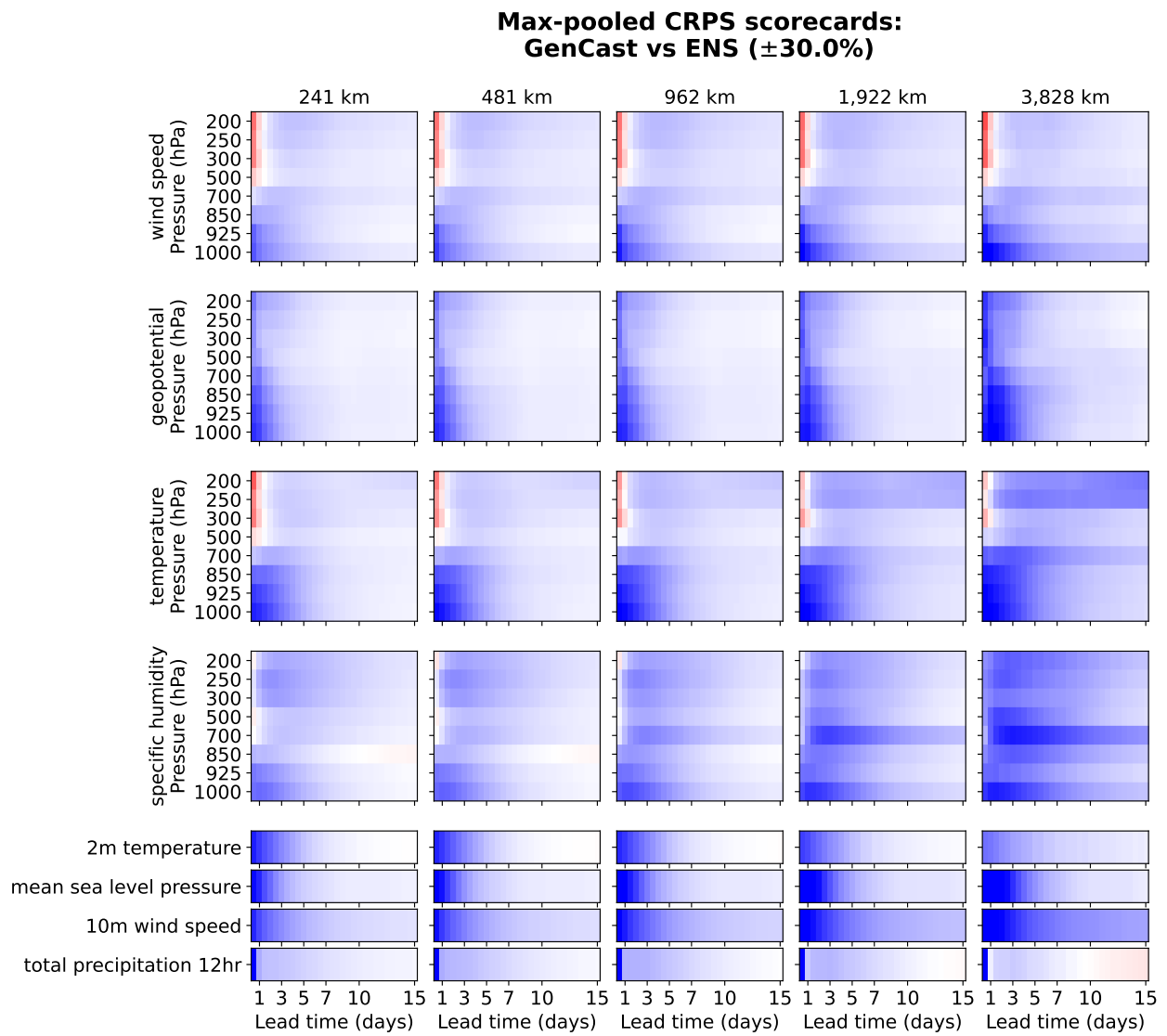


Figure F24 | Max-pooled CRPS scorecard comparing GenCast and ENS at varying spatial scales, dark blue (resp. red) means GenCast is 30% better (resp. worse) than ENS, and white means they perform equally.

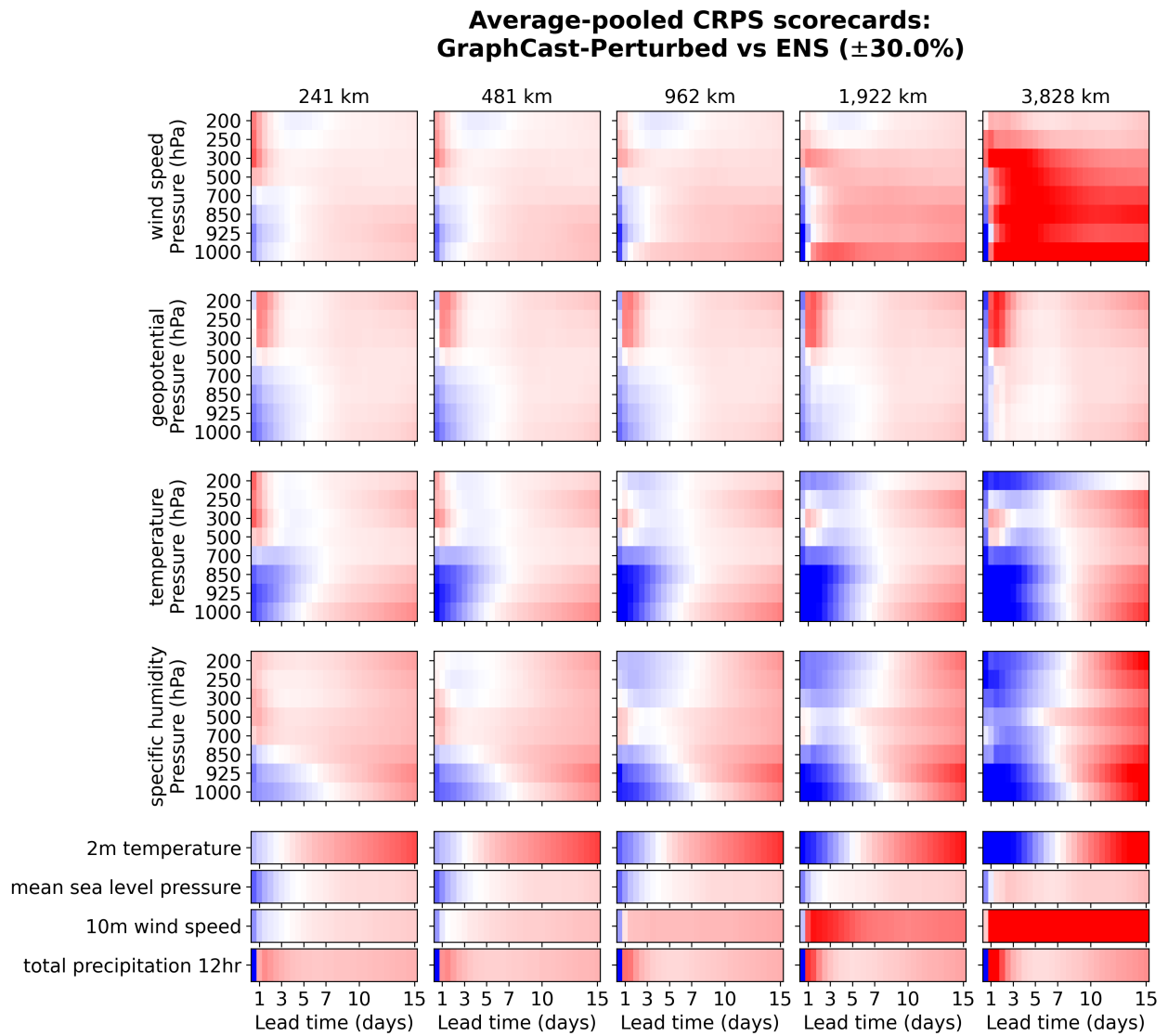


Figure F25 | Average-pooled CRPS scorecard comparing GraphCast-Perturbed and ENS at varying spatial scales, dark blue (resp. red) means GraphCast-Perturbed is 30% better (resp. worse) than ENS, and white means they perform equally.

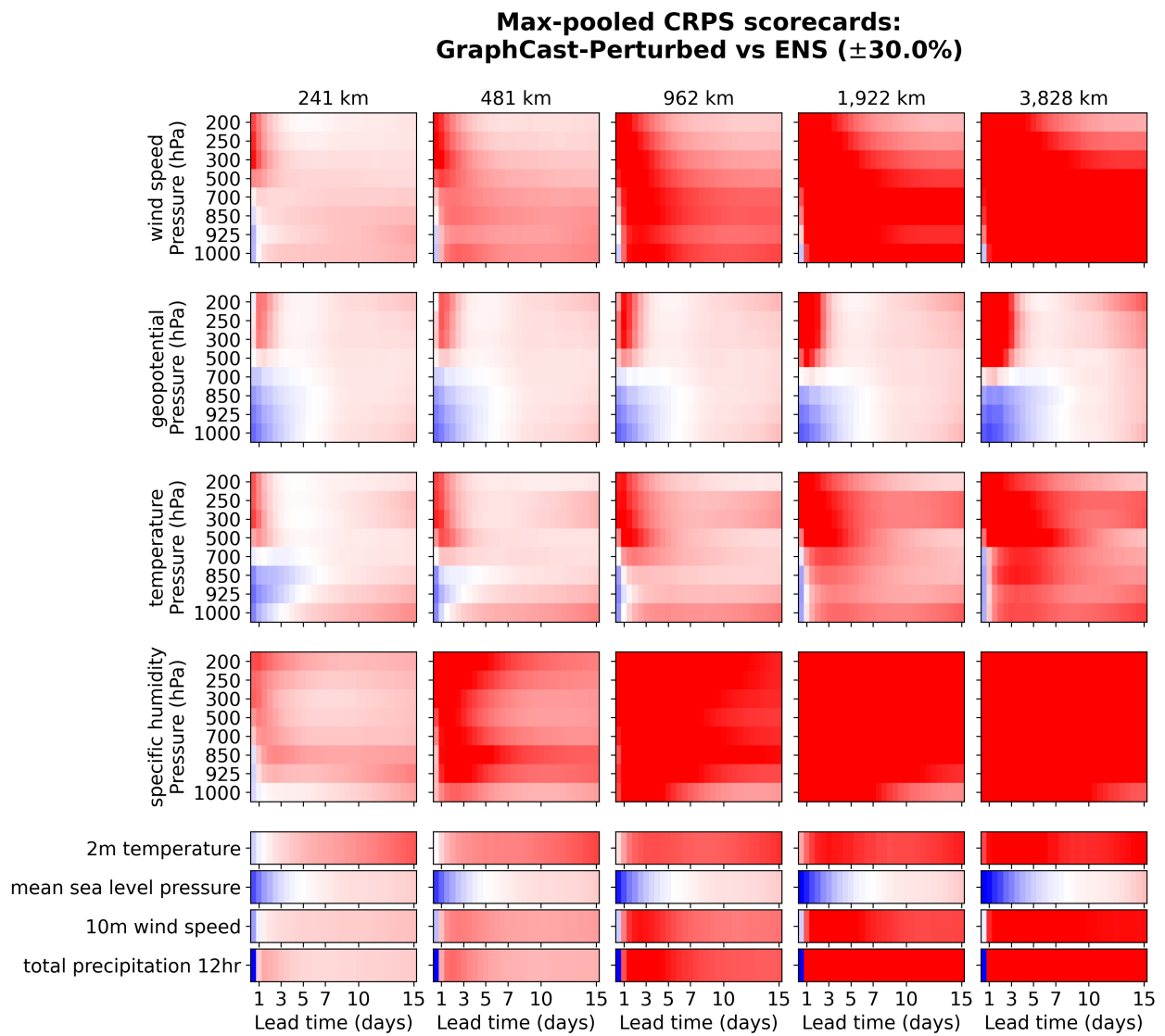


Figure F26 | Max-pooled CRPS scorecard comparing GraphCast-Perturbed and ENS at varying spatial scales, dark blue (resp. red) means GraphCast-Perturbed is 30% better (resp. worse) than ENS, and white means they perform equally.

### F.10. Regional wind power forecasting statistical significance

Figure F27 shows the relative CRPS of GenCast and ENS on the regional wind power forecasting task of Section 8.2. Lead times at which the difference in CRPS is statistically significant ( $p < 0.05$ ) are shaded grey. Differences are significant up to a 7 day lead time for all pool sizes, and up to 10 days with a few exceptions.

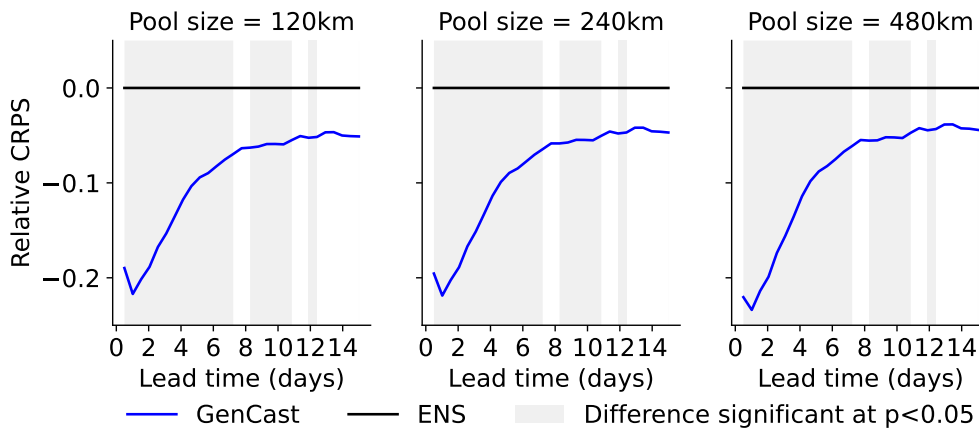


Figure F27 | Regional wind power results. Grey shading indicates the lead times at which the improvement achieved by GenCast is statistically significant ( $p < 0.05$ ).

### F.11. Ablation of EDA perturbations in GenCast initial conditions

Here we ablate the use of perturbed initial conditions when generating ensemble forecasts with GenCast. Figure F28 (colour range only  $\pm 2\%$ ) shows that on CRPS and RMSE, EDA perturbations have very little effect, and Figure F29 confirms that GenCast still outperforms ENS on RMSE and CRPS in the same percentage of cases even when initialising all ensemble members from deterministic ERA5 analysis. Figure F30 plots the spread skill ratios across lead times for a subset of variables and pressure levels, showing that the primary impact of the perturbed initial conditions is on the dispersion of the ensemble. Initialising with deterministic analysis alone generally improves the spread-skill ratio achieved on the first step or two. However we expect this is an artifact of evaluating against deterministic analysis, which will artificially reward under dispersion at short lead times, rather than being a meaningful improvement. In addition, the ensemble-initialised GenCast has generally better spread skill from approximately 2-3 days lead time onward.

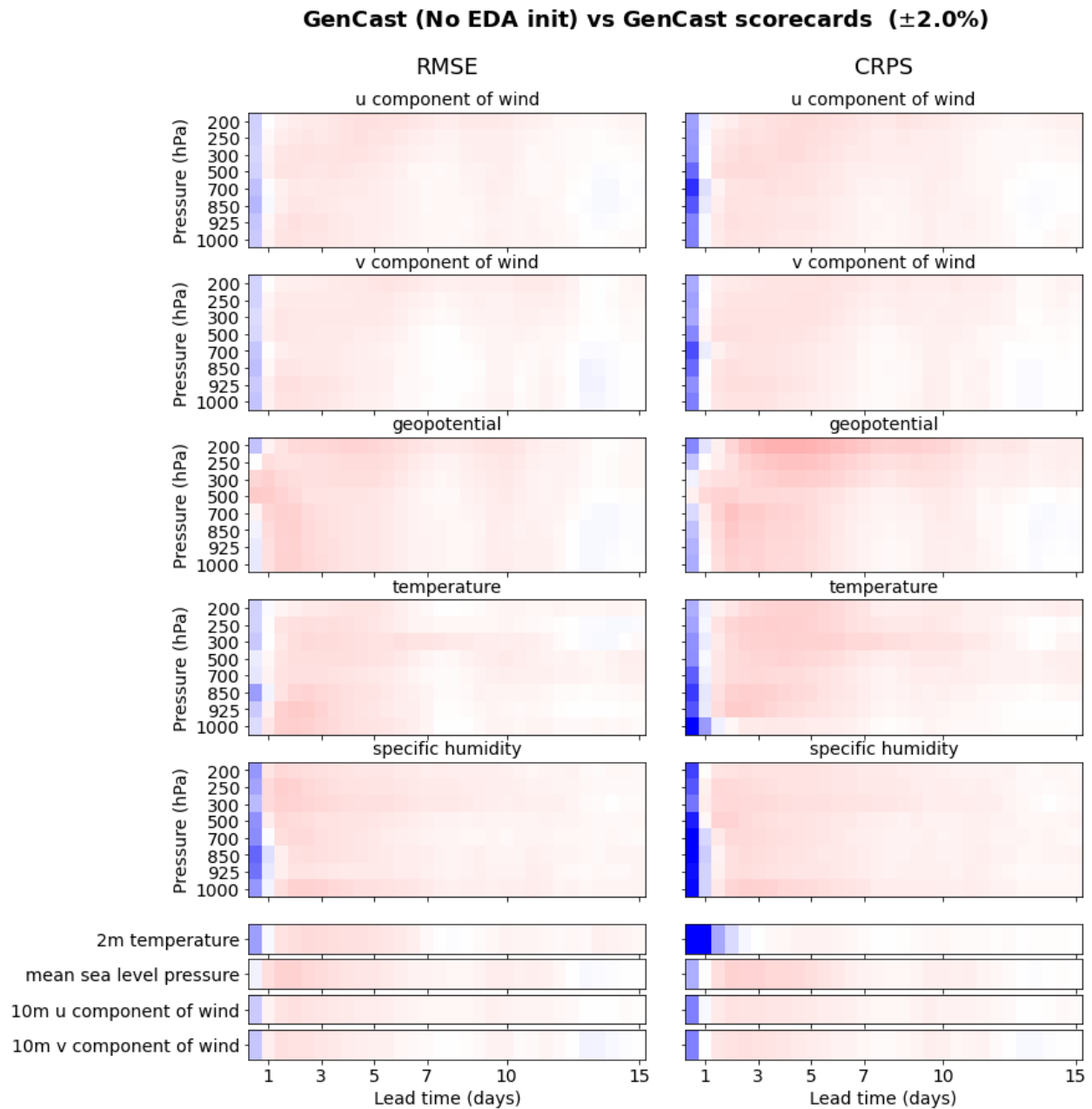


Figure F28 | CRPS and RMSE scorecards comparing GenCast using deterministic ERA5 analysis as initial conditions to GenCast as presented in the main results section, using perturbed initial conditions. Performance with and without EDA-perturbed initial conditions is extremely similar, and in this scorecard maximum saturation of blue and red correspond to only a 2% relative improvement or degradation respectively. Blue indicates GenCast initialised with deterministic ERA5 analysis is performing marginally better, Red indicates GenCast with EDA-perturbed initial conditions is performing marginally better.

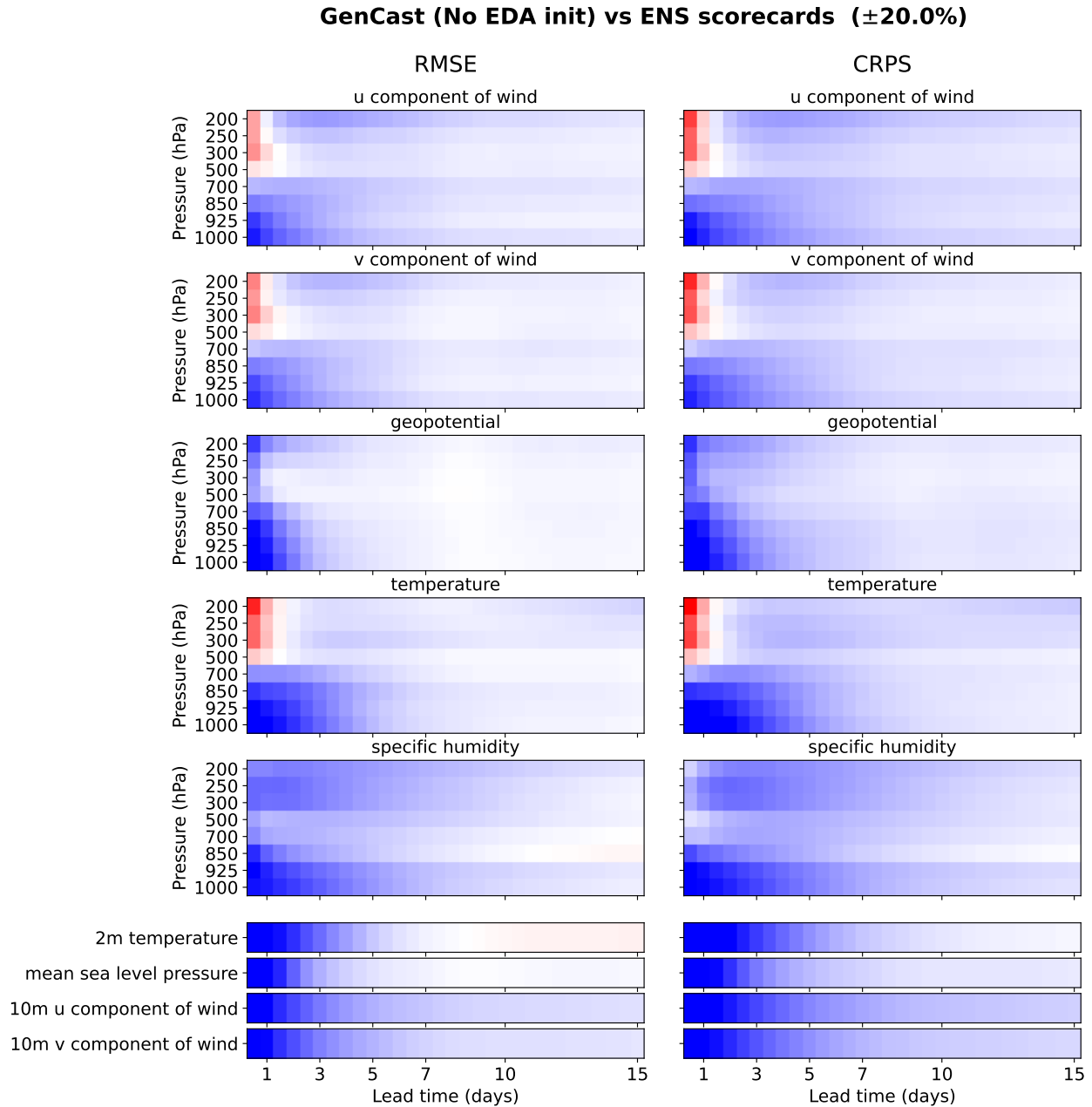


Figure F29 | CRPS and RMSE scorecards comparing GenCast using deterministic ERA5 analysis as initial conditions to ENS. GenCast still outperforms ENS on 96% and 97% of ensemble-mean RMSE and CRPS targets respectively.

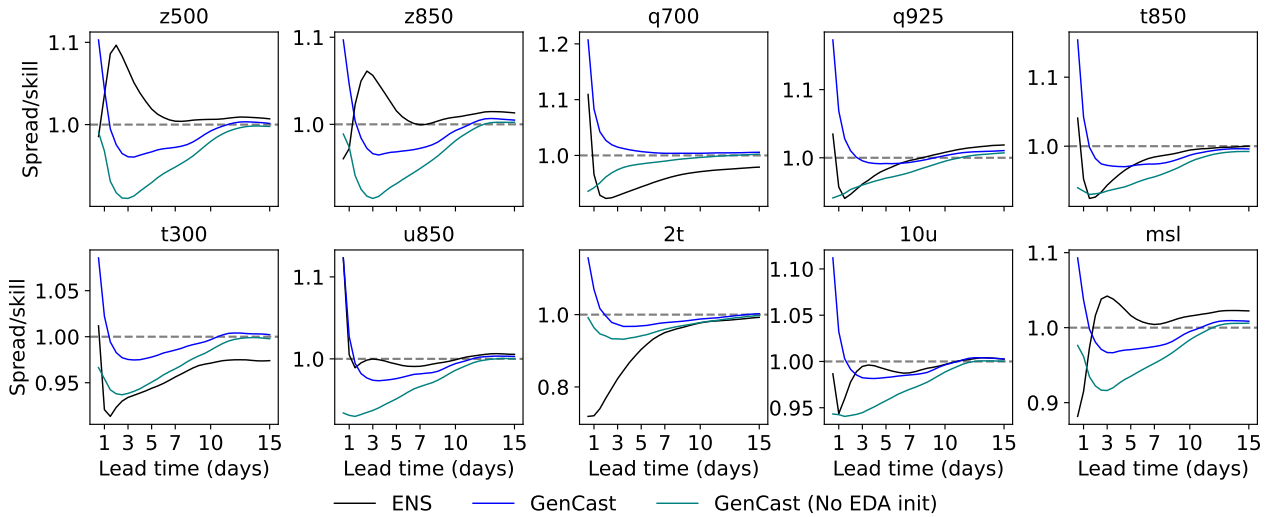


Figure F30 | Spread-skill ratios of ENS, GenCast, and GenCast but without EDA-perturbed initial conditions. Initial spread-skill is closer to 1 for the first forecast step, but overall GenCast without EDA-perturbed initial conditions is somewhat under-dispersed. compared to the default GenCast.

## F.12. Empirical support of initialisation time and evaluation time choices for verification

### F.12.1. Initialisations used for GenCast evaluation

Our main results always use 06/18 UTC initialisation times when evaluating GenCast. Figure F31 shows a scorecard comparing GenCast initialised at 00/12 and 06/18 UTC, showing how the 00/12-initialised forecasts have a systematic advantage due to the ERA5 look-ahead at those initialisation times. This motivates the use of 06/18 UTC initialisations for the evaluations of GenCast as the most conservative approach.

### F.12.2. Lead time interpolation in regional wind farm evaluation

Section E.1 motivates and describes the lead time interpolation method for evaluating ENS and GenCast on the same set of validity times for regional wind power forecasting. We were able to download 06/18 UTC initialised ENS forecasts for some surface variables for 2018 to validate and justify this approach. Figure F32 shows that on the regional wind power forecasting task, lead time interpolation with 00/12-initialised ENS forecasts actually overestimates the performance of 06/18-initialised ENS forecasts on 06/18 UTC targets. This is particularly the case at a 12-hour lead time, where 06/18-initialised ENS performs 6% worse than 00/12-initialised ENS with lead time interpolation. This suggests that the lead time interpolation is in fact advantaging ENS in Section 8.2, and explains the non-monotonicity in GenCast’s relative performance at the shortest lead times in Figure 4d.

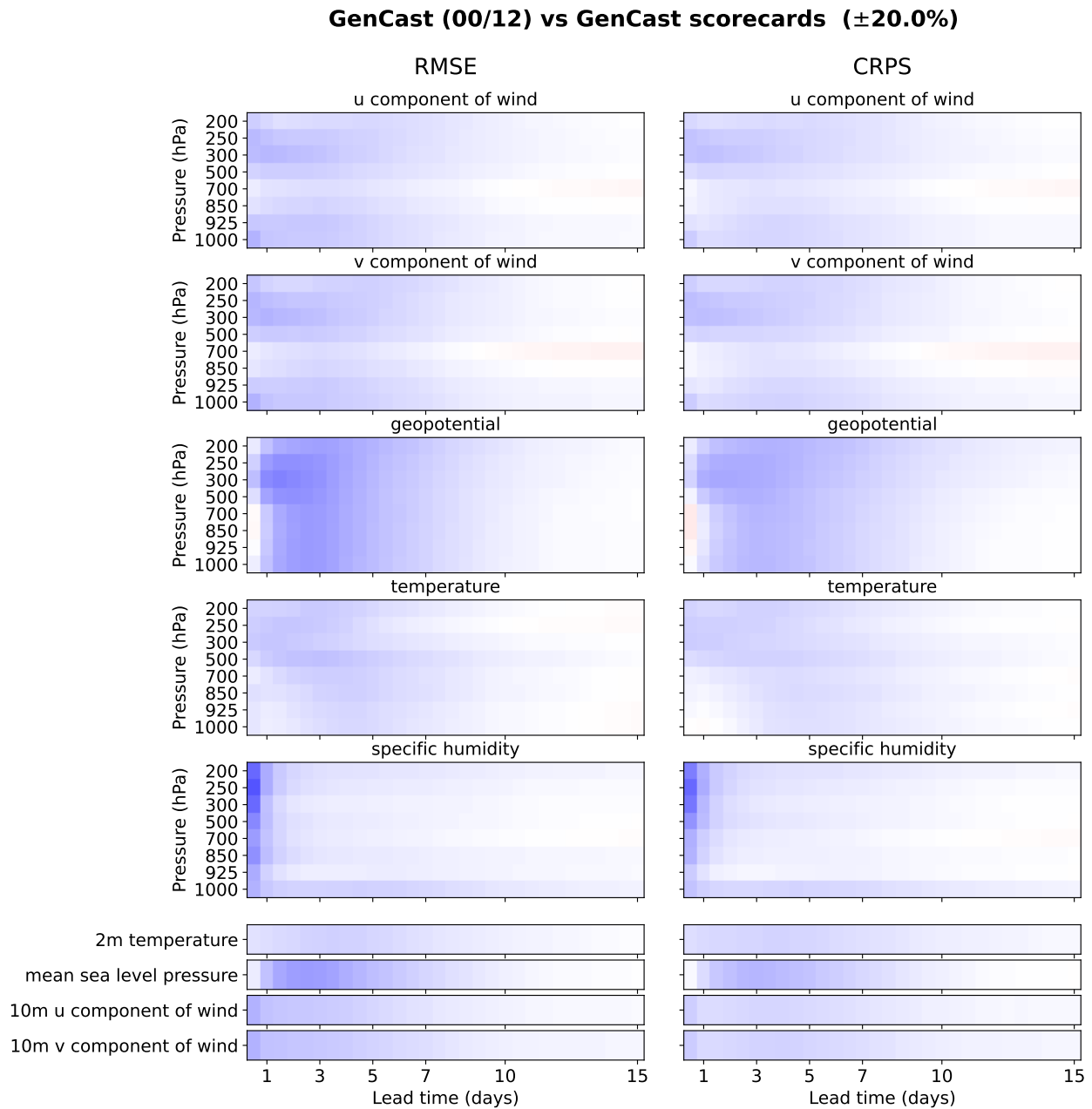


Figure F31 | Scorecard comparing the performance of GenCast evaluated on 00/12 UTC initialisation times, to GenCast evaluated on the 06/18 UTC initialisation times (the latter is used in the rest of the evaluation in the paper). The 9 hour assimilation look-ahead of the 00/12 UTC initialisations gives the model a consistent advantage in CRPS and Ensemble-Mean RMSE over the 3 hour assimilation look-ahead of the 06/18 UTC initialisations. This highlights the importance of accounting for assimilation window look-ahead when comparing metrics across model evaluations.

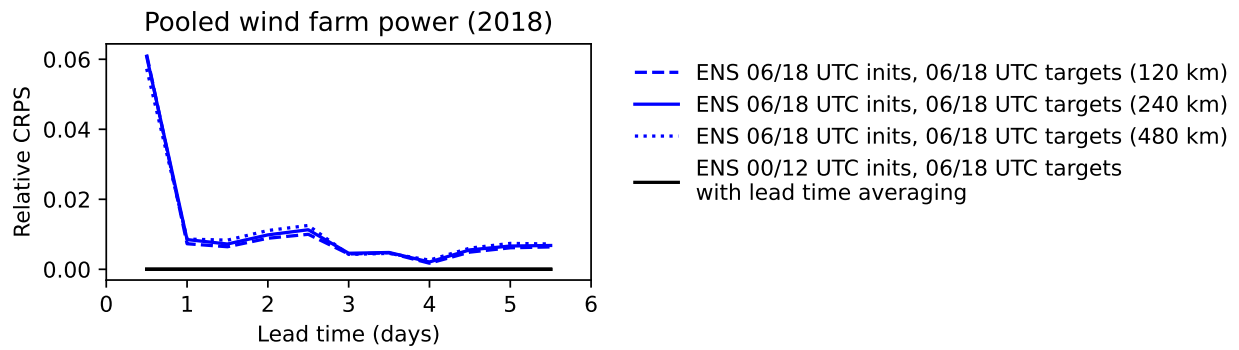


Figure F32 | Relative CRPS of ENS (06/18 UTC initialisations) compared to ENS 00/12 UTC initialisations with the lead time averaging applied to 06/18 UTC targets, on the regional wind power forecasting task.

## G. Forecast visualisations

### G.1. Tropical cyclone tracks

Here we provide further cyclone track visualisations. We picked some of the most extreme cyclones in 2019, based on several measures: the deadliest, the costliest, the strongest globally, and the strongest in the Atlantic basin. The deadliest cyclone was Cyclone Idai, which killed over 1500 people and caused a humanitarian crisis in Mozambique, Zimbabwe, and Malawi (Figure G1). The costliest cyclone was Typhoon Hagibis, which struck Japan and caused damages of 17.3 billion USD in 2019 (Figure G2). The strongest cyclone was Typhoon Halong, with a minimum barometric pressure of 905 hPa and maximum 1-minute sustained winds of 305 km/h (85 m/s) (Figure G3). The strongest cyclone in the Atlantic basin was Hurricane Dorian, which caused catastrophic damage in the Bahamas as a Category-5 hurricane before moving northwards along the coast of the United States, where it caused further damage and power outages (Figure G4).

In our visualisations, we set the validity dates as the day of landfall for Idai and Hagibis. For Halong, which did not make landfall, we set the validity date as the day the cyclone reached Category-5 status. For Dorian, we picked a time when the cyclone had weakened to Category-2 status, to also capture its effects on the East coast of the US.

Due to the 6-hour offset in initialisation and validity times between GenCast and ENS in our cyclone analysis (06/18 UTC and 00/12 UTC, respectively), in our visualisations we show ENS forecasts initialised both 6 hours before and 6 hours after GenCast's (with the same lead time). A 12-hour later initialisation time can give a model information on a cyclone that is 12 hours further into its development, which can have a material effect on cyclone forecasts in some cases. For example, when initialised 12 hours later, ENS performs substantially better at predicting Hurricane Dorian's curve northward along the eastern coast of the United States after passing the Bahamas (Figure G4a vs Figure G4k).

These visualisations are for illustration purposes only and have not been chosen as representative of differences between GenCast and ENS. We refer the reader to our systematic REV evaluation for a rigorous and principled comparison of model performance (Figure 4b, Figure F18, Section E.5.1). We note that in some cases the trajectory of the main cyclone being visualised coincides with the trajectory of another cyclone nearby (e.g. Figure G2a, Figure G4a). Finally, whereas tracks with short lead times branch out from an initial point, some tracks for long lead times *start* from different places (e.g. Figure G3a,f,k). This is because the forecasts are initialised before the cyclone started and the model is uncertain about whether cyclogenesis will occur and, if so, where it will occur.

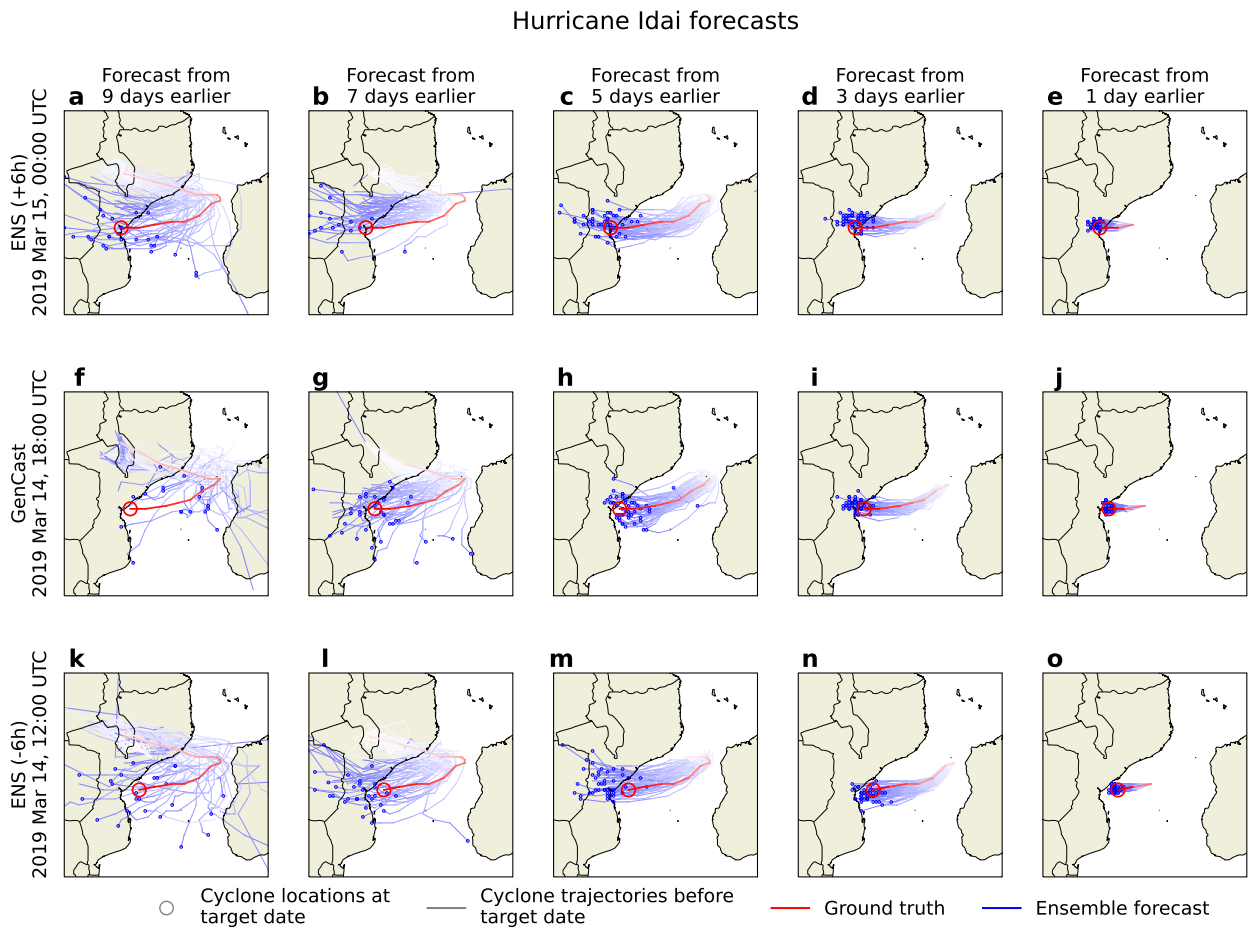


Figure G1 | Visualisation of Cyclone Idai trajectory forecasts.

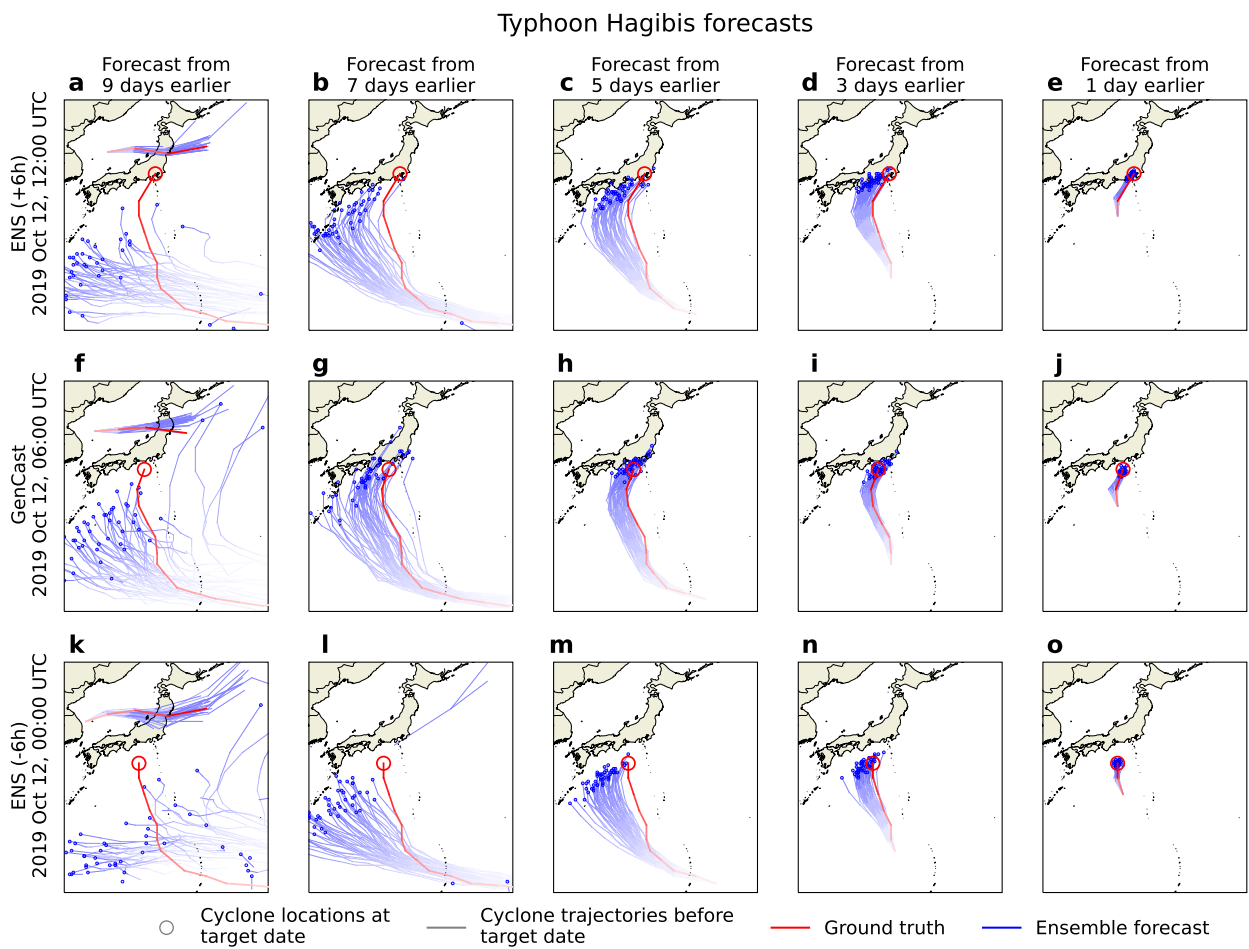


Figure G2 | Visualisation of Typhoon Hagibis trajectory forecasts.

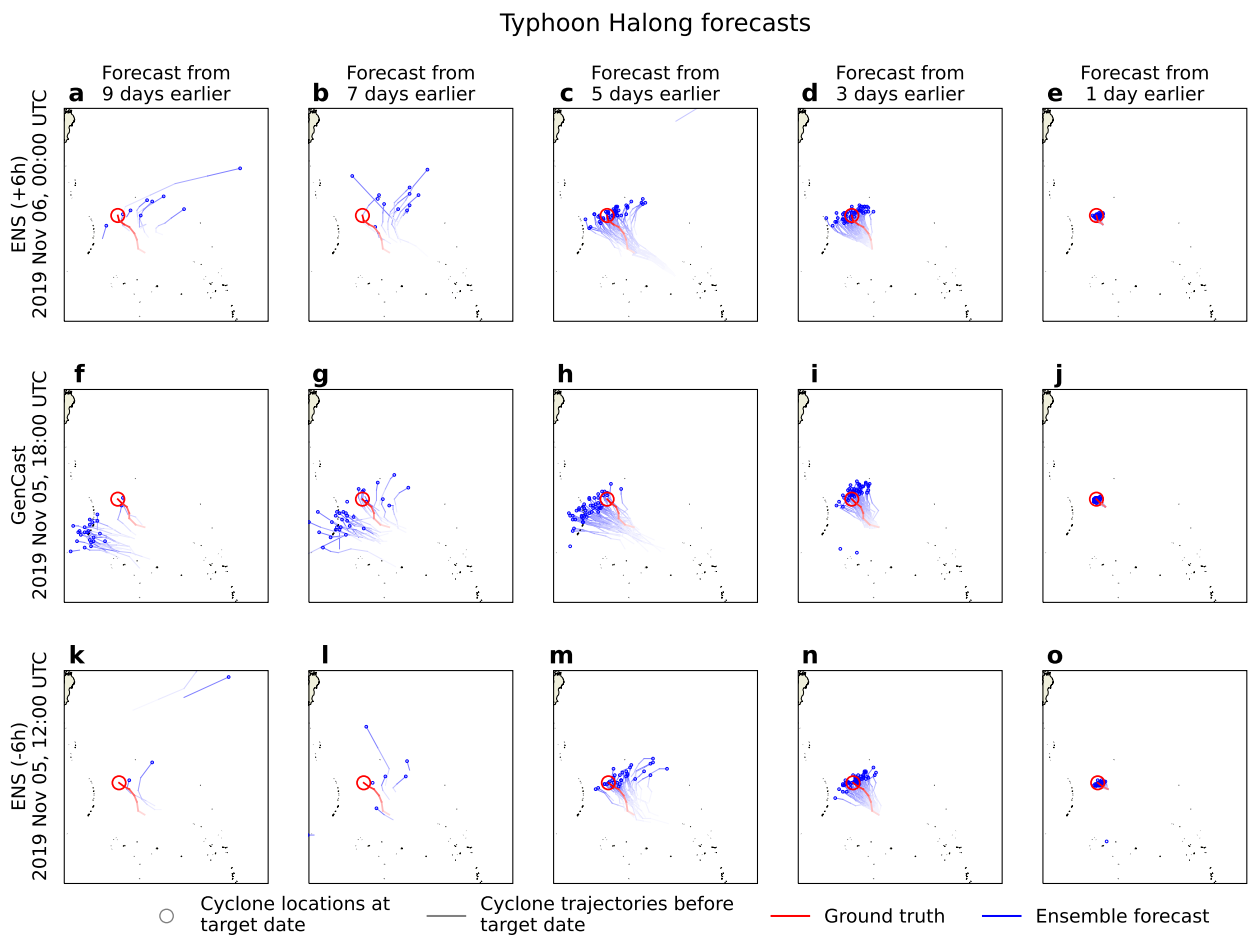


Figure G3 | Visualisation of Typhoon Halong trajectory forecasts.

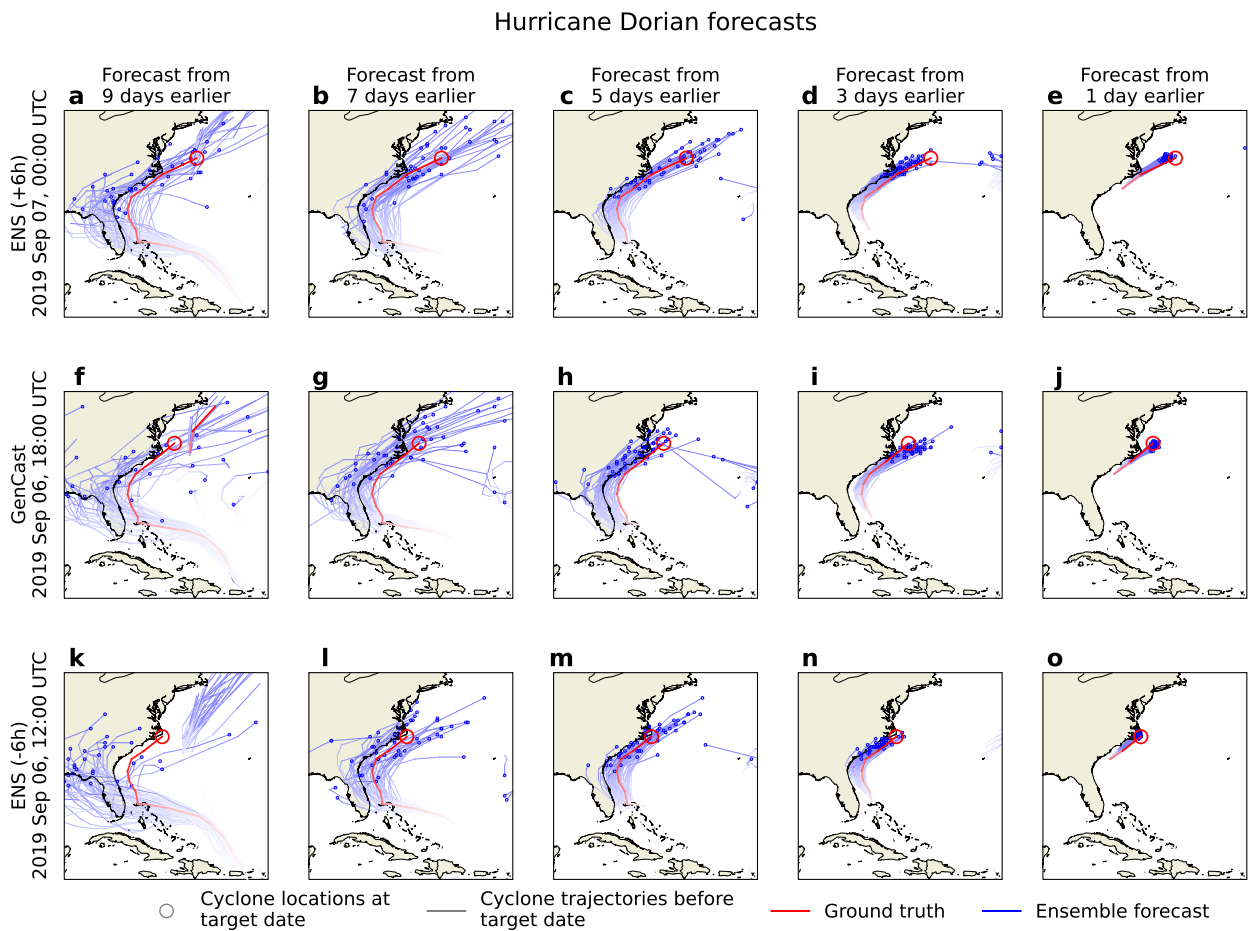


Figure G4 | Visualisation of Hurricane Dorian trajectory forecasts.

## G.2. Visualising forecasts of additional variables during Typhoon Hagibis

We provide additional visualisations of Typhoon Hagibis similar to Figure 2 for additional lead times, and 10 representative variables including specific humidity at 700 hPa (Figure G5), specific humidity at 925 hPa (Figure G6), geopotential at 500 hPa (Figure G7), geopotential at 850 hPa (Figure G8), temperature at 850 hPa (Figure G9), temperature at 300 hPa (Figure G10), u component of wind at 850 hPa (Figure G11), 2 meter temperature (Figure G12), 10 meter u component of wind (Figure G13), and mean sea level pressure (Figure G14).

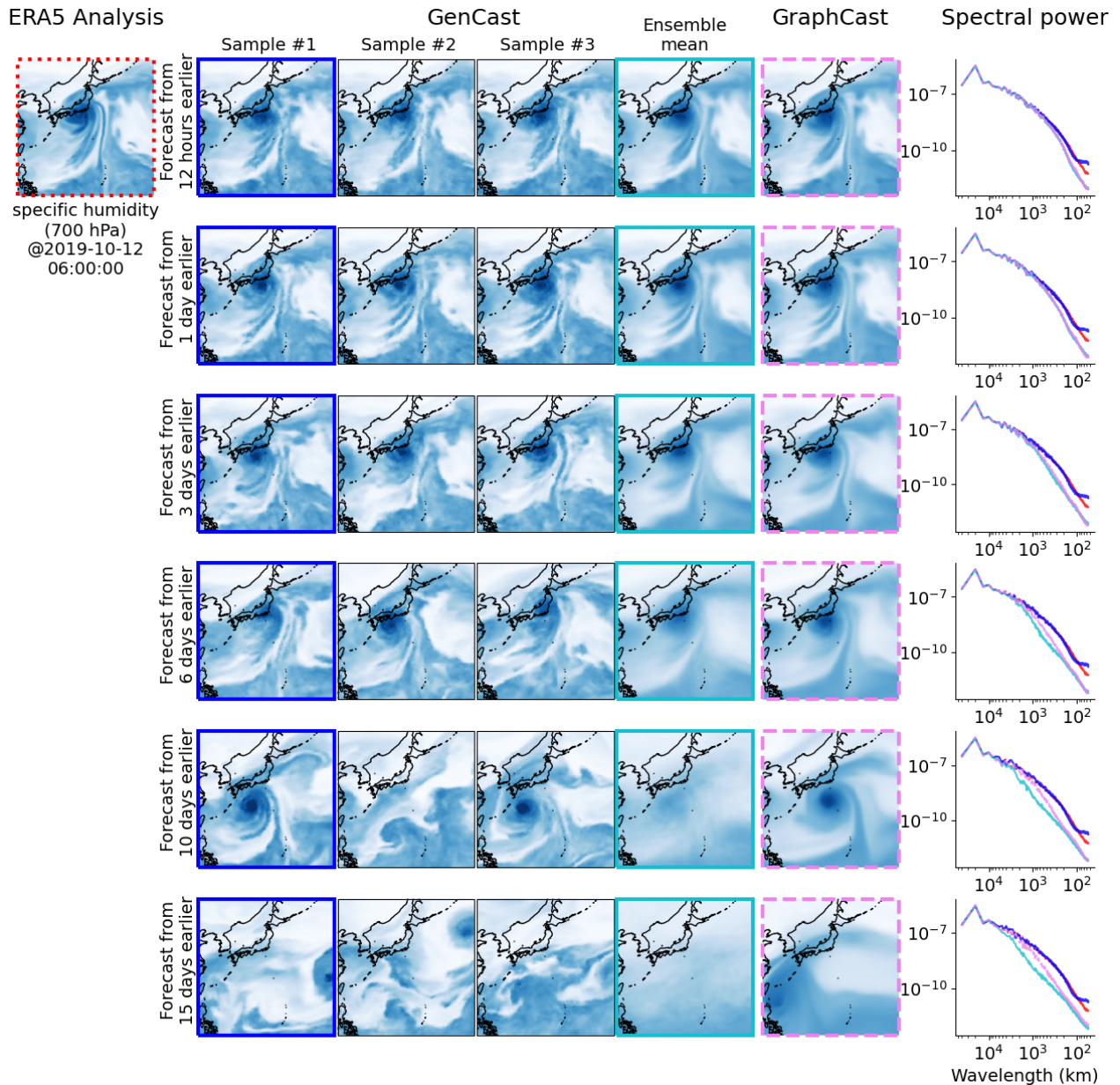


Figure G5 | Visualisation of specific humidity at 700 hPa.

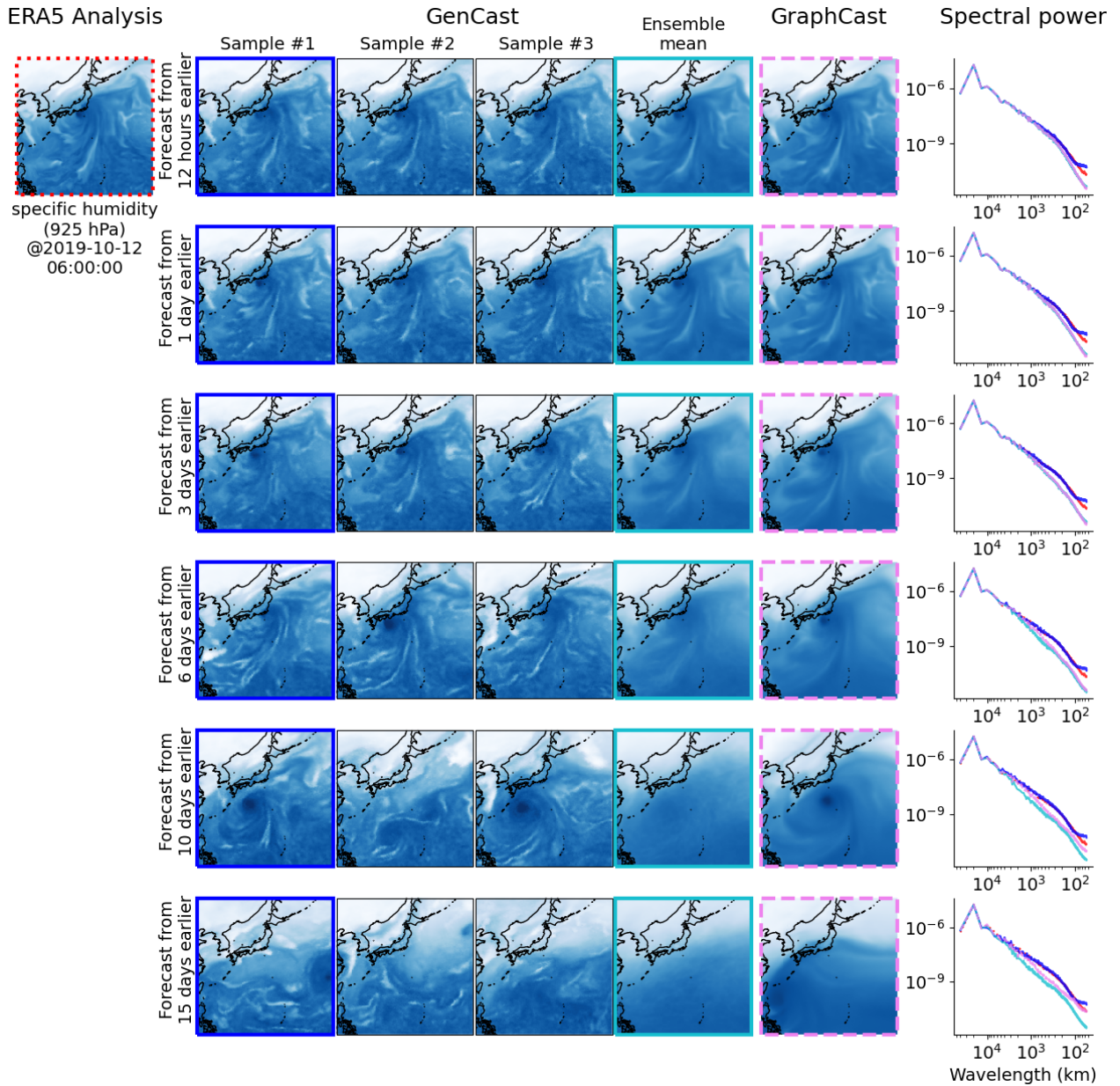


Figure G6 | Visualisation of specific humidity at 925 hPa.

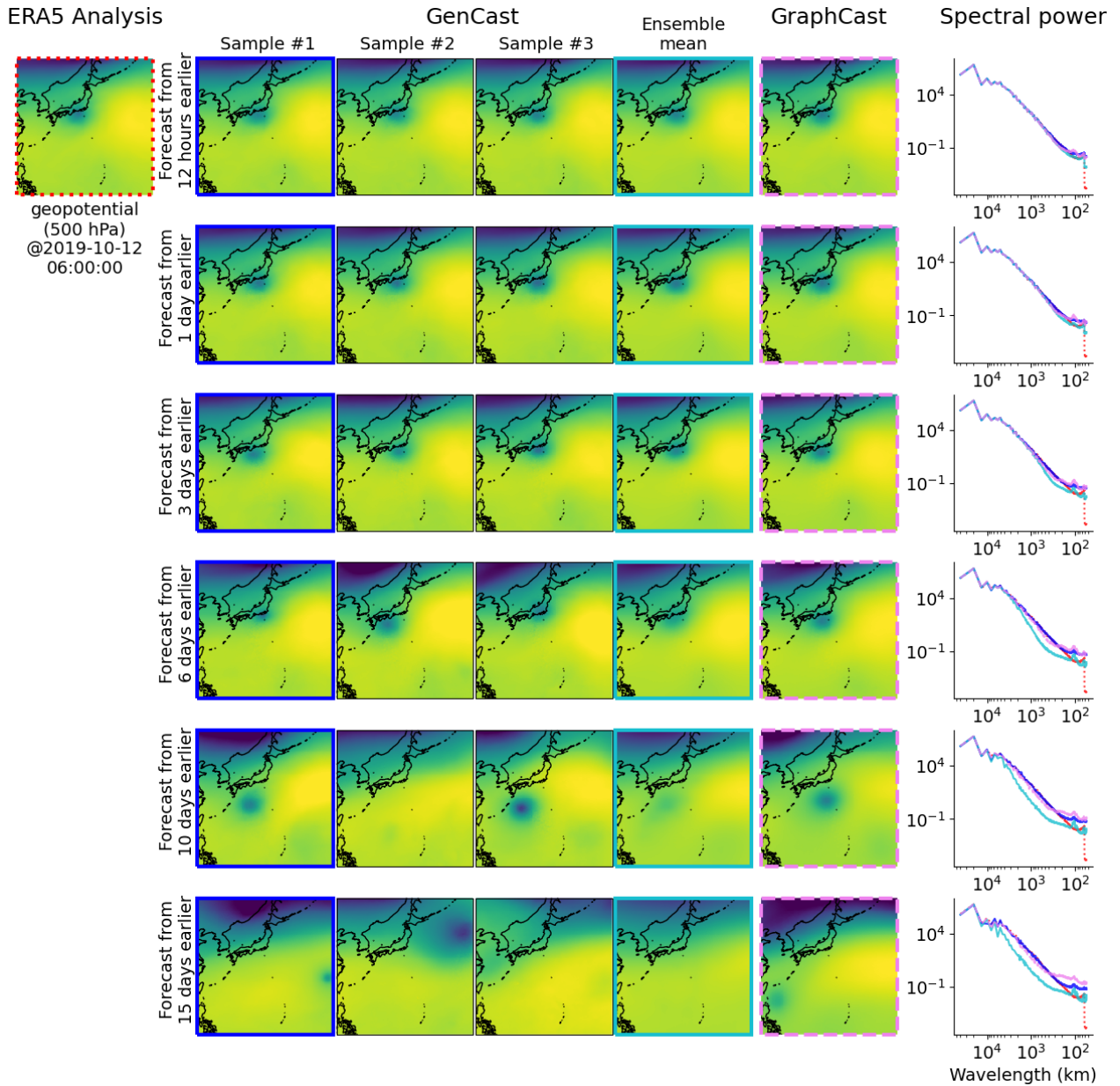


Figure G7 | Visualisation of geopotential at 500 hPa.

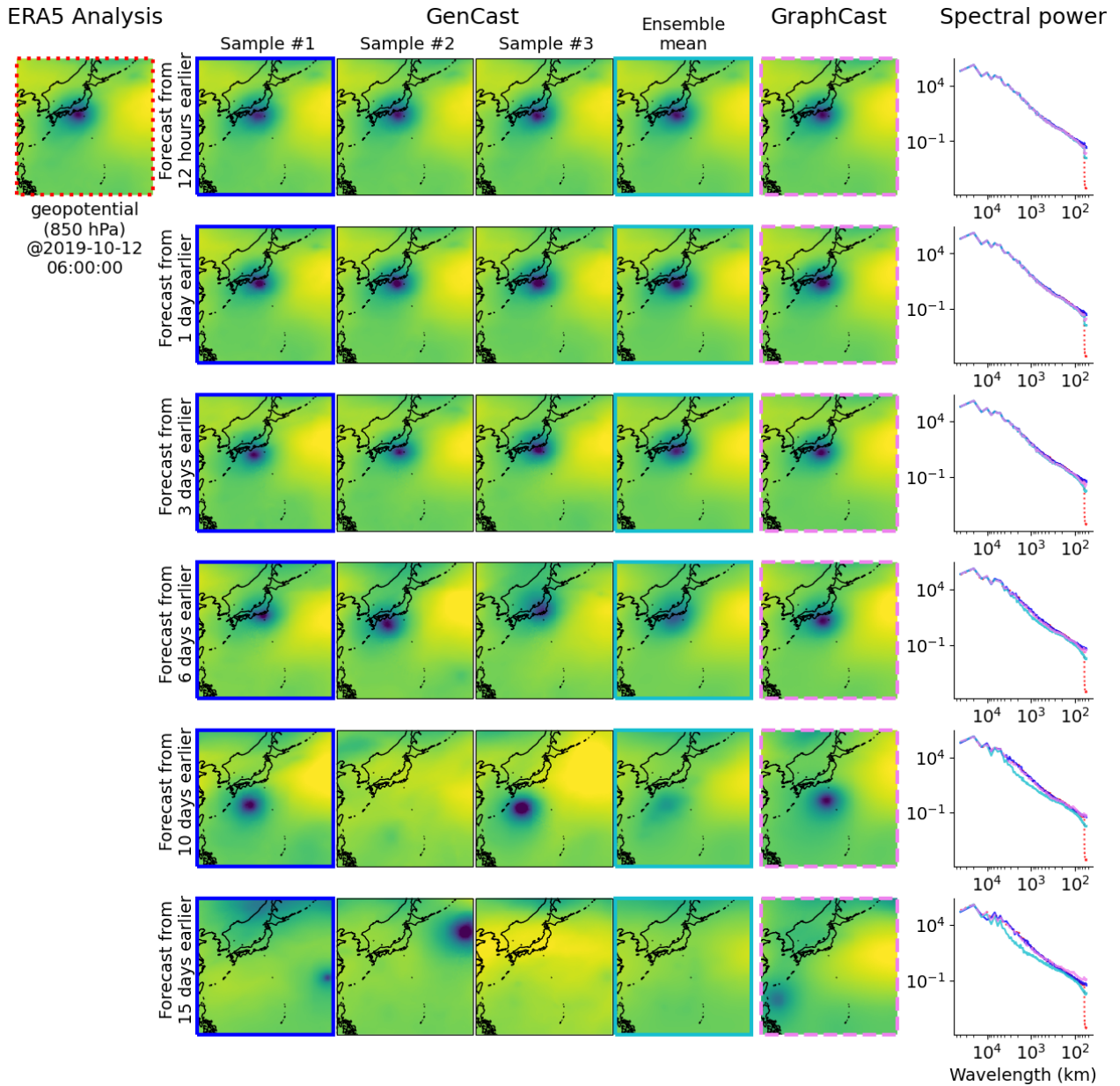


Figure G8 | Visualisation of geopotential at 850 hPa.

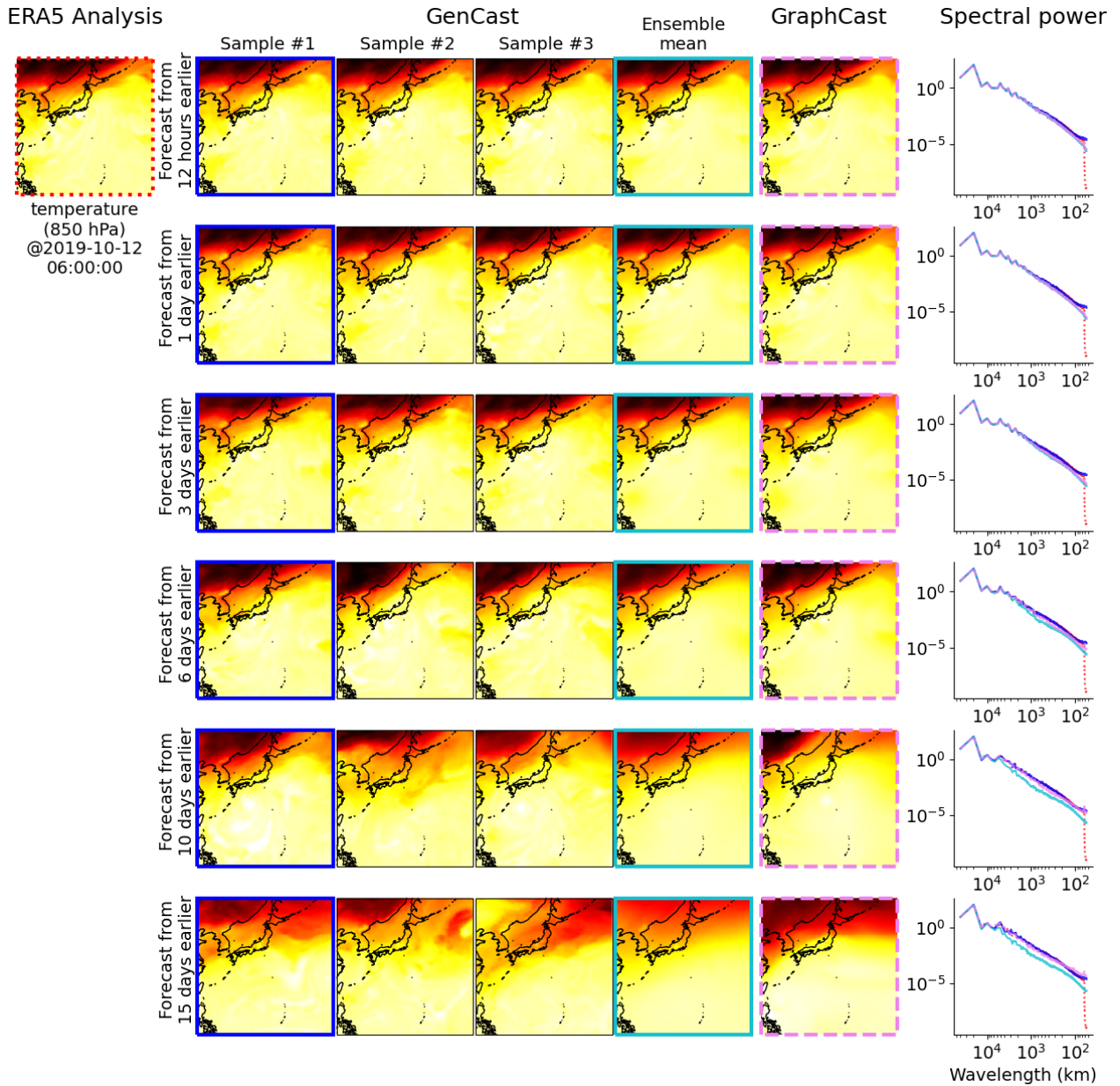


Figure G9 | Visualisation of temperature at 850 hPa.

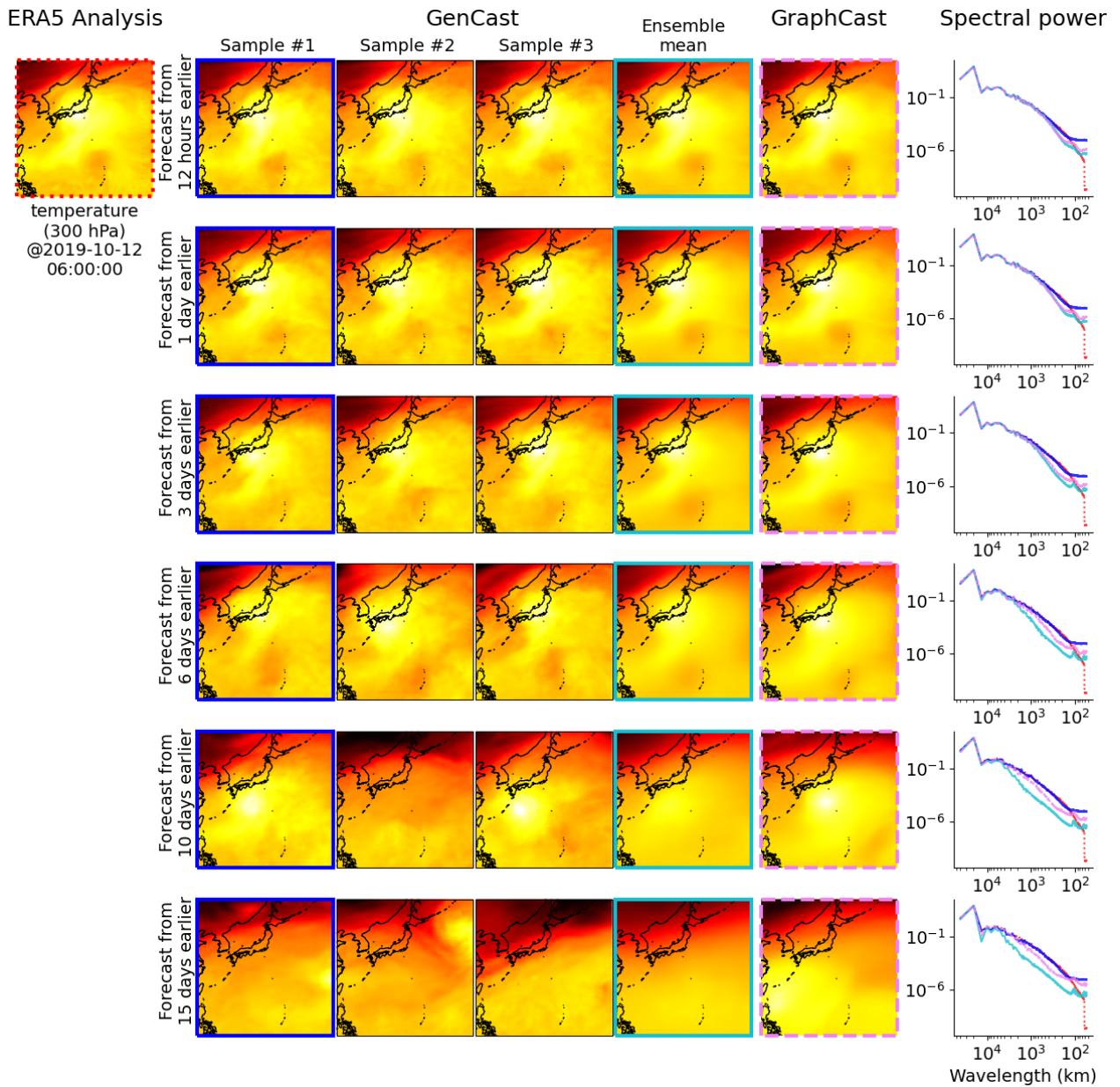


Figure G10 | Visualisation of temperature at 300 hPa.

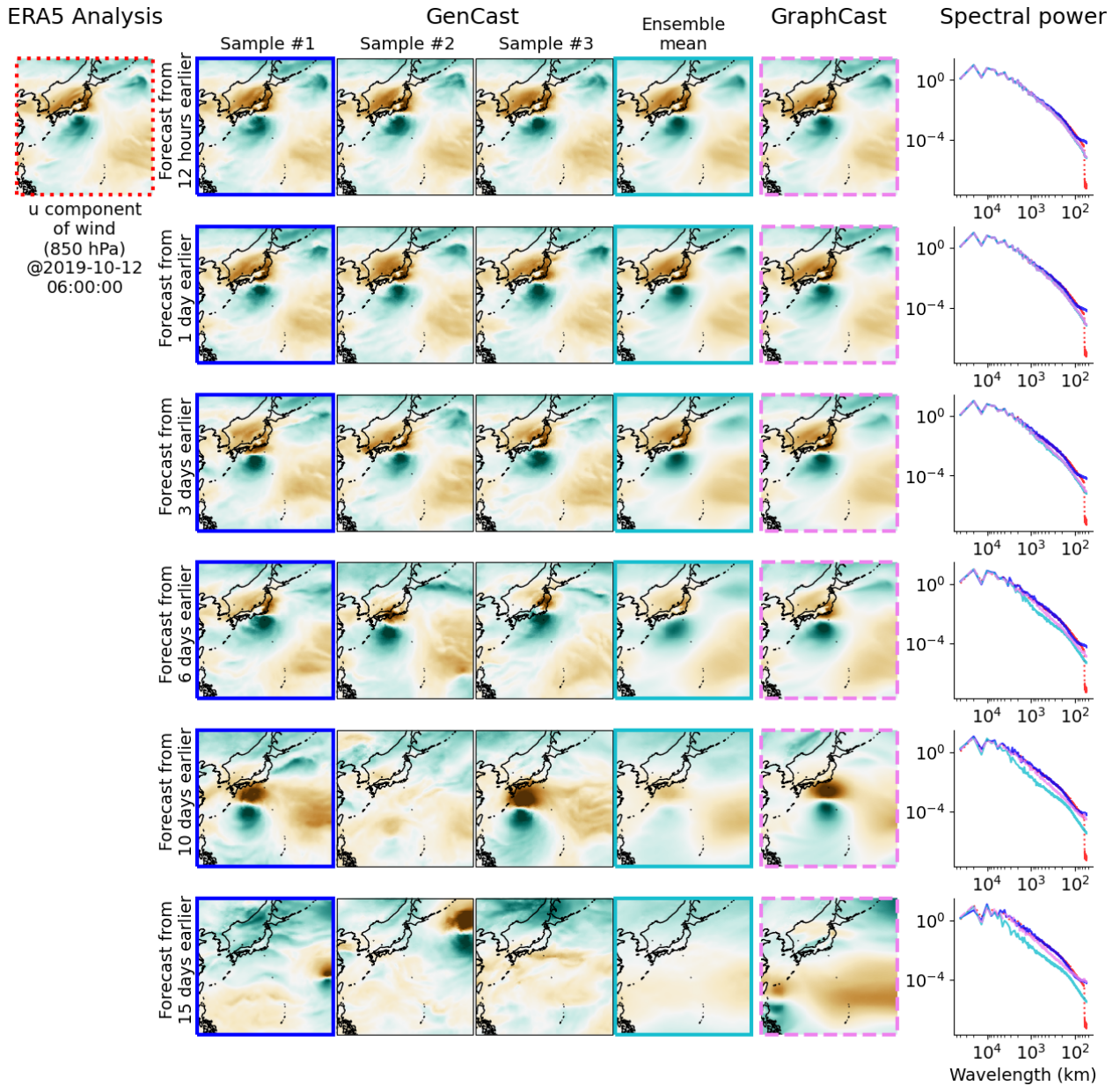


Figure G11 | Visualisation of u component of wind at 850 hPa.

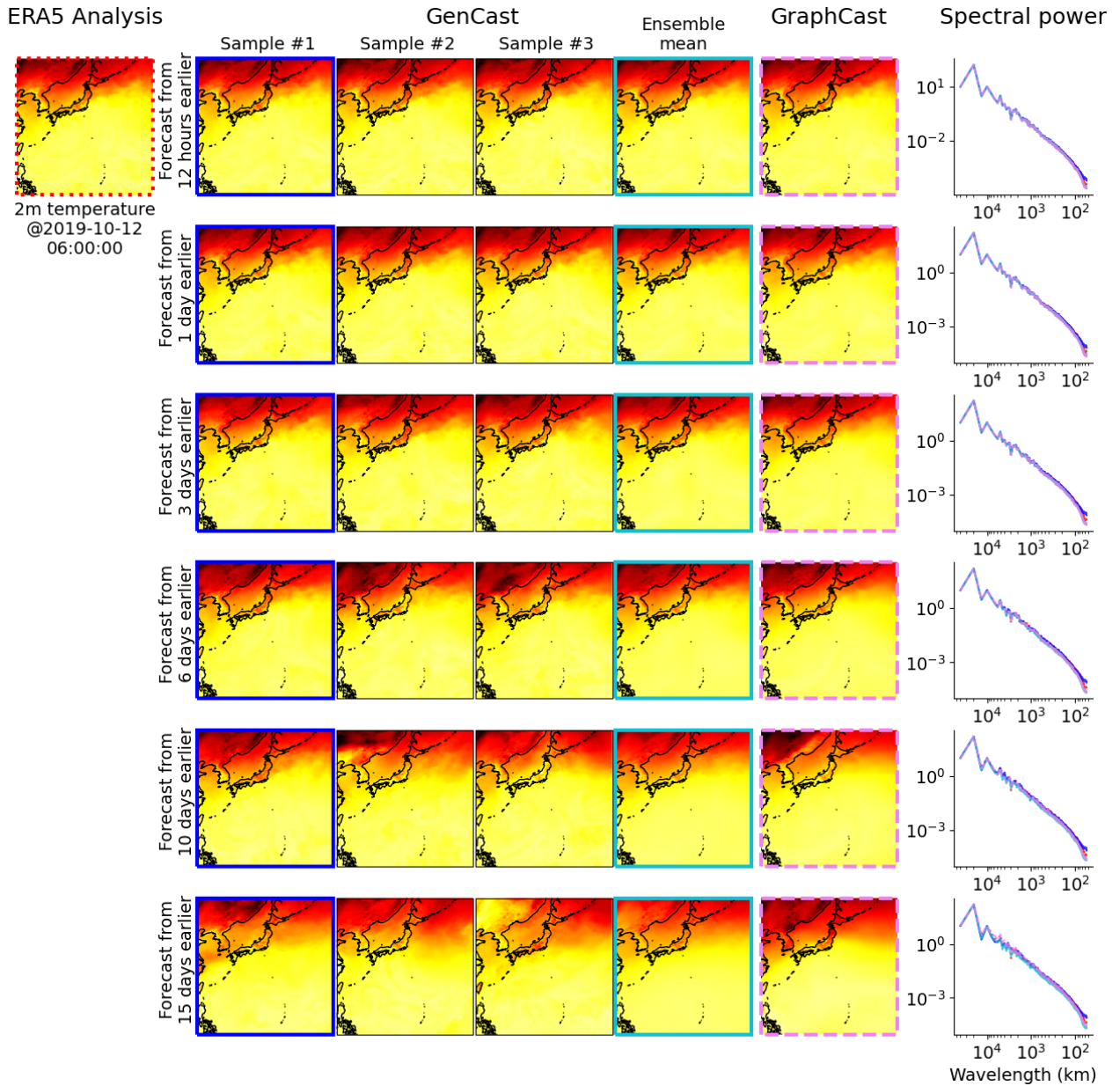


Figure G12 | Visualisation of 2 meter temperature.

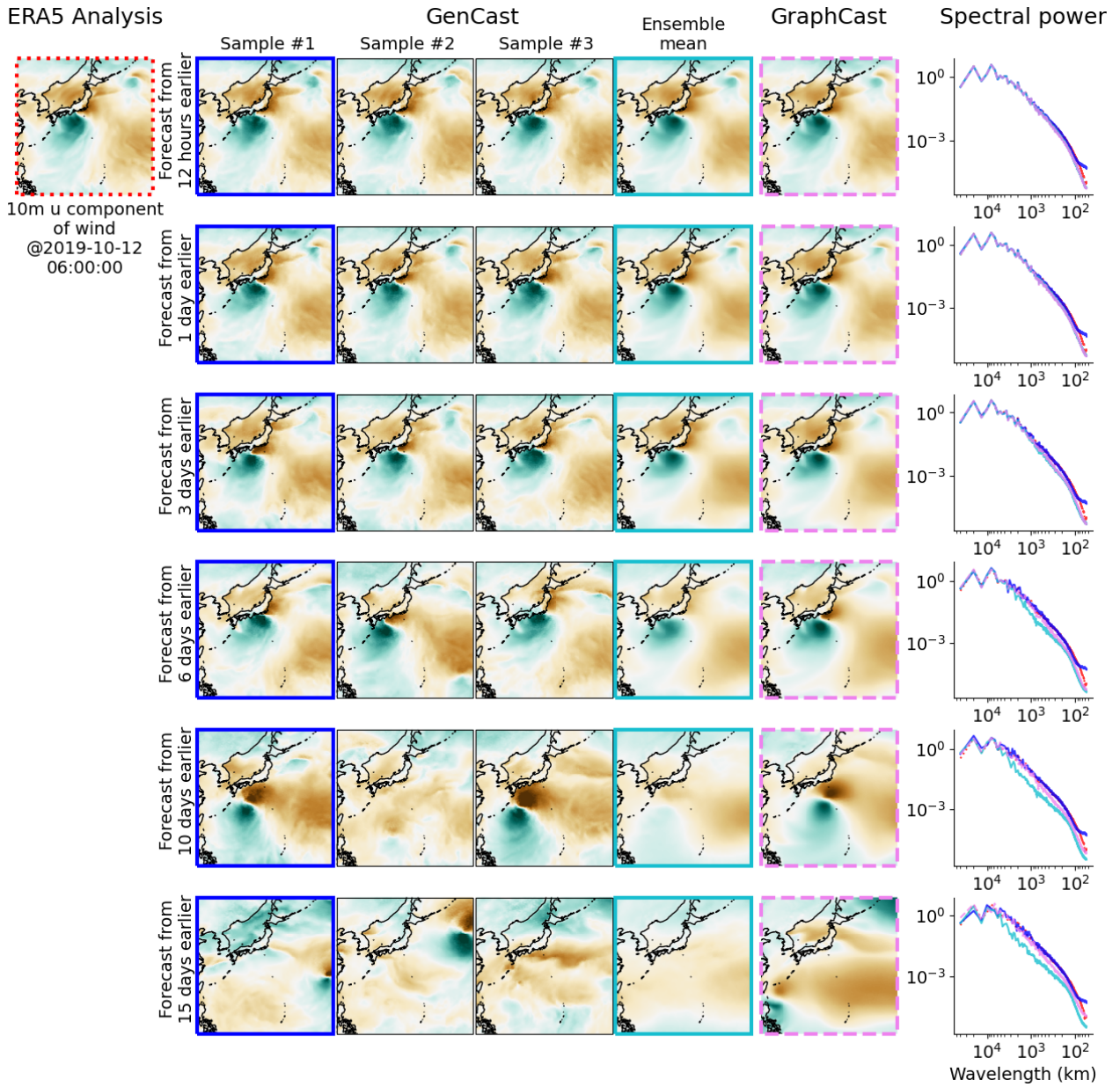


Figure G13 | Visualisation of 10 meter u component of wind.

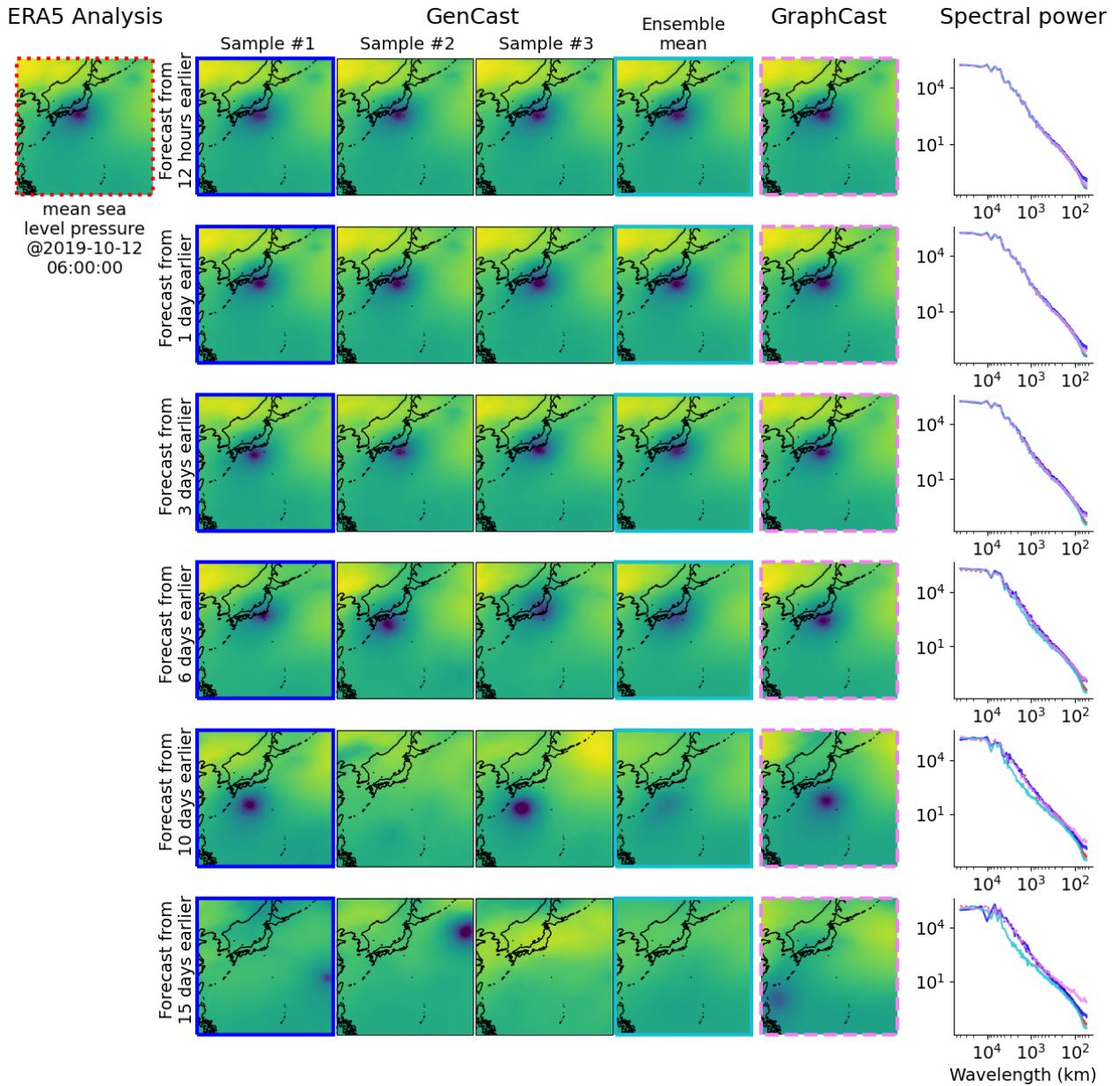
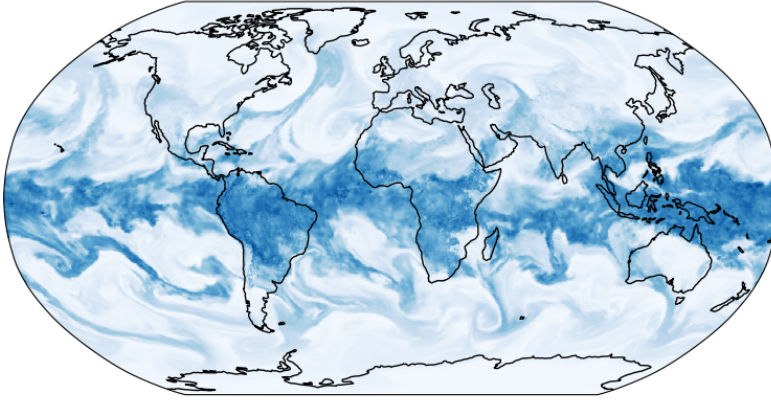


Figure G14 | Visualisation of mean sea level pressure.

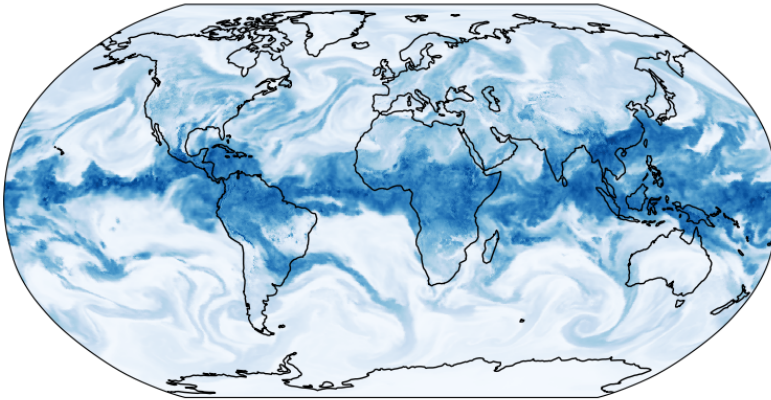
### G.3. Global forecasts

We provide representative global visualisations for various lead times, and 10 representative variables including specific humidity at 700 hPa (Figure G15), specific humidity at 925 hPa (Figure G16), geopotential at 500 hPa (Figure G17), geopotential at 850 hPa (Figure G18), temperature at 850 hPa (Figure G19), temperature at 300 hPa (Figure G20), u component of wind at 850 hPa (Figure G21), 2 meter temperature (Figure G22), 10 meter u component of wind (Figure G23), and mean sea level pressure (Figure G24). For each variable-lead time combination we choose the 2019 initialization time with median CRPS error. This means that each figure shows a snapshot from a different forecast trajectory at each lead time. In each case we plot the first ensemble member.

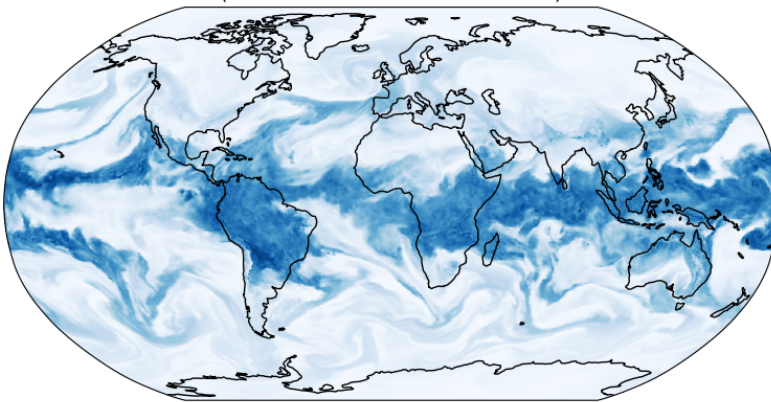
Init time: 2019-04-02 06Z UTC, Lead time: 12 hours  
(Valid time: 2019-04-02 18Z UTC)



Init time: 2019-05-25 18Z UTC, Lead time: 5 days  
(Valid time: 2019-05-30 18Z UTC)



Init time: 2019-11-17 06Z UTC, Lead time: 10 days  
(Valid time: 2019-11-27 06Z UTC)



Init time: 2019-01-11 18Z UTC, Lead time: 15 days  
(Valid time: 2019-01-26 18Z UTC)

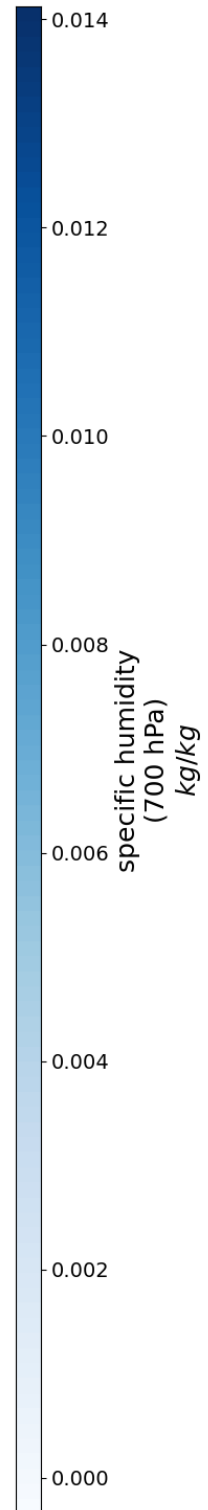
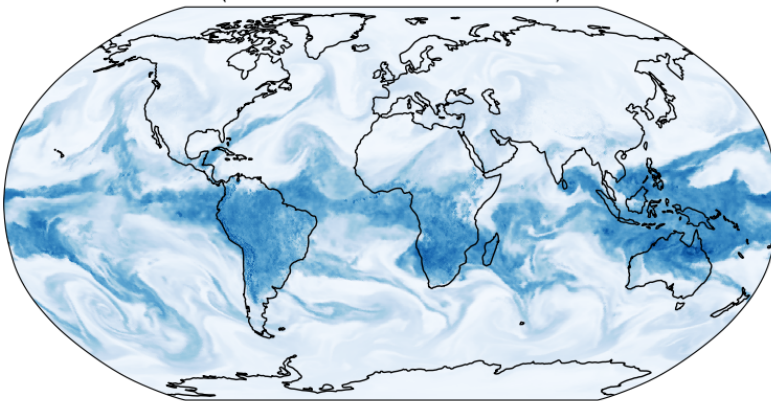
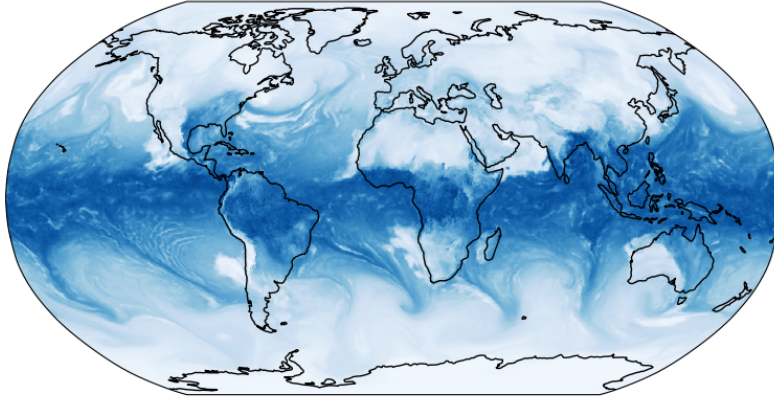
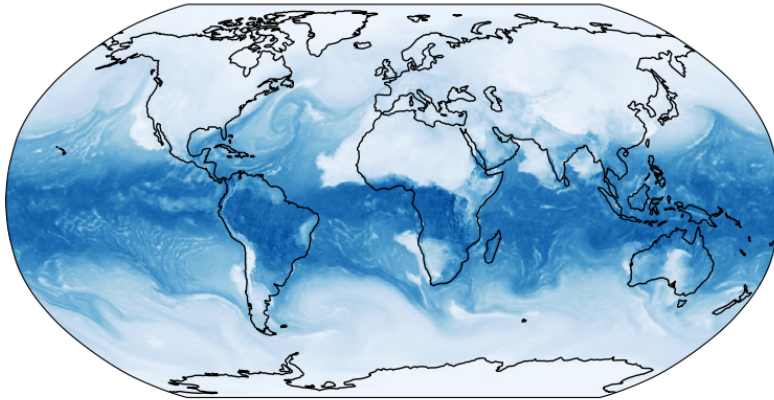


Figure G15 | Visualisation of specific humidity at 700 hPa.

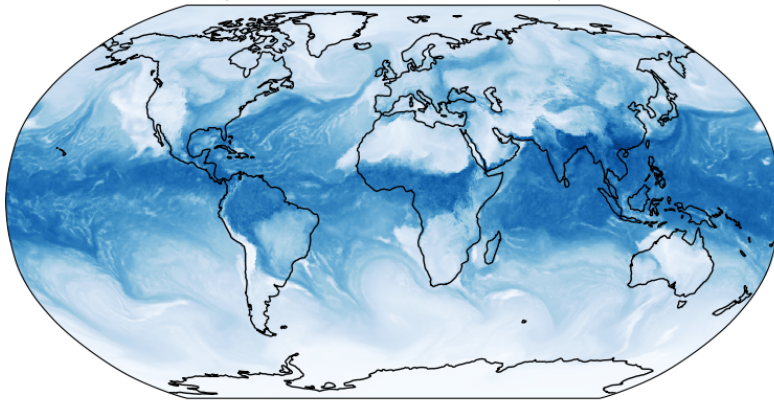
Init time: 2019-05-01 06Z UTC, Lead time: 12 hours  
(Valid time: 2019-05-01 18Z UTC)



Init time: 2019-03-11 18Z UTC, Lead time: 5 days  
(Valid time: 2019-03-16 18Z UTC)



Init time: 2019-06-12 18Z UTC, Lead time: 10 days  
(Valid time: 2019-06-22 18Z UTC)



Init time: 2019-04-20 18Z UTC, Lead time: 15 days  
(Valid time: 2019-05-05 18Z UTC)

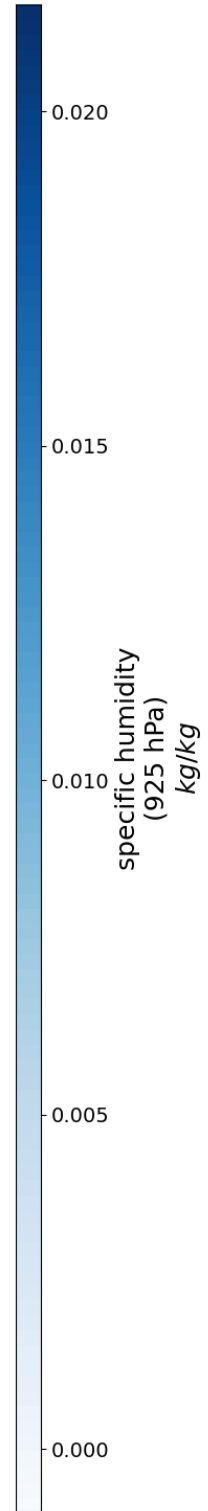
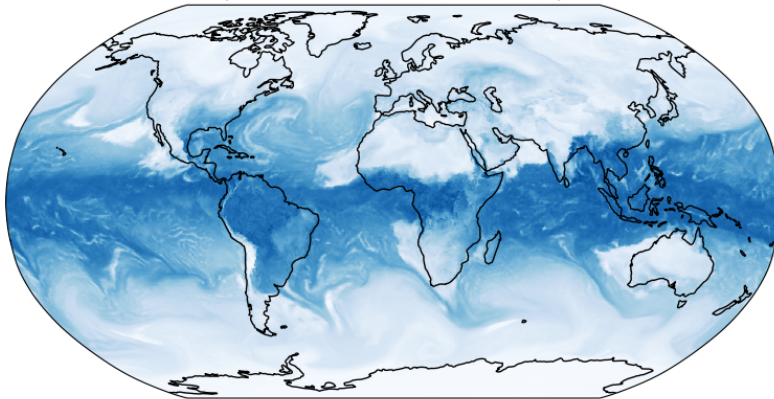
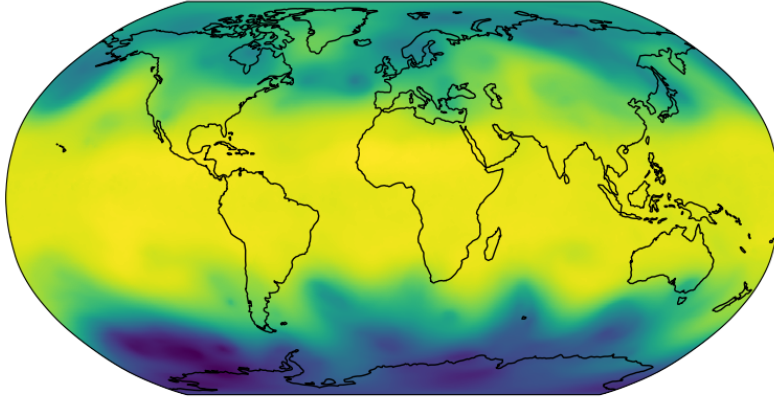
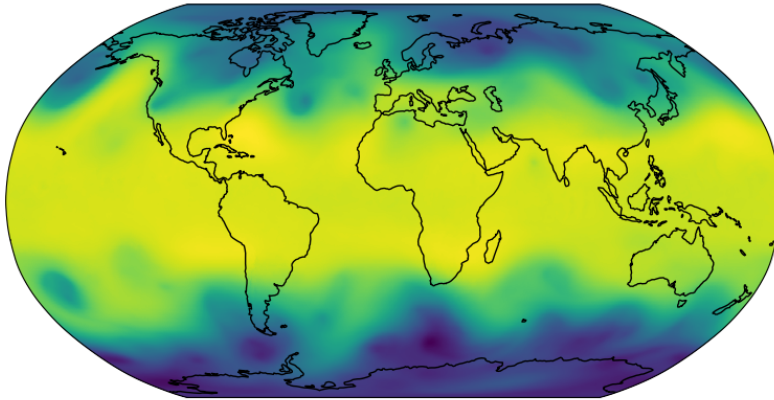


Figure G16 | Visualisation of specific humidity at 925 hPa.

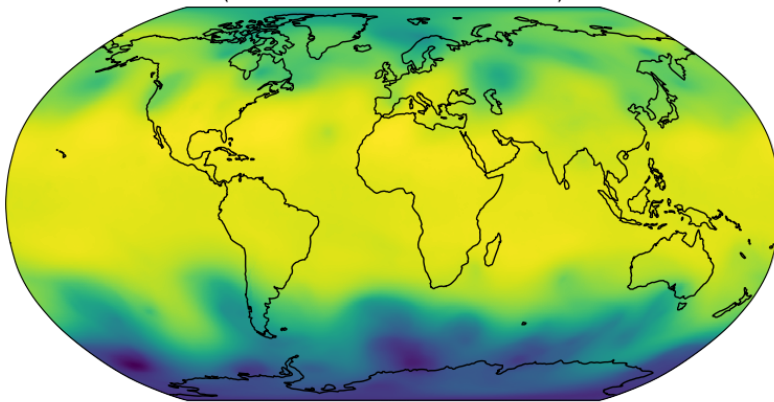
Init time: 2019-05-07 06Z UTC, Lead time: 12 hours  
(Valid time: 2019-05-07 18Z UTC)



Init time: 2019-10-22 18Z UTC, Lead time: 5 days  
(Valid time: 2019-10-27 18Z UTC)



Init time: 2019-06-19 06Z UTC, Lead time: 10 days  
(Valid time: 2019-06-29 06Z UTC)



Init time: 2019-01-14 06Z UTC, Lead time: 15 days  
(Valid time: 2019-01-29 06Z UTC)

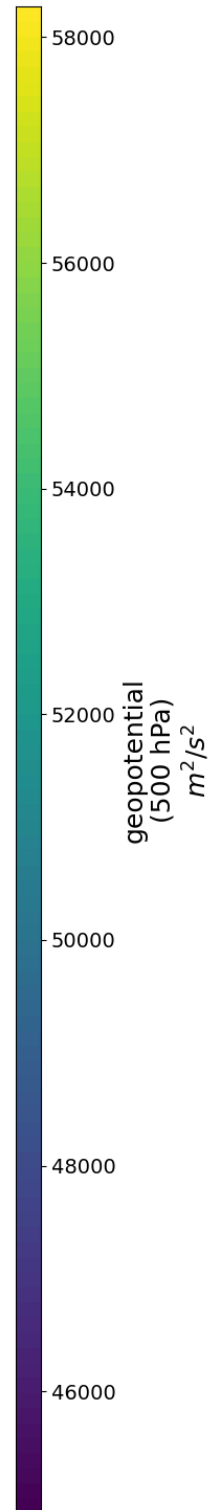
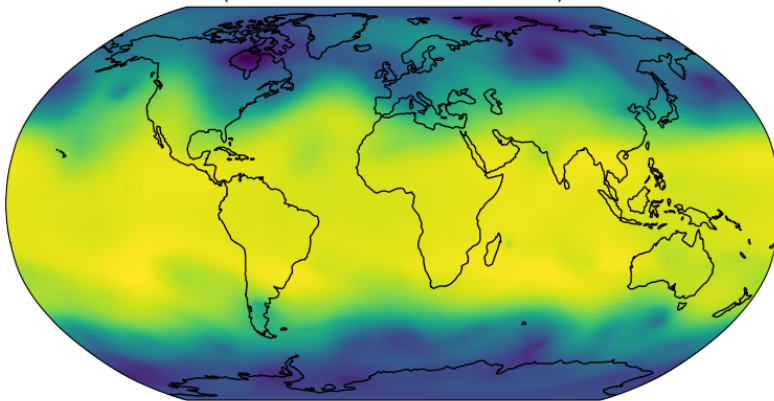
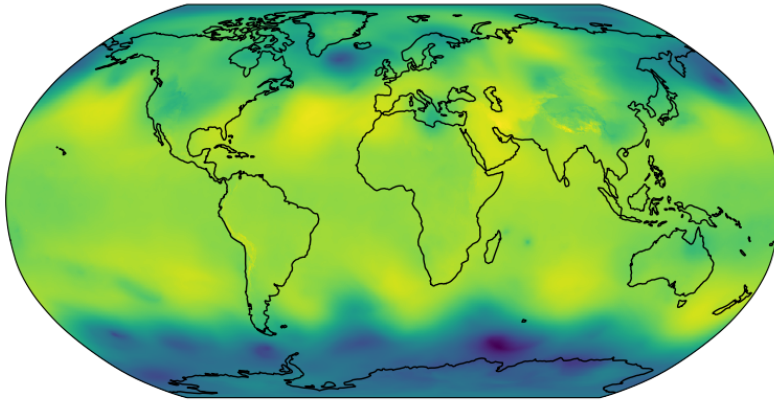
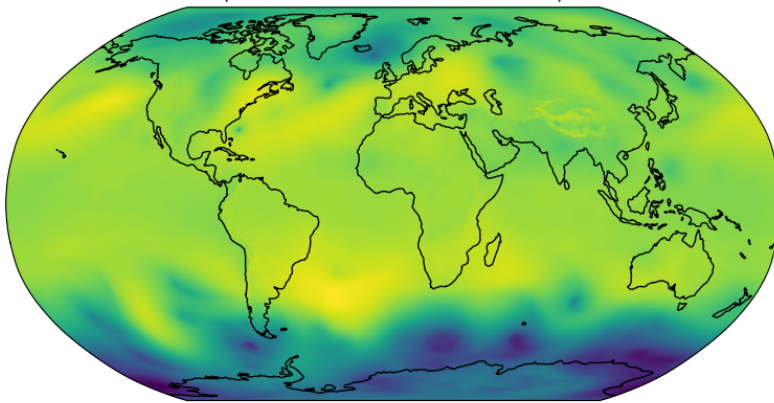


Figure G17 | Visualisation of geopotential at 500 hPa.

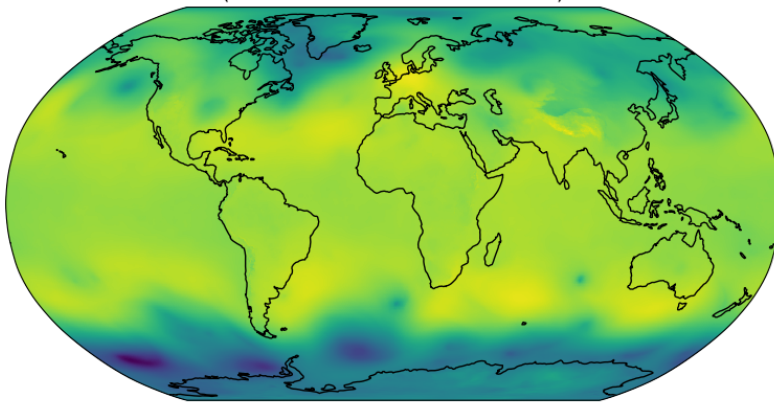
Init time: 2019-02-05 18Z UTC, Lead time: 12 hours  
(Valid time: 2019-02-06 06Z UTC)



Init time: 2019-08-21 18Z UTC, Lead time: 5 days  
(Valid time: 2019-08-26 18Z UTC)



Init time: 2019-03-16 18Z UTC, Lead time: 10 days  
(Valid time: 2019-03-26 18Z UTC)



Init time: 2019-10-29 06Z UTC, Lead time: 15 days  
(Valid time: 2019-11-13 06Z UTC)

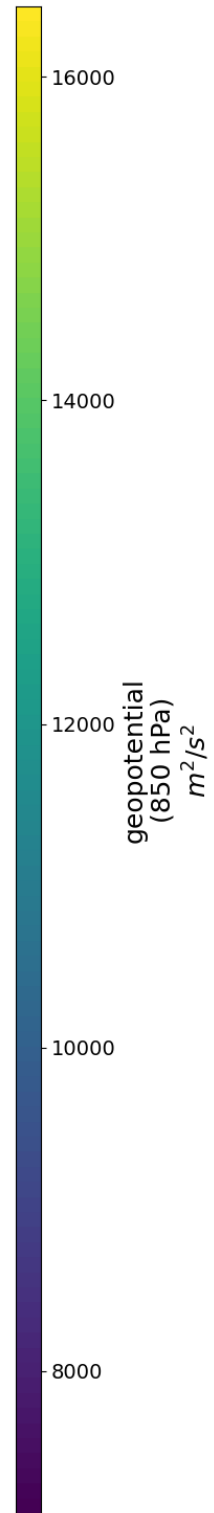
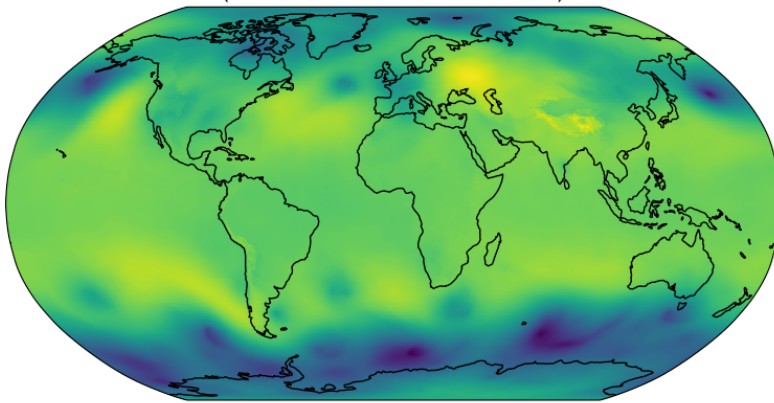
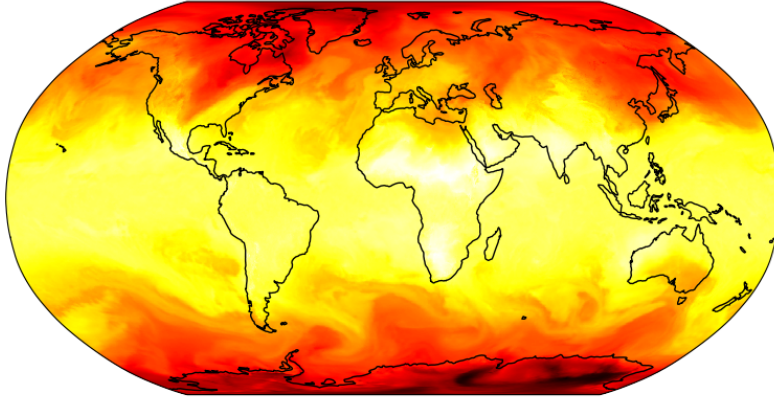
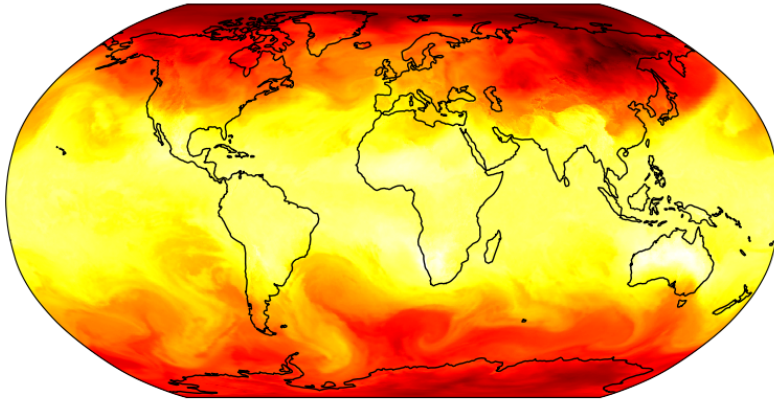


Figure G18 | Visualisation of geopotential at 850 hPa.

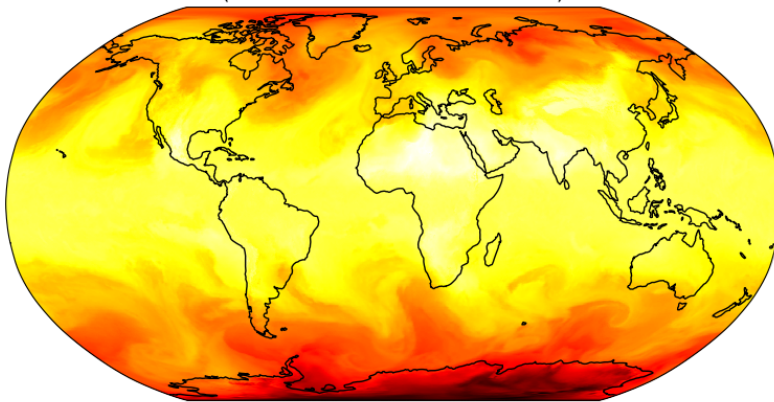
Init time: 2019-03-30 06Z UTC, Lead time: 12 hours  
(Valid time: 2019-03-30 18Z UTC)



Init time: 2019-11-21 06Z UTC, Lead time: 5 days  
(Valid time: 2019-11-26 06Z UTC)



Init time: 2019-05-12 18Z UTC, Lead time: 10 days  
(Valid time: 2019-05-22 18Z UTC)



Init time: 2019-05-26 06Z UTC, Lead time: 15 days  
(Valid time: 2019-06-10 06Z UTC)

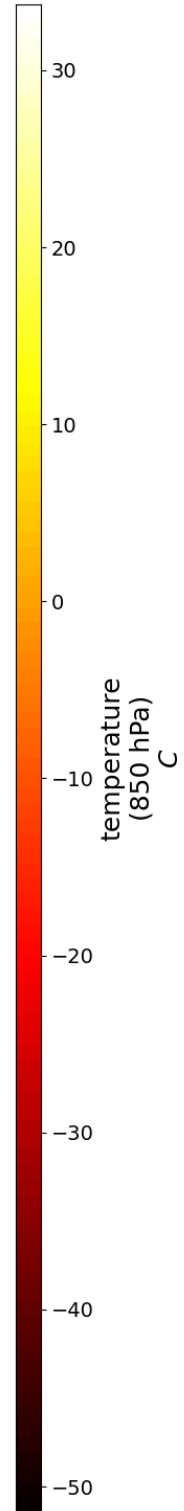
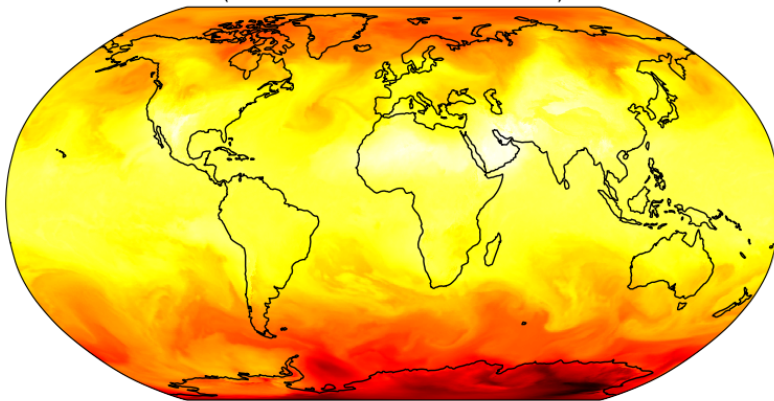
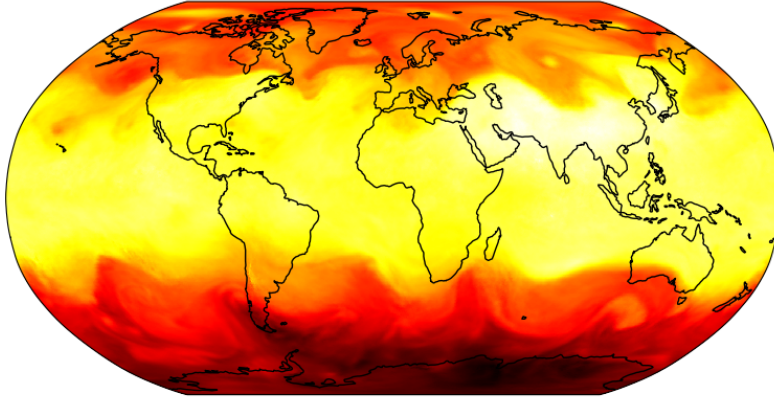
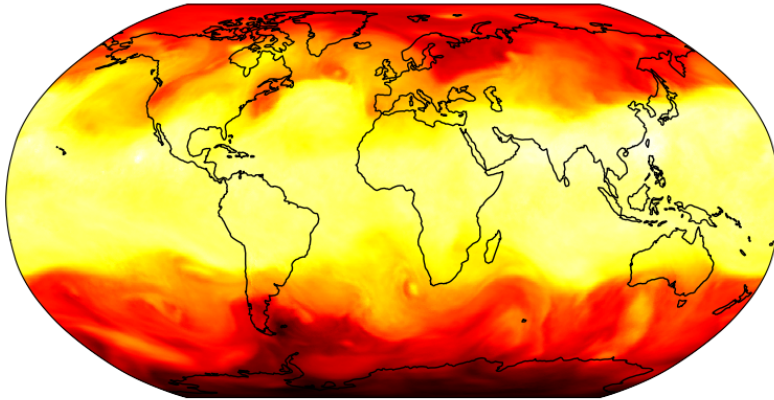


Figure G19 | Visualisation of temperature at 850 hPa.

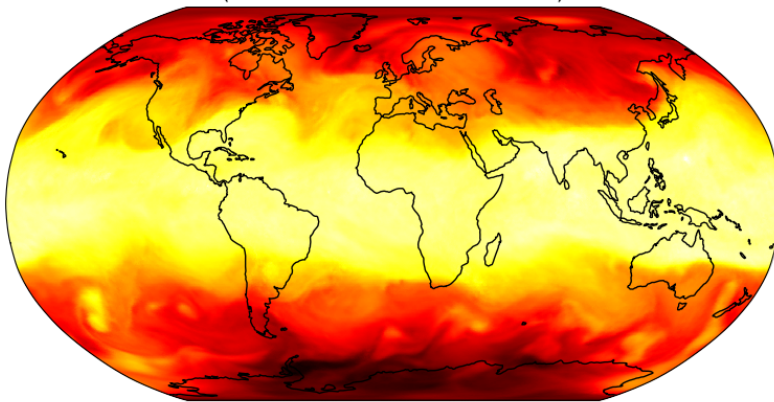
Init time: 2019-07-20 18Z UTC, Lead time: 12 hours  
(Valid time: 2019-07-21 06Z UTC)



Init time: 2019-09-14 18Z UTC, Lead time: 5 days  
(Valid time: 2019-09-19 18Z UTC)



Init time: 2019-10-15 18Z UTC, Lead time: 10 days  
(Valid time: 2019-10-25 18Z UTC)



Init time: 2019-10-14 18Z UTC, Lead time: 15 days  
(Valid time: 2019-10-29 18Z UTC)

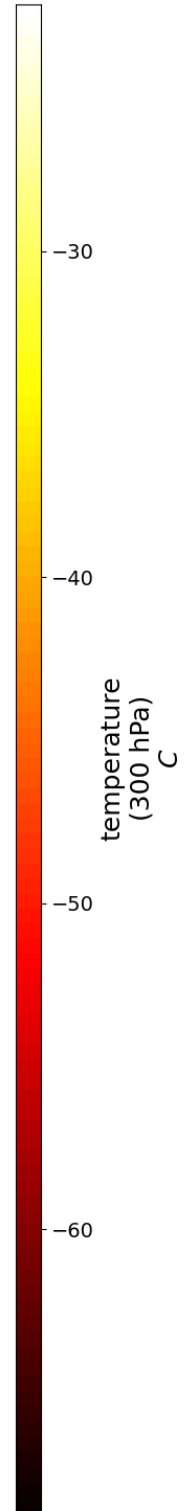
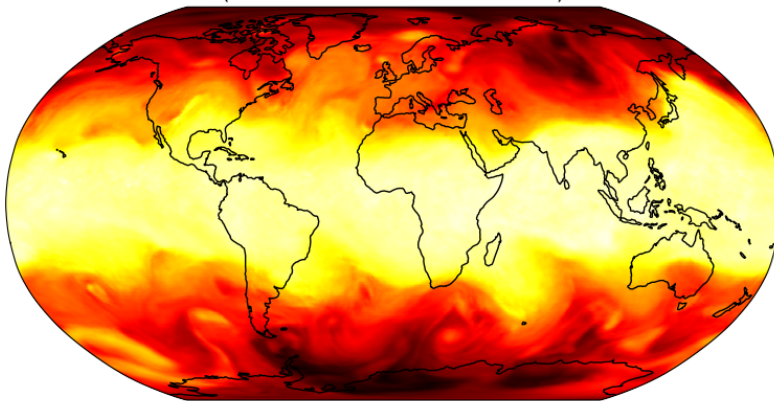
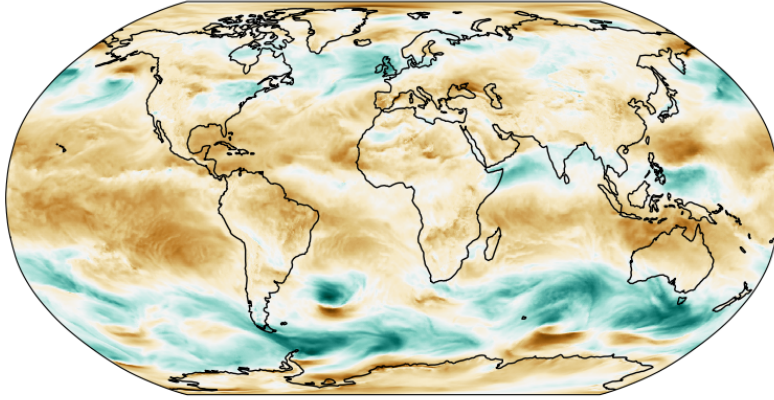
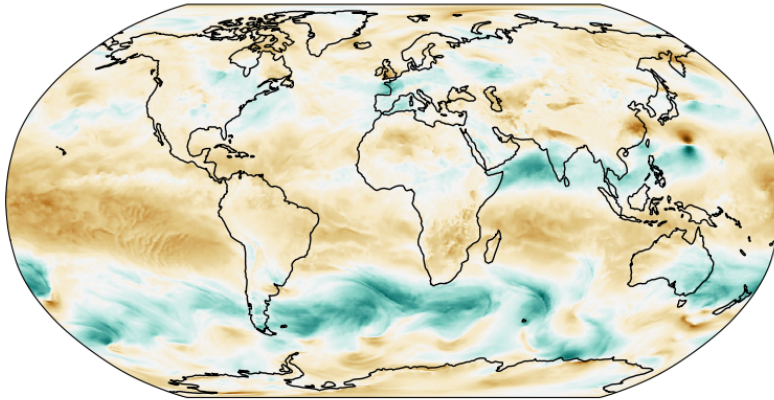


Figure G20 | Visualisation of temperature at 300 hPa.

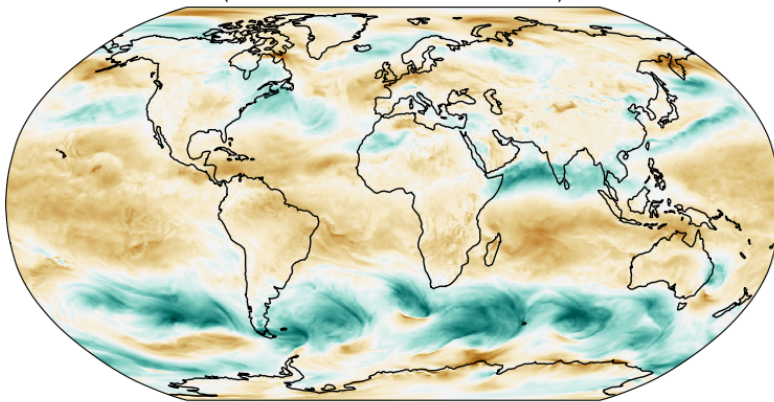
Init time: 2019-09-10 18Z UTC, Lead time: 12 hours  
(Valid time: 2019-09-11 06Z UTC)



Init time: 2019-08-04 18Z UTC, Lead time: 5 days  
(Valid time: 2019-08-09 18Z UTC)



Init time: 2019-06-01 18Z UTC, Lead time: 10 days  
(Valid time: 2019-06-11 18Z UTC)



Init time: 2019-07-23 06Z UTC, Lead time: 15 days  
(Valid time: 2019-08-07 06Z UTC)

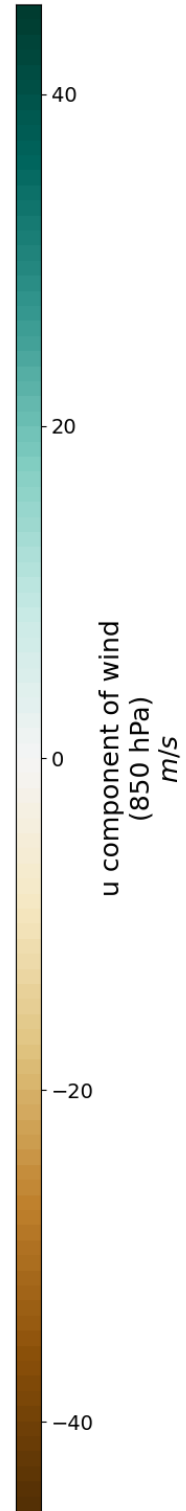
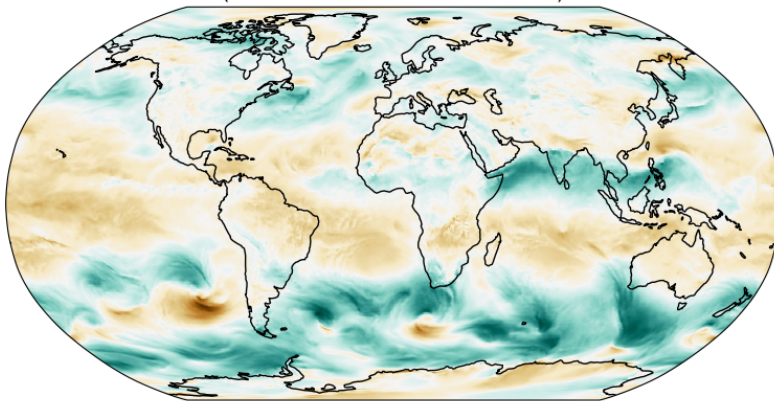
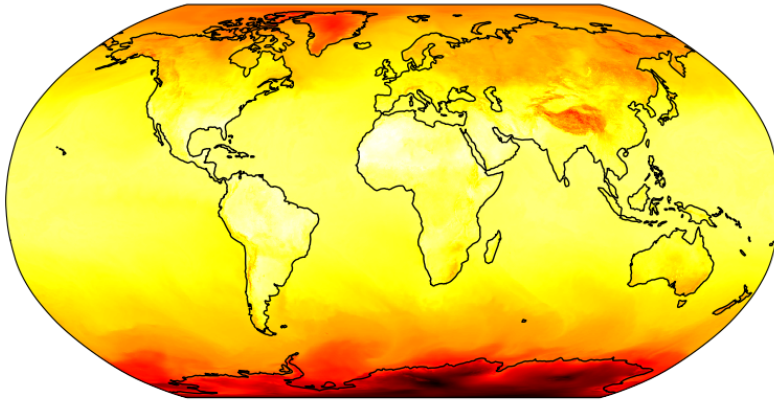
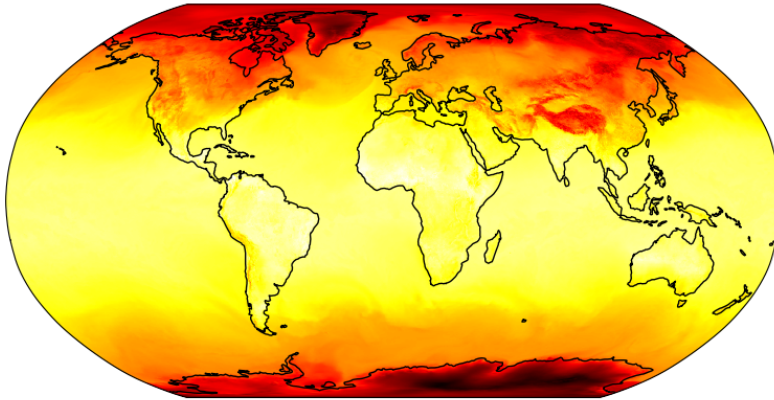


Figure G21 | Visualisation of u component of wind at 850 hPa.

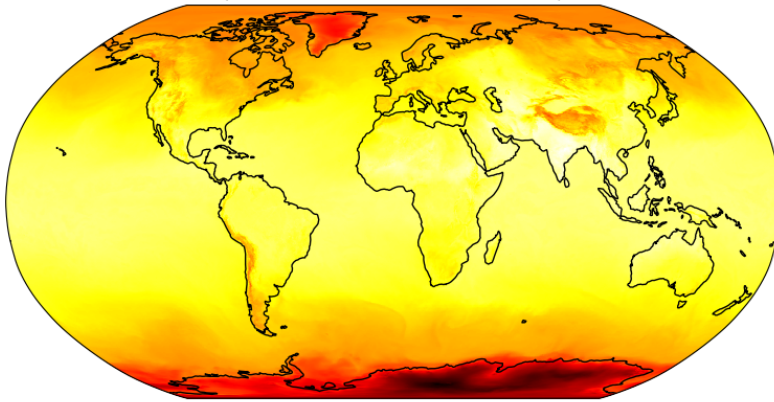
Init time: 2019-09-25 06Z UTC, Lead time: 12 hours  
(Valid time: 2019-09-25 18Z UTC)



Init time: 2019-03-06 18Z UTC, Lead time: 5 days  
(Valid time: 2019-03-11 18Z UTC)



Init time: 2019-04-30 06Z UTC, Lead time: 10 days  
(Valid time: 2019-05-10 06Z UTC)



Init time: 2019-03-25 18Z UTC, Lead time: 15 days  
(Valid time: 2019-04-09 18Z UTC)

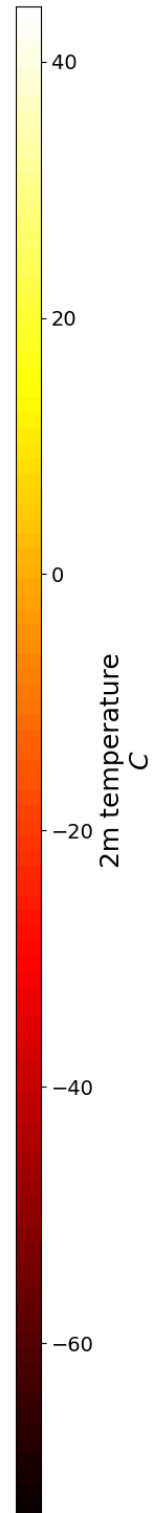
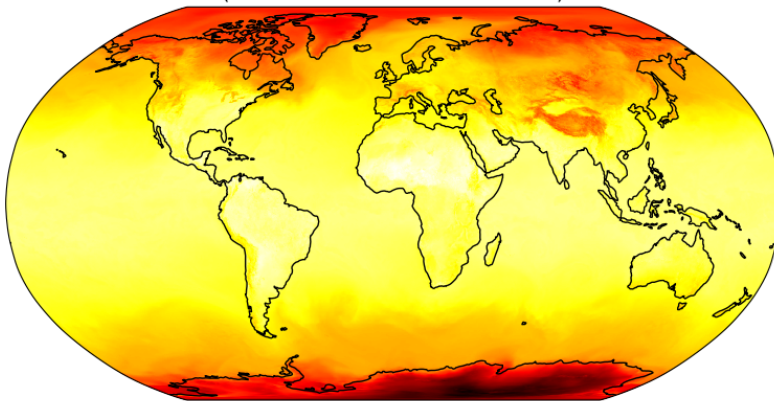
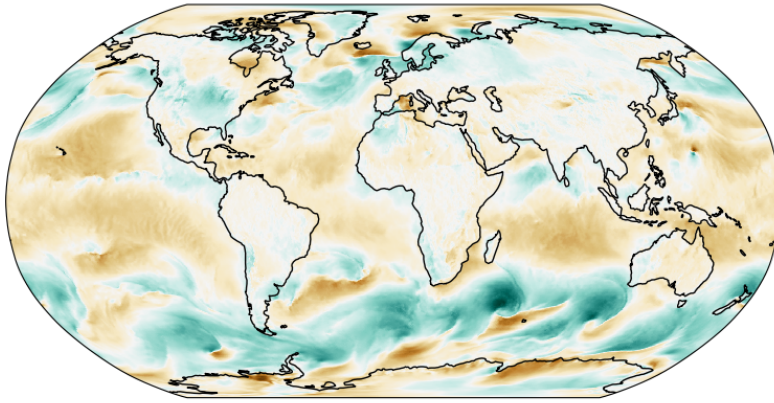
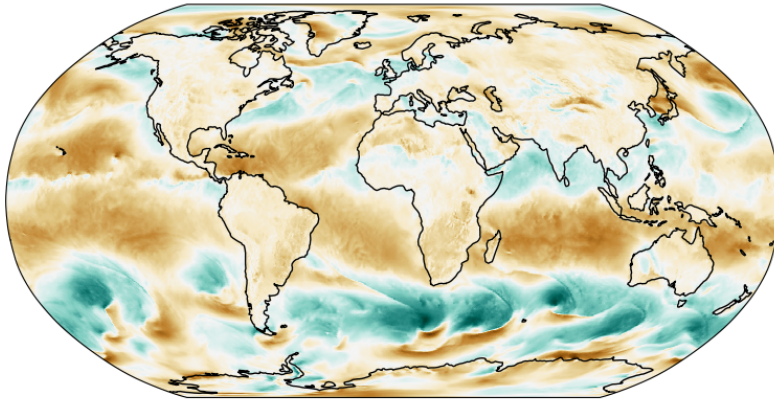


Figure G22 | Visualisation of 2 meter temperature.

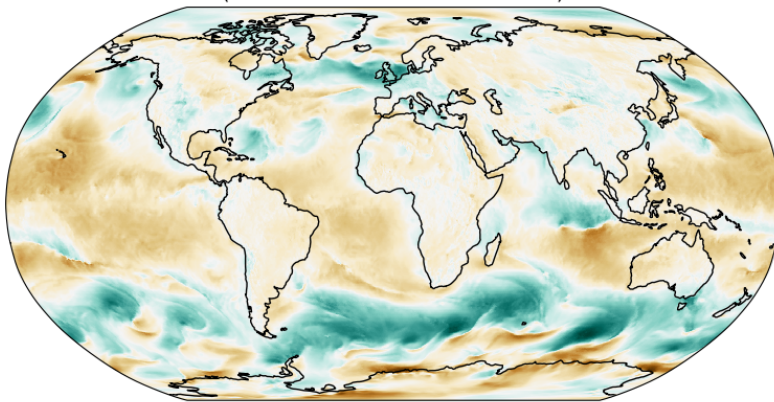
Init time: 2019-10-22 06Z UTC, Lead time: 12 hours  
(Valid time: 2019-10-22 18Z UTC)



Init time: 2019-08-10 06Z UTC, Lead time: 5 days  
(Valid time: 2019-08-15 06Z UTC)



Init time: 2019-04-15 18Z UTC, Lead time: 10 days  
(Valid time: 2019-04-25 18Z UTC)



Init time: 2019-11-28 06Z UTC, Lead time: 15 days  
(Valid time: 2019-12-13 06Z UTC)

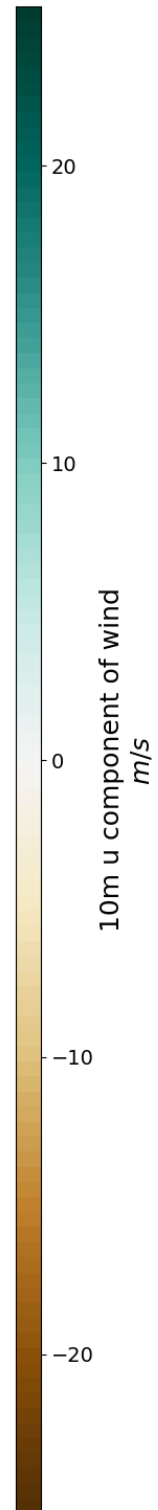
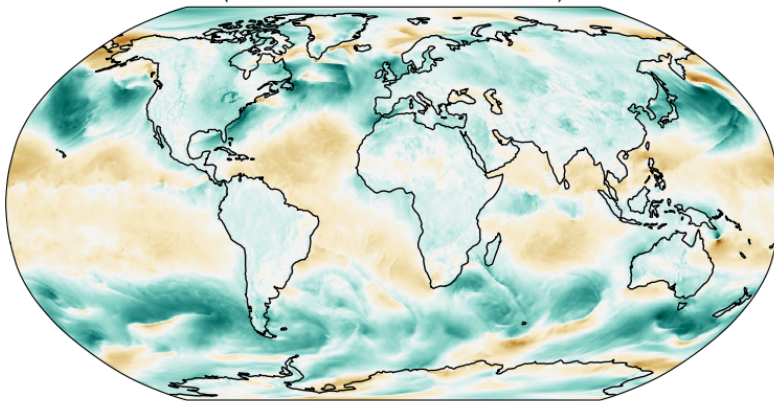
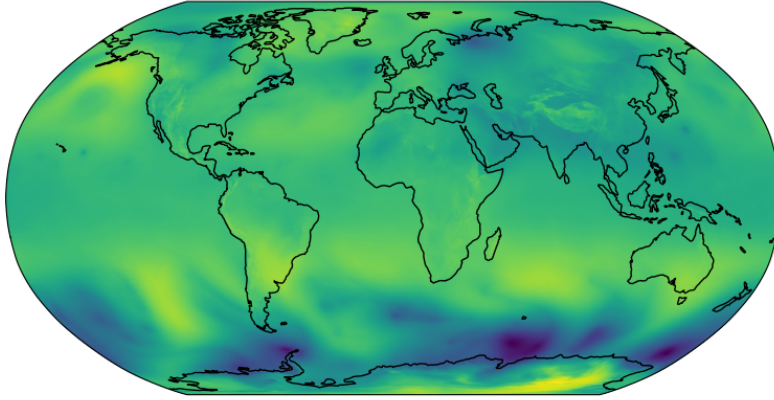
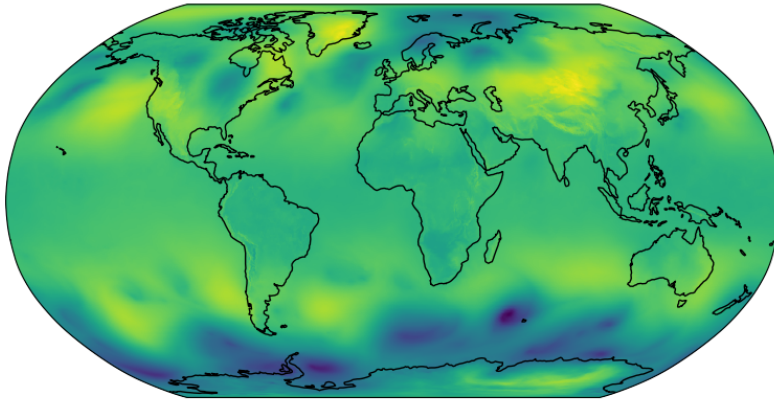


Figure G23 | Visualisation of 10 meter u component of wind.

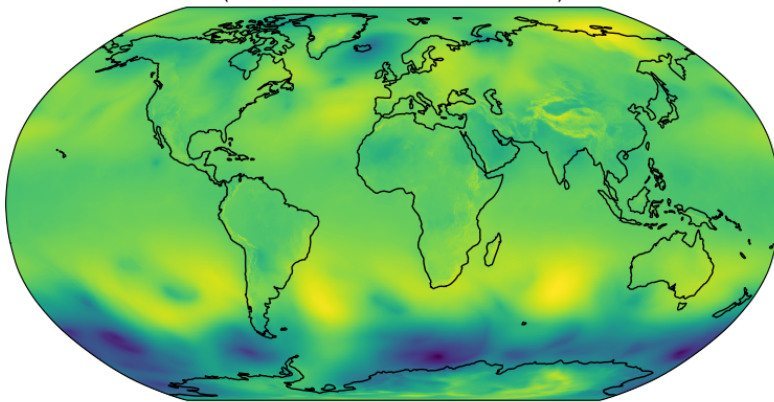
Init time: 2019-08-03 18Z UTC, Lead time: 12 hours  
(Valid time: 2019-08-04 06Z UTC)



Init time: 2019-10-17 18Z UTC, Lead time: 5 days  
(Valid time: 2019-10-22 18Z UTC)



Init time: 2019-08-14 18Z UTC, Lead time: 10 days  
(Valid time: 2019-08-24 18Z UTC)



Init time: 2019-10-31 06Z UTC, Lead time: 15 days  
(Valid time: 2019-11-15 06Z UTC)

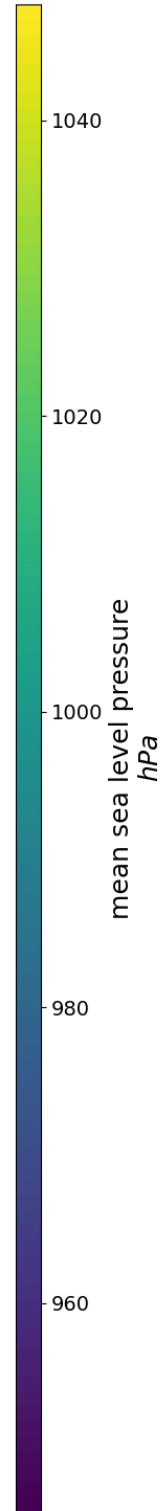
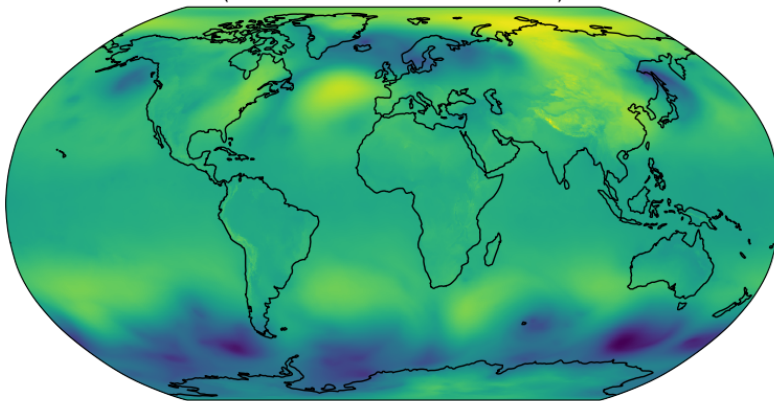


Figure G24 | Visualisation of mean sea level pressure.

## H. Author Contributions

In alphabetical order by surname for each category of work:

Conceptualisation: P.B., S.M., I.P., M.W. Project management: P.B., R.L., I.P., J.S., M.W. Data Curation: P.B., A.E.K., I.P., A.S-G. Model Development: F.A., A.E.K., R.L., D.M., I.P., A.S-G., M.W. Code: F.A., T.R.A., T.E., A.E.K., R.L., D.M., I.P., A.S-G., M.W. Experiments and Evaluation: F.A., T.R.A., A.E.K., R.L., D.M., I.P., A.S-G., M.W. Paper writing (original draft): F.A., T.R.A., P.B., R.L., I.P., A.S-G., M.W. Paper writing (reviewing and editing): F.A., T.R.A., P.B., A.E.K., D.M., S.M., I.P., A.S-G., M.W.